THE DEEPWATER VOLCANICLASTIC MISTAKEN POINT FORMATION IN THE NORTHEASTERN AVALON PENINSULA: FACIES, ARCHITECTURE, AND DETRITAL (U-PB) ZIRCON PROVENANCE

By

Grace Khatrine

A dissertation submitted to the School of Graduate Studies

In partial fulfilment of the requirements for the degree of

Master of Science

Department of Earth Sciences

MEMORIAL UNIVERSITY OF NEWFOUNDLAND

March 2024

St. John's, Newfoundland and Labrador, Canada

Abstract

The Mistaken Point Formation (MPF) is a ~400 m-thick late Neoproterozoic siliciclastic-volcaniclastic unit that crops out in the Avalon Zone of Newfoundland Appalanchians and is recognized as one of the world's leading Ediacaran fossil-bearing deep-water successions. The MPF sits at the top of a thick sequence of volcaniclastic submarine fan strata within the Conception Group. These layers were deposited during the transition from a fore-arc or back-arc basin to a potentially foreland basin. Thus, MPF strata can provide insight into whether the basin transformation may have influenced important aspects of the sedimentary environment during the deposition of the MPF. Detailed stratigraphic, petrographic, and facies analysis were integrated, supporting a submarine fan depositional system with two lobe complexes: MPF1 and MPF2. Stratal stacking patterns indicate a “back stepping” lobe abandonment. Examination of facies reveals the presence of ponded turbidites and stratification resembling HCS, which document the gradual confinement of the basin over time. Paleocurrent measurements demonstrate a slight variation in sediment routing directions from S-SE to S-SW. MPF1 detrital zircon ages define a unimodal peak at ca. 650 Ma consisting mostly of Ediacaran to Cryogenian, subordinate peak of Mesoproterozoic and Paleoproterozoic ages, whereas the overlying MPF2 depicts a polymodal distribution with peaks at ca. 600 and 580 Ma comprising mostly Ediacaran ages, less Cryogenian than MPF1, and Mesoproterozoic ages. This research emphasizes the development of the MPF submarine fan system as it undergoes basin transformations. This transformation plays a crucial role in enhancing our understanding of paleogeographic reconstructions of submarine fans. It also provides valuable insights into the evolution of the basin and tectonic processes of Ediacaran strata in the northeastern Avalon Peninsula.

General Summary

The succession accumulated in a submarine fan system with stratal stacking patterns suggests a “back stepping” lobe abandonment with overall upward reduction in sediment concentrations, flow energy, syn-sedimentary volcanism, and basin confinement through time. The reconstructed paleoflow directions predominantly shift from SE to S-SW is similar to what is seen in strata across the Avalon Peninsula, and supports a two-phase tectonic history hypothesized for the Late Neoproterozoic (Ediacaran) rocks of the Avalon Zone. The change in flow directions was diachronous across sections of the MPF, occurring much earlier in the northern sections near St. John’s and Spaniard’s Bay, suggesting the influence of a southward-propagating uplift. A ternary plot was constructed using QFL data from 10 point-counting highlights the changes in mineral composition. Detrital zircons within the MPF are dominated by ages corresponding to the main Avalonian Arc (ca. 620-630 Ma). Sediment sources changed upward within the MPF, characterized by increasing contributions of Mesoproterozoic zircons, a decrease in Tonian sources, and the loss of Paleoproterozoic grains. Maximum depositional age estimates and sediment provenance for the MPF1 and MPF2 facies yield 567.2 ± 10.1 Ma and 560.33 ± 3.72 Ma, respectively suggesting that these hinterland changes, uplift, lobe retrogradation, and basin confinement occurred at circa. 565 Ma. The provenance and stratigraphic evidence further suggest synchronous hinterland uplift, coinciding with tectonically-driven basin confinement.

Acknowledgement

I am immensely grateful to Dr. David Lowe, my supervisor, for his unwavering support and guidance. His dedication, time, and resources have been instrumental in helping me develop my geoscience skills and pursue my passion. I also acknowledge my committee member Dr. Duncan Mcllroy and all the reviewers for their valuable feedback that have greatly contributed to the quality of my work.

I thank Memorial University's CREAIT team and network during the data acquisition. Matt Crocker, Wanda Aylward, Dylan Goudie, Marcus Walle, Sherri Strong, Rebecca Lam, and Inês Nobre Silva.

Highest appreciation to all the researchers who have supported me both in and out of the field. I am grateful to all my team in the Tectonostratigraphy Research Group led by Dr. Lowe, Dr. Gregory Dunning, Dr. Bill Arnott, Dr. Alex Liu, Dr. Guy Narbonne, Pascal Olschewski, and Andrea Mills for their valuable contributions.

I want to express my deep gratitude to my mom, dad, CMFI church, and beloved ones. Their constant prayers, encouragement, and support have been a source of strength throughout my studies in a foreign country.

Finally, I thank My Lord and Savior, Jesus Christ.

Table of Contents

ABSTRACT .... **II**

GENERAL SUMMARY .... **III**

ACKNOWLEDGEMENT .... **IV**

TABLE OF CONTENTS .... **V**

LIST OF TABLES .... **VIII**

LIST OF FIGURES .... **IX**

LIST OF ILLUSTRATION .... **XV**

LIST OF APPENDICES .... **XVI**

CO-AUTHORSHIP STATEMENT .... **XVII**

CHAPTER I - THESIS INTRODUCTION **1**

1.1 BACKGROUND OF STUDY 1

1.2 INTRODUCTION 2

1.3 GEOLOGICAL SETTING 5

1.4 LOCATION 9

1.5 METHODOLOGY 10

CHAPTER II - FACIES AND SEDIMENTARY PROCESS **14**

FACIES 1: CONGLOMERATE 14

F1A. Matrix-supported Conglomerate 14

F1B. Thin clast-supported Conglomerate 15

FACIES 2: SANDSTONE 20

F2A. Massive Sandstone Beds with Graded Tops 20

F2B. Planar-Stratified, Normally Graded Sandstone 21

F2C. Thin Cross-Stratified Sandstone Sets 22

F2D. Climbing Ripple Cross-Stratified Sandstone *23*

F2E. Hummocky Cross-Stratification (HCS)-like Sandstone *24*

FACIES 3: MUDSTONE 25

F3A. Thin Massive Mudstone *25*

F3B. Thick Massive Mudstone *26*

F3C. Laminated Siltstone/Mudstone *27*

FACIES 4. HETEROLITHIC FACIES 28

FACIES 5. BOUMA SEQUENCE (TA-TE) 29

FACIES 6. IRREGULAR POST-DEPOSITIONAL STRATIFICATION 30

FACIES 7: TUFF (VOLCANIC LAYERS) 32

F7A. Thin Crystal Ash Tuff *32*

F7B. Vitric Lapilli Tuff *33*

F7C. Tuffite/ Tuffaceous Beds *34*

CHAPTER III - FACIES ASSOCIATION AND ARCHITECTURE 36

FA1: AMALGAMATED SANDSTONE 36

FA2: SANDSTONE INTERBEDDED WITH SSD AND MUDSTONE 38

FA3: MUDSTONE INTERBEDDED WITH SILTSTONE AND SANDSTONE 40

FA4: HCS-LIKE CROSS-STRATIFIED SANDSTONE INTERBEDDED WITH THICK MUDSTONE 45

CHAPTER IV STRATIGRAPHIC ORGANIZATION 48

CHAPTER V - SEDIMENT PROVENANCE 54

SANDSTONE PETROGRAPHY 54

INTERSAMPLE DETRITAL ZIRCON COMPARISON 57

DETRITAL ZIRCON GEOCHRONOLOGY 58

CHAPTER VI - DISCUSSION 61

PROVENANCE INTERPRETATION 61

DEPOSITIONAL SYSTEM 63

BASIN RECONSTRUCTION 65

CHAPTER VII - CONCLUSION **70**

REFERENCES **74**

APPENDIX **17**

Appendix A: Deepwater Flow, Deposits, and Mechanism *17*

Appendix B: Methodology and Laboratorium Equipment *18*

Appendix C: Hierarchy of Lobe Architectural Elements *19*

Appendix D: Larger Version of Measured Sections in Selected Locations *20*

Appendix E: MPF 1 and MPF 2 Paleo flow Measurement (Rose diagram stereonet) *21*

Appendix F: Workflow of U-Pb Geochronology Analysis for the study *22*

Appendix G: Zircon U-Pb Geochronology data tables *23*

Appendix H: SEM-CL images of zircon grains *30*

Appendix I: Mapping SEM-CL image zircon address *47*

List of Tables

Table 2.1 Facies Organization of seven facies and fifteen subfacies based on lithology by field- and microscopic observations, including sedimentary textures, structures, geometry and interpretation 16

Tabel 3 1 The overall distribution of lithofacies in each facies association, divided into three sections ranging from rare to abundant. FA1 and FA2 are dominated by F1 and F6. F2 and F7 relatives are found in all facies associations, but are more common in FA1 and FA2, whereas F2E, F3, F4, and F5 are abundance in FA3 and FA4. 39

Table 5.1 Cross-correlation Coefficient Matrix 57

List of Figures

CHAPTER I

Figure 1.1 (A) Avalonia, the largest accreted crustal block in the Appalachian - Caledonian orogen, records a Neoproterozoic tectonomagmatic history as a Neoproterozoic arc-related terrane along the active margin of Gondwana. The green squares A to D (upper left) are elucidated in distinct time intervals (bottom left), encompassing a complex basin evolution and magmatic evolution. This includes the occurrence of High-P metamorphism and deformation around 600Ma, followed by Low-P metamorphism, uplift, and deltaic progradation during 560Ma where MPF deposited and syn-deformational sedimentation around 550Ma. Red square identifies the study area, known as Avalon Peninsula. **(B)** Late Neoproterozoic to Early Cambrian stratigraphy of the Avalon Peninsula based on Williams and King (1997) and King et al (1988) highlights major faults and the location of U-Pb detrital zircon samples 3

Figure 1.2 (A) Eastern Avalonia particularly the Avalon Peninsula, southeast Newfoundland, showing the distribution of Mistaken Point Formation (MPF) in the north-eastern margin. **(B)** Map of Mistaken Point area, including access route and sections measured in this study **(C)** Regional stratigraphy with geochronological data and cross-section of St. John's area modified after . Regionally comprises Neoproterozoic magmatic arc and sedimentary cover sequences sub- to deep marine siliciclastic and volcaniclastic rocks dominated by volcanogenic turbidites Conception Group (this study) overlain by shallow marine to deltaic St. John's group and fluvial to alluvial fan Signal Hill Group (…). 5

CHAPTER II

Figure 2.1 Conglomerate Facies (F1) (A) Thin (7 cm) granule-sized clast-supported conglomerate associated with the other two units (from bottom) interlaminated red mudstone and greyish pebbly sandstone **(B)** Micrograph (Sample T-28) shows poorly sorted clast supported (F1B) granule-sized in poorly sorted matrix-supported conglomerate **(C)** 10 cm, granule- to pebble-sized moderately sorted matrix-supported conglomerate (F1A) associated with the underlying units vc-c sandstone (white lines shows the erosional base contact) and sharply overlying by tuff and interlaminated c-m sandstone and mudstone **(D)** Micrograph (Sample PC-13) shows granophyric texture as igneous rock fragment (Kf=k-feldspar, mcqz=microcrystalline quartz, qz=quartz, cl=chlorite, gr=granophyric texture, pl=plagioclase) 19

Figure 2.2 Sandstone Facies (F2) examined from outcrop-based **(A)** 35 cm normally graded sandstone from med sand to silt, capped sharply with 1 cm vf sand, mostly structureless with dewatering structures (blue arrow). Photo was taken at Trans-Canada Highway **(B)** Amalgamated massive and normal graded parallel-laminated sandstone, thinning upward, m to vf, with parallel lamination in the middle of 25 cm sandstone overlying the massive mudstone facies. Photo was taken at Brier Ave (Fig. 1.2) **(C)** Cross-stratified sandstone represented by climbing ripples and wavy correlated with mudstone and massive sandstone. Photo was taken at Middle Cove **(D)** Trough cross stratification as a feature of F2D. Photo was taken at TCH 3. 21

Figure 2.3 Mudstone Facies (F3) (A) Si-rich, massive mudstone facies (F3A). Photo was taken at Airport Heights (Fig 1.2) **(B)** Photomicrograph PPL, massive mudstone (F3A) shows the lack of internal structures. White bar equals to 1 m **(C)** laminated mudstone facies (F3C). Photo was taken at TCH 3 **(D)** Photomicrograph PPL, fissile-looking, clay-rich laminated mudstone shows faint wavy-lenticular lamination (F3C)26

Figure 2.4 Heterolithic Facies (F4) (white brackets) **(A)** Medium-bedded interlamination between red mudstone, dark grey siltstone, and greyish fine sandstone, with black organic-rich on top of the facies (blue arrow). F4 then overlain by yellowish normally graded tuffaceous sandstone **(B)** Thin-bedded interlamination between dark grey mudstone, greenish siltstone, and dark grey fine sandstone. F4 here associated with thin dark red massive mudstone (pink arrow) and planar laminated sandstone (yellow arrow) 29

Figure 2.5 Ideal Bouma Sequence (F5) (A) Medium bedded (30 cm) of Ta-Te located in Team Gushue Highway 3 **(B)** Thin bedded (<10cm) Bouma sequence in small scale (Ta-Te) located in Brier Ave. Location details in Fig 1.2. 30

Figure 2.6 Irregular Post Depositional Stratification Facies (F6) by Soft-sediment deformation **(A)** Thin laminar parallel lamination (*yellow arrow*) overlain by fine-grained convolute lamination sandstone **(B)** Convolute bedding medium-grained sandstone. Both photos are located in Middle Cove coast. 32

Figure 2 7 Tuff and Tuffaceous Facies (F7) (A) Crystal ash tuff F7A located in Middle Cove coast **(B)** Phenocryst stratified lapilli tuff facies **(C)** Tuffaceous beds. Photos B and C were taken at Hyundai outcrop **(D)** Micrograph (Sample C3-43) PPL - Slightly altered volcanic glass shard, Y—shaped and curved forms are well-preserved. Biotite phenocryst is visible **(E)** Micrograph (Sample C3-43) XPL - Crystal-vitric tuff, contain altered plagioclase 35

CHAPTER III

Figure 3.1 Architectures and interpretation with overall staking patterns of the measured Lobe and Lobe Complexes **(A)** It is at approximately 8 m stratigraphic height of lobe axis (FA1) to distal lobe (FA3) **(B)** Lobe fringe (FA2) with erosional contacts, thickening upward **(C)** Lobe axis (FA1) shows thinning and thickening upward **(D)** Off axis to Proximal Lobe Fringe (FA2) shows thinning upward **(E)** HCS-like sandstone (FA4) shows 3-4 vertical generations. The white rectangular scale represents one meter 43

Figure 3.2 (A) 180 hundred meters stratigraphic column comprises of two lobe complexes (*dark green square* represent MPF1 and *light green square* represent MPF 2 or younger member) **(B)** Cross section of A-A' and B-B' shows dimension, changing in lobe staking pattern (thickening-thinning), and some observed lobe element from field observation. *Black arrow* indicates younging direction. *Red star* in the right below picture indicates the contact boundary between MPF and older Drook fm. All attached pictures are located in Team Gushue Highway (contact approx. 47.547763, -52.765821). 45

Figure 3 3 Conformity relationship between MPF 1and MPF 2 which distinguished by their degree of confinement, exposed in Middle Cove section close to Torbay area (see Fig. 1.2 for area locations). **B)** Interpreted Upper MPF lobe elements or confined setting exposed in Section Middle Cove hundred meters east from A. Red arrow, respectively indicate paleoflow directions. Red solid lines represent fault near section; black dashed line represents sharp contact; red and blue dashed line represents upper and lower members. Black triangles represent upward coarsening and thickening trends. 46

CHAPTER IV

Figure 4.1 NE-SW, ±400m thick stratigraphic correlation of selected measured section in the northeastern Avalon Peninsula. The diagram shows a change of predominance facies association (lobe) from the older (MPF1) FA1-FA3 interlobes to the younger (MPF2) FA2-FA4 interlobes. The transition of MPF 1 and MPF 2 represent by blue line. Paleocurrent from current-ripple reading represent in black arrows is shown shifting from SE to SSW, respectively. Bed markers or marker horizons are lithography, including crystal ash tuff and conglomerate. They are shown in the red dashed line. Nametag above each section refers to site names with numbers in dividing sub-section [HY, Hyundai; GH, Team Gushue Highway; CH, Trans-Canada Highway; MC, Middle Cove; AH, Airport Heights]. 48

Figure 4.2 The graph demonstrates the compensational stacking pattern of lobe complexes, explaining the differences between lateral migration, retrograding, and prograding compensational staking pattern (modified from Zhang, 2016). 51

CHAPTER V

Figure 5.1 Selected thin section photomicrographs in PPL and XPL shows mineral composition. The methodology employed for this analysis is point-counting (Gazzi-Dickinson) (V-volcanic clast; S-sedimentary clast; PQ-polycrystalline quartz; Gl-glouconite; Q-monocrystalline quartz; Cb-carbonate; Plg-plagioclase; Fd-feldspar; Cal-calcite; Ep-Epidote m-matrix) 55

Figure 5.2 The QFL and QpLvmLsm ternary plots from selected ten samples. Five samples of MPF 1 plot on the dissected arc field in the QFL (Dickinson, 1988) diagram and on the magmatic arc field in the Qp-Lvm-Lsm diagram (Ingersoll and Suczek, 1979). The remaining five samples of MPF 2 plot between the basement uplift and dissected arc fields in the QmFLt diagram, and between the magmatic arc and rifted continental margin fields of the Qp-Lvm-Lsm diagram. 55

Figure 5.3 The maximum depositional ages determined for the MPF1 (left) and MPF2 (right) facies are 567.2 ± 10.1 Ma and 560.33 ± 3.72 Ma, respectively. MLA was selected as the preferred method for this study to obtain the most accurate estimate and approach. The findings obtained through the MLA technique are most effectively presented using radial plots as suggested by Vermeesch (2021). 58

Figure 5.4 The detrital zircon geochronology analysis conducted on the MPF1 at Spaniard's Bay (MC-SB) reveals polymodal peaks at approximately 606 Ma, predominantly composed of Ediacaran zircons (66%) and Cryogenian zircons (6%). Additionally, there is a Tonian peak at around 752 Ma (7%), a Mesoproterozoic peak at approximately 1550 Ma (7%), and a Paleoproterozoic peak at about 2050 Ma (14%). On the other hand, the combined sample from the overlying MPF2 in Spaniard's Bay and Mistaken Point displays a polymodal distribution with peaks at approximately 607 and 560 Ma, with 80% of the zircons falling within the Ediacaran and Cryogenian age range spanning from 542 to 720 Ma. There are also subordinate peaks, including 3.5% Tonian ages with a peak at around 766 Ma, and 16.5% Mesoproterozoic and Paleoproterozoic ages with peak ages ranging from approximately 1230 to 1400 to 1700 Ma. 59

List of Illustration

CHAPTER VI

Illustration 6.1 Conceptual Model of the MPF Depositional System. MPF represents an active period of volcanic activity concurrent with submarine fan sedimentation, with an overall reduction of flow energy and degree of volcanic supply through time. Stratigraphic evidence suggests MPF strata were deposited by concentrated density flows to low-energy turbidity currents, which are represented by facies conglomerate, sandstone, and mudstone. Two different mechanisms of volcanic ash deposit: (1) hemipelagic settling by wind-derived and suspension (2) resedimented and transported downslope with turbidity current, resulted in three sub facies of tuff. Along slope process (bottom current deposit) may be the influence of heterolithic facies deposition. 63

Illustration 6.2 The comparison of basin transition based on paleocurrent measurements in four distinct study areas within the Avalon and Bonavista Peninsula. The pink dashed lines indicate a gradual shift of basin transformation. The transition firstly occurred in the St John's area approximately halfway through the MPF's succession., then followed in the Spaniards Bay (Conception Bay, 42 kms western St John's) within the upper MPF formation. It then occurred in the Catalina Dome, Bonavista Peninsula (nearly 100 kms northwest St. John's) within the Trapasssey Formation. Finally, it observed between the Trepassey and Fermeuse formations in the Ecological Reserve MPF in the southeastern Avalon Peninsula 65

List of Appendices

Appendix A: Deepwater Flow, Deposits, and Mechanism

Appendix B: Methodology and Laboratorium Equipment

Appendix C: Hierarchy of Lobe Architectural Elements

Appendix D: Larger Version of Measured Sections in Selected Locations

Appendix E: MPF 1 and MPF 2 Paleo flow Measurement (Rose diagram stereonet)

Appendix F: Workflow of U-Pb Geochronology Analysis for the study

Appendix G: Zircon U-Pb Geochronology data tables

Appendix H: SEM-CL images of zircon grains

Appendix I: Mapping SEM-CL image zircon address

Co-authorship Statement

This dissertation follows a conventional format and comprises of seven chapters. The first chapter introduces the subject matter, the issues at hand, the objectives, outlines the geological context of the units under investigation, the location of the measured sections, and the methodologies employed in the research. Chapter two delves into the description and interpretation of sedimentary facies and environments. Chapter three focuses on facies associations, encompassing the distribution of facies, their interrelationships, and their boundaries. Chapter four elaborates on the stratigraphic arrangements. Chapter five discusses sediment provenance, including sandstone petrography and detrital geochronology. Chapter six engages in a discussion and examines the implications of the findings in light of existing geological knowledge and models for the Avalon Peninsula. Lastly, chapter seven offers a comprehensive summary of the MSc research.

The research conceptualization and development were led by Dr. David Lowe. The author undertook all primary research tasks, such as measuring stratigraphic sections, collecting samples, preparing samples, and conducting petrographic analysis. The author conducted heavy mineral separation under the guidance of Matthew Crocker. SEM-CL analyses and backscatter imaging were performed by the author under the supervision of Dr. Gregory Dunning, Dylan Goudie, and Wanda Aylward. The author performed U-Pb LA-ICPMS analyses and data reduction with the assistance of Dr. Markus Wälle.

Dr. David Lowe served as the primary editor of the manuscript.

CHAPTER I - THESIS INTRODUCTION

1.1 Background of Study

The Mistaken Point Formation (MPF) of the Avalon Peninsula of Newfoundland, Canada, is recognized as one of the world's leading Ediacaran fossil-bearing deep-water successions (ca. 630-542 Ma) (Ichaso et al., 2007). During the past decades, the study of the Mistaken Point Formation (MPF) in the southern Avalon Peninsula, particularly palaeontology, has been well examined. However, details of the sedimentology of the Mistaken Point Formation exposed in the northern Avalon Peninsula near St. John's, including regional stratal evolution, correlations, and local sedimentary process, are not well understood. Notably, many new roadcut outcrops have been created since the early 2000s, the work on the local stratal succession in St. John's was done by King (1990). Indeed, the understanding from both the southern and northern successions of the Mistaken Point Formation on the Avalon Peninsula is critical to developing the sedimentary system by investigating the relatively narrow section of stratigraphy to understand the regional tectonic changes at the basin scale.

This research presents the details of the regional differences in the stratigraphic succession, sedimentary facies, and depositional conditions of the MPF from south to north across the Avalon Peninsula. In the context of tectonostratigraphy, this formation sits at or near the change from arc-adjacent basin sedimentation to the proposed foreland basin sedimentation of the overlying St. John – Signal Hill Groups (Serna-Ortiz and Lowe, 2024). Therefore, the distributions of facies associations, paleoflow, and provenance from the base to the top of the succession will explain how the basin configuration changed through MPF deposition, or if in fact it did.

1.2 Introduction

The geological history of Newfoundland (Appalachians) extensively documents the development of Gondwana, Laurentia, and related terranes as they experienced tectonic accretion during the orogenesis linked to the closure of the Iapetus and Rheic oceans in the early Paleozoic era (O'Brien et al., 1983; Nance and Murphy, 1996). The peri-Gondwanan terranes Ganderia and Avalonia are represented by the Gander and Avalon zones in central and eastern Newfoundland Appalachians, respectively. The Avalon Zone of Eastern Newfoundland (Fig 1.1) formed as a volcanic arc complex outboard of Gondwana during the Neoproterozoic. The Avalon Zone consists of three geologic regions (western, central, and eastern; Myrow, 1995; Nance et al., 2002). The Eastern region of the Avalon zone, cropping out mainly on the Avalon Peninsula, is considered the most inboard zone relative to the Gondwanan margin (O'Brien, 1988; Fig 1.1). The eastern Avalon zone consists of bimodal plutonic-volcanic rocks of the Harbour Main Group (631 – 606 Ma) overlain by volcaniclastic submarine fan-slope strata of the Conception Group (ca.584 Ma to 565 Ma: Bowring et al., 2003; Ichaso et al., 2007; Matthews et al., 2021), transition into shallow marine St John's to alluvial deposits Signal Hill groups (Myrow, 1995; King, 1990). The Harbour Main Group is exposed along the eastern shore of Conception Bay. The Conception Group (Fig 1.2) crops out east of the Topsail Fault and underlies much of the eastern Avalon Peninsula (Fig. 1B). King (1990) considers the base of the Conception Group as a conformable contact above the Harbour Main Group; whereas Sparkes et al. (2021) show that the Harbour Main- conception groups contact is at least locally unconformable. According to King (1990), the Conception Group is conformably overlain by a shallowing-upward succession of dark-grey, marine shale, and sandstone of the St. John's Group, which occurs in the eastern part of the map area. The Signal Hill Group, a thick deltaic and alluvial-plain sequence, is believed to be the most recent Precambrian to potentially Early Paleozoic deposit that conformably sits above the St. John's Group (King, 1990; Beranek et al., 2023).

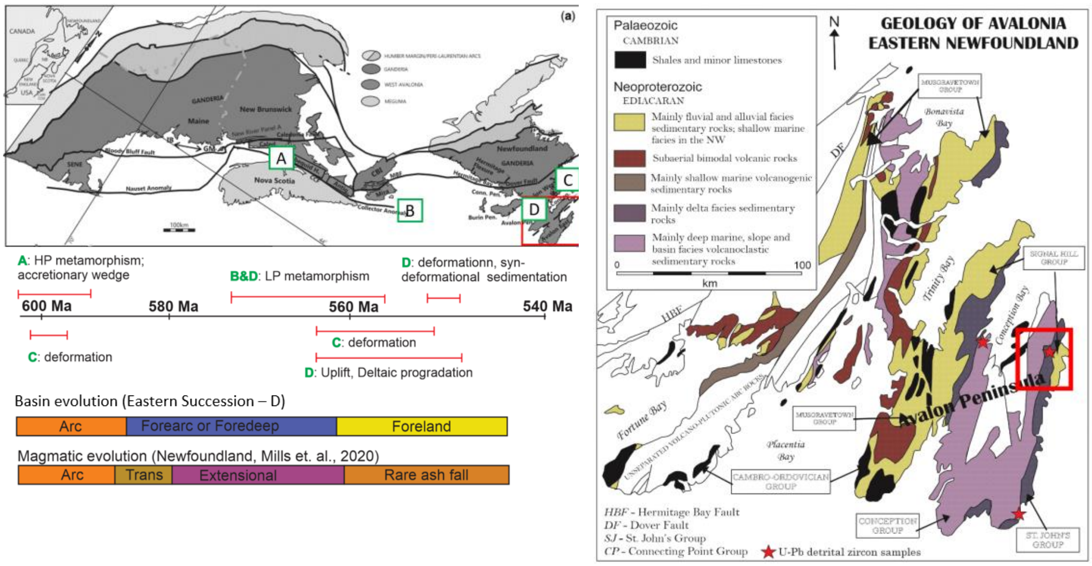

Figure 1.1 (A) Avalonia, the largest accreted crustal block in the Appalachian - Caledonian orogen, records a Neoproterozoic tectonomagmatic history as a Neoproterozoic arc-related terrane along the active margin of Gondwana (modified from van Staal et al., 2021). The green squares A to D (upper left) are elucidated in distinct time intervals (bottom left), encompassing a complex basin evolution and magmatic evolution. This includes the occurrence of High-P metamorphism and deformation around 600Ma, followed by Low-P metamorphism, uplift, and deltaic progradation during 560Ma where MPF deposited and syn-deformational sedimentation around 550Ma. Red square identifies the study area, known as Avalon Peninsula. **(B)** Late Neoproterozoic to early Cambrian stratigraphy of the Avalon Peninsula based on Williams and King (1997) and King et al. (1988) highlights major faults and the location of U-Pb detrital zircon samples. Red square identifies the study area, St John's city.

The thickness of the Mistaken Point Formation spans approximately 400 meters across the Avalon Peninsula. This formation is identified as the uppermost part within a substantial sequence of volcaniclastic submarine fan strata of the Conception Group (see Appendix A). MPF is generally composed of interbedded thin- to medium-bedded greenish-grey and reddish-purple tuffaceous siltstone, shale, and sandstone. The upper Mistaken Point Formation contains a tuff bed that has yielded a U-Pb zircon date of 565 ± 3 Ma (Benus, 1988). This particular date was selected by Williams and King (1979) to establish the upper boundary of the Conception Group. The study conducted by Matthews et al. (2021) provides a detailed analysis of six radioisotopic ages obtained from zircons found in volcanic tuffites within the Conception and St. John's Groups at Mistaken Point Ecological Reserve (south Avalon Peninsula). In the upper Drook Formation, the oldest (dated at 574.17 ± 0.66 Ma) architecturally complex macrofossils, located. On the other hand, the youngest rangeomorph fossils discovered in the Fermeuse Formation at Mistaken Point Ecological Reserve have a maximum age of 564.13 ± 0.65 Ma (Matthews et al., 2021) and 562.5 ± 1.1 Ma (Canfield et al., 2020). Recent geochronological data obtained from the southern Avalon Peninsula provide a depositional age range from 567.48–563.81 Ma of the Mistaken Point Formation, based on zircon U-Pb geochronology using high-precision CA-TIMS technique (Matthews et al., 2021). Ichaso et al. (2007), in his studies at West Conception Bay, north-western Avalon Peninsula, investigated the basin evolution of the Mistaken Point Formation. As the uppermost part of Conception group and transition to the St. John's group, this formation records the conditions of arc-adjacent volcaniclastic sedimentation at or below the transformation of the basin to prodelta pull-apart basin sedimentation according to Ichaso et al. (2007).

The purpose of this investigation is to detail the sedimentary evolution of the Mistaken Point Formation on the northern Avalon Peninsula. Specifically, the goal is to better understand the regional stratigraphic and sedimentologic changes from the south to the north of the Avalon Peninsula by integrating the local stratigraphic framework with reconstructions of submarine fan sedimentary process and architecture and sediment provenance. The research will also provide the context of the terminal arc-adjacent phases of sedimentation in the Avalon Zone and constrain the maximum depositional age. The study will be undertaken by developing a holistic 'source-to-sink' approach of sedimentary facies analysis, stratal architectural analysis, and sediment provenance.

1.3 Geological Setting

Late Neoproterozoic volcaniclastic and sedimentary successions of the Conception Group exposed along the eastern and southern margin of the Avalon Peninsula have been widely studied over the last 40 years (Williams and King, 1979; Misra, 1981; Anderson, 1987; Gardiner and Hiscott, 1988; Benus, 1988; Myrow, 1995; Narbonne et al. 2001; O' Brien et al., 1983; Murphy et al., 1999; Nance et al., 2002; Wood et al., 2003; Ichaso et al., 2007). However, Conception Group strata along the northeastern margin of the Avalon Peninsula, including the Mistaken Point Formation, have not been as well studied. In fact, the most recent investigation in this area was by King (1990), which covered few details of the sedimentary facies or provenance of Mistaken Point Formation in this area. Moreover, since 1990, many new roadcut exposures of the Mistaken Point formation have been created in and around St. John's, providing a unique opportunity to study the details of its sedimentology using facies and architectural analysis.

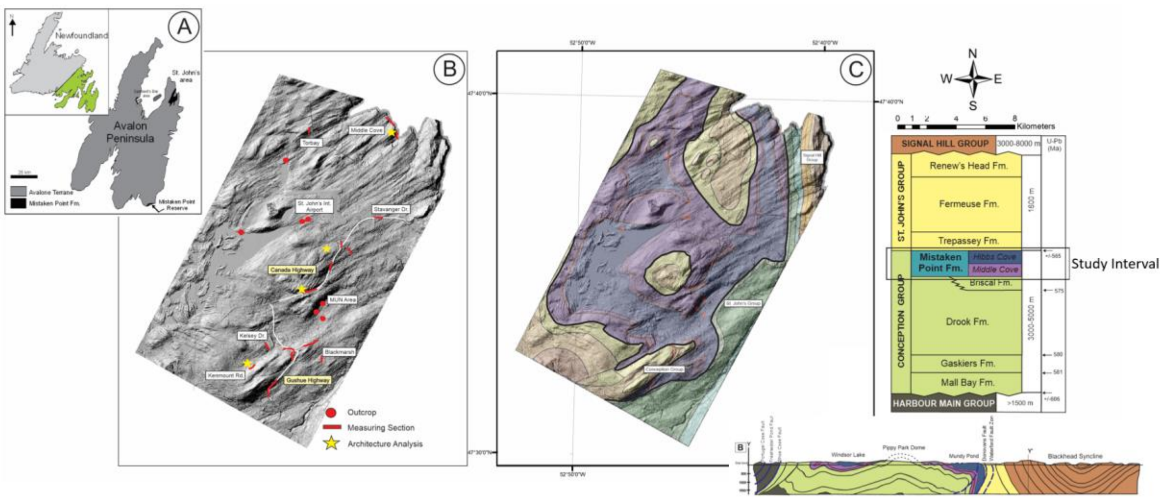

Figure 1.2 (A) Eastern Avalonia particularly the Avalon Peninsula, southeast Newfoundland, showing the distribution of Mistaken Point Formation (MPF) in the north-eastern margin. **(B)** Map of Mistaken Point area, including access route and sections measured in this study **(C)** Regional stratigraphy with geochronological data and cross-section of St. John's area modified after King (1990) and Williams and King (1979). Regionally comprises Neoproterozoic magmatic arc and sedimentary cover sequences sub- to deep marine siliciclastic and volcaniclastic rocks dominated by volcanogenic turbidites Conception Group (this study) overlain by shallow marine to deltaic St. John's Group and fluvial to alluvial fan Signal Hill Group (Krogh et al., 1988; Bowring et al., 2003; G. Dunning in Benus, 1988)

The 3- to 5-km-thick marine sequence of the Conception Group suggests sedimentation contemporaneous with volcanism (Hughes and Bruckner, 1971), coeval with Harbour Main Group volcanism. The Conception Group of southeastern Avalon Peninsula is divided into five formations: Mall Bay, Gaskiers, Drook, Briscal, and Mistaken Point (Williams and King, 1979). Of these, only the Drook and Mistaken Point Formations are exposed on the northern Avalon Peninsula. In the southern Avalon Peninsula, the Mistaken Point Formation conformably overlies the Briscal Formation (Williams and King, 1979; King, 1990; Narbonne et al., 2001), with the base defined where thick-bedded turbidites of the underlying Briscal Formation pass upward into the thin-and medium-bedded turbidites of the Mistaken Point Formation (Wood et al., 2003). In the northern Avalon Peninsula, the Mannings Hill Member of Drook Formation passes stratigraphically upwards gradationally by interfingering with the Mistaken Point Formation. The boundary is arbitrarily placed at the lowest variegated chert-tuff bed (King, 1990).

The Mistaken Point Formation (Fig 1.2) consists of a 400 m thick succession medium-bedded turbidites (Ta-c,e Bouma Sequence) and siltstone with and millimeter- to centimeter-thick volcanic ash layers that locally mold the Ediacaran fossils (King, 1990). The Mistaken Point Formation consists of the Middle Cove and Hibbs Cove members. The Middle Cove Member (lower member) is characterized by medium bedded, graded, variegated tuffs, and cherts (King, 1990). These strata are prominently visible along a 1-km coastal stretch to the north of Middle Cove (King, 1990). The thickness of this unit is approximately 100 m and remains consistent across the Avalon Peninsula from south to north. Although there are minor east-west striking strike-slip faults, correlation is marked by marker beds of tuff (King, 1990). Middle Cove Member is in sharp, conformable contact with the overlying argillaceous rocks of the Hibbs Cove Member. The Hibbs Cove Member, first named by Hutchinson (1953), is the uppermost unit of the Conception Group, defined by the medium to thick beds of reddish-purple and green argillaceous siltstones, very fine-grained parallel laminated sandstones with parallel laminations. The Hibbs Cove Member can be traced throughout much of the central and eastern Avalon Peninsula, where its thickness gradually increases from about 10-20 m in the south to about 300 m in the northern Avalon Peninsula (King, 1990). The boundary between the Middle Cove and Hibbs Cove members is a sharp, conformable contact representing a change from highly silicified strata below to argillaceous rocks above, reflecting a rapid decline in volcanism and volcaniclastic sedimentation (King, 1990). Only minor tuff laminae are present in the Hibbs Cove Member compared to abundant tuff in the Middle Cove Member. Interturbidite hemipelagic layers (Tf division) are documented in the Mistaken Point Formation exposed in the southern Avalon Peninsula (Hesse, 1975) but have not been recognized in exposures in the northern Avalon Peninsula.

The Mistaken Point Formation preserves fossils of some of the oldest known assemblages of the Ediacaran fauna. Within this formation, numerous discoid and frondose Ediacaran fossils are found, spanning over 60 fossil-rich surfaces near Mistaken Point. Ecological Reserve (Matthews et al., 2021) and are comparable in terms of species diversity and abundance to a modern deep marine ecosystem (Clapham, 2003). Paleocurrent directions measured from the Mistaken Pont Formation in the southern Avalon Peninsula from current ripples of the Tc Bouma turbidites

(1962) turbidites show easterly and south-easterly directions, whereas biological indicators (oriented fronds) in laminated siltstone show southwest (SW) paleoflow, approximately orthogonal to the physical indicators (Narbonne et al., 2001, Wood et al., 2003). According to Ichaso et al. (2007), this orthogonal disposition implies that deposition of the laminated interturbidite siltstone occurred mainly under the influence of weak contour currents. The southeast paleoflow of turbidites in the north-western Avalon Peninsula is orthogonal to the proposed axis of the basin, suggesting that sedimentation occurred on a basin-margin slope (Ichaso et al., 2007). Paleoflow measurements from Mistaken Point Formation strata in the northern Avalon Peninsula are not documented.

Sedimentation of the Mistaken Point Formation is variably interpreted to have occurred in a forearc basin (Narbonne et al., 2001; Wood et al., 2003), intra-arc basin (Dec et al. 1992), or back-arc basin (Myrow 1995; Murphy et al. 1999). Ichaso et al. (2007) outlined the persistence of contour currents and deep-water tidal currents throughout the Mistaken Point and Trepassey formations, suggesting deposition in an structurally unconfined, relatively open basin connected to the open ocean, typical of a forearc basin setting, rather than back-arc or intra-arc. Narbonne et al. (2001) noted that the overlying Trepassey and Fermeuse formations of St. John's Group record slope sedimentation during the transition between a forearc and pull-apart basin setting. This transition is marked by the change in the paleocurrent directions from the southeast (transversal to the basin axis) to more southwest (axial oriented) and the dominance of thin-bedded turbidites. However, Ichaso et al. (2007) found the paleocurrent changes occur at a lower stratigraphic level close to the top of the Mistaken Point Formation. This suggests that the transition was diachronous and occurred earlier in northern areas and moved progressively to more southern areas within the basin.

The sandstone of the Mistaken Point Formation consists mainly of feldspathic wacke containing detrital calcic plagioclase, quartz, volcanic rock fragments, biotite, and muscovite, consistent with derivation from magmatic-arc sources (Ichaso et al., 2007)

Detrital zircons of the Conception Group (Briscal and Mall Bay Formations) are dominated by an Ediacaran-aged zircon population (562 to 641 Ma) that constitutes ca. 90% of the zircons (Pollock et al., 2009). The sedimentary rocks of the Conception Group contain a majority of zircons with ages between ca. 570–620, corresponding to main magmatic activity in the adjacent Neoproterozoic Avalonian arc (Pollock et al., 2009) according to the petrography and provenance data (Dec, 1992). Therefore, the Conception Group is interpreted to have been sourced mainly from coeval arc igneous rocks of the Harbour Main group. The change from siliceous volcaniclastic rocks of the Conception Group to overlying molasse-like red beds of the Signal Hill Group represents a transition from deep-water turbidite deposition to shallow marine and alluvial plain conditions. Moreover, the overall coarsening- and thickening-upwards sequences of the Signal Hill Group (King, 1990) indicate that deposition occurred in a tectonically active fault-bounded basin coeval with uplift of the underlying arc sequences during the latest Neoproterozoic Avalonian orogeny (Hughes, 1970; Beranek et al., 2023; Serna-Ortiz and Lowe, 2024).

1.4 Location

The study area is located in the St. John's area, in the northeastern Avalon Peninsula, Newfoundland and Labrador, Canada (Figs. 1.2, 1.3). Here, the Mistaken Point Formation strata are well-exposed. Geographically, the area is bound to the north by Middle Cove and Torbay Road, east of Portugal Cove, to the south by the end of Gushue Highway, and west by Windsor Lake, within latitudes 47°65' to 47°53' and longitudes

-52°69' to -52°78'. Each section consists of a well-exposed and easily accessible continuous outcrop of the Mistaken Point Formation. Most sites are roadcut outcrops along highways that can be reached by car or bus. The other exposures are along the coasts and in quarries.

1.5 Methodology

Fieldwork and Detailed Stratigraphy: Detailed mapping and fieldwork of the Mistaken Point Formation was conducted at a centimetric scale across the Avalon Peninsula, include measuring stratigraphic sections, structural and paleocurrent measurements. Eighteen stratigraphic sections of 20 to up to 300 m were measured to provide sedimentological-environmental data, contact relationships, mineral/ clast composition, and the stratigraphic position of volcanic ashes. GPS was used to record station locations using UTM Zone 22 coordinate system. The interpretation of facies and facies associations was conducted to understand the depositional processes and sedimentary environments. This interpretation was based on careful analysis of grain size, stratal geometry, and sedimentary structures (James and Dalrymple, 2010). Seven facies are group into four facies association that reflect combinations of processes and therefore environment of deposition, discussed below. Thin section petrography was used to identify texture, composition, and effect of early diagenesis to better constrain depositional process and environment.

Architectural Analysis: Drone-based aerial photography was undertaken for outcrop photogrammetry and architectural analysis to further reconstruct details of the sedimentary environment by placing the constituent facies into a hierarchical framework of bounding surfaces (Miall, 1985). The cross-sectional geometry of architectural elements within the Mistaken Point Formation was identified by utilizing photogrammetric models and photomosaics of laterally continuous outcrops. These outcrops, which spanned several tens of meters in width and were exposed along cliff faces, offered important insights into the structural attributes (architectures) of the formation. The data acquisition process involved the utilization of a DJI Mavic 2 Pro (Appendix B) for capturing images, while Pix4D software version 4.7.5 was employed to construct the photogrammetric models. Subsequently, the photogrammetric models were analyzed and interpreted using Leapfrog Geo software version 2021.2.5 and Virtual Reality Geological Studio software version 3.1. This helped identify recurring architectural elements, e.g., channels, lobes, sheets, sandy bedforms, accretional, scour, sediment gravity-flows, etc. (e.g., Lowe and Arnott, 2016).

Paleoflow Analysis: Orientation dip and azimuth of paleoflow were used to interpret the direction of sediment-transporting currents from ancient flows. Paleoflow data, in combination with facies and provenance data, were employed to construct comprehensive paleogeographic reconstructions. Paleoflow were measured from ripple cross-stratified sets and restored to paleohorizontal using the method of Lisle and Leyshon (2004) via Stereonet software version 11 of Cardozo and Allmendinger (2013). Rose diagrams were used to summarise directional data graphically.

Detrital Zircon U-Pb Geochronology: Provenance analyses were undertaken to help determine the directions of sediment transport and making geodynamic reconstructions of the history of orogens or sedimentary basins. Six samples weighing 1 – 2 kg were taken selectively to maximize the vertical and lateral coverage of successions. The samples were disaggregated and processed to isolate ~100-200 detrital zircon grains from each sample. Chemical abrasion, which included thermal annealing followed by partial dissolution in HF acid at a relatively low temperature, was utilized to reduce or eliminate the impact of Pb-loss. Mounting and polishing were used to reveal zircon cores, and SEM imaging used to characterize the morphology and zonation of detrital zircons and select appropriate sites for in-situ analysis (Appendix F, H). Ratios of Pb, U, and Th were measured from mounted detrital zircons using laser ablation inductively coupled mass spectrometry at Memorial University. For each specimen, between 80 and 250 zircons were subjected to ablation using a GeoLas 193nm excimer laser ablation system connected to a ThermoFinningan Element XR magnetic sector-inductively coupled plasma-mass spectrometer (ICP-MS) (Appendix G, H). The measurements were conducted with a 20 μm spot size, utilizing a laser fluence of 4 J/cm2, a pulse rate of 5 Hz, and 200 pulses, resulting in a total analysis duration of around 120 seconds. Data reduction and U-Pb age calculations were carried out employing the VizualAge data reduction method specifically designed for Iolite (Paton et al., 2011; Petrus & Kamber 2012). No common Pb correction was applied. Instrumental mass bias was corrected using standard-sample bracketing with the 91500-zircon standard (Wiedenbeck et al., 1995) and internal monitors. Concordance values were determined by comparing the $^{206}Pb/^{238}U$ and $^{207}Pb/^{206}Pb$ ages. Samples showing significant discordance (>10% discordant, >5% reverse discordant) were not included in the analysis and interpretation. The ages provided for grains younger than and older than 1000 Ma are derived from $^{206}Pb/^{238}U$ and $^{207}Pb/^{206}Pb$ ages, respectively (Appendix G). The U-Pb ages are reported at a 2σ uncertainty and showcased through Kernel density estimate (KDE) plots created using Vermeesch's IsoplotR software (2018). The determination of maximum depositional ages (MDA) can be achieved through various methods, including Younger Grain Cluster (YGC2σ), Youngest Single Grain (YSG), Youngest Statistical Population (YSP), and Maximum Likelihood Age (MLA). In this particular study, Maximum Likelihood Age (MLA) was utilized, primarily due to the high analyzed zircon numbers (n > 300) per sample which also included a significant proportion of young grains. Given this numbers and broader range of population ages, alternative methods were considered inappropriate for implementation in this study. The MLA algorithm is designed to converge towards the accurate solution as sample size increases, utilizing all available sample data (Vermeesch, 2021). Inter-sample comparison for correlations were statistically assessed using the multi-dimensional scaling method of Vermeesch (2013). A quantitative statistical analysis was carried out by comparing samples using the cross-correlation coefficient of probability density plots (PDPs). The comparisons were executed utilizing the “DZstats” software developed by Saylor and Sundell (2016). Close to 1 cross-correlation coefficient values indicate similar detrital zircon age distributions, while close to 0 values indicate different zircon age distributions (Saylor and Sundell, 2016).

Petrography: Petrography, using a polarized light microscope with a digital camera, facilitates in the interpretation of sedimentology and provenance. A detailed description of the mineral compositions and textural relationships of the detrital and diagenetic phases within the rock has been provided to support field observation. These analyses were carried out to 40 representative samples by point counting (200-300) following the Gazzi-Dickinson method. Point counting methods are employed primarily to determine statistical parameters and modal composition of rock samples (Ingersoll et al., 1984) using Dickinson et al. (1983) procedures. For provenance purposes, the sandstone samples were described by using the tectonic discrimination diagram of Dickinson (1988). Detrital framework components were graphed on QFL diagrams, enabling them to be plotted at one of the three poles in the ternary plot, as suggested by Pettijohn (1975) and Folk (1980). SEM-CL (Appendix H,I), a method for characterizing the composition, optical, and electronic properties of materials by correlating them down to the nanoscale was undertaken to understand the types of clay minerals for six representative samples.

CHAPTER II - FACIES AND SEDIMENTARY PROCESS

Seven sedimentary facies were recognized in the northeastern Mistaken Point Formations: Conglomerate (facies 1), Sandstone (facies 2), Mudstone (facies 3), Heterolithics (facies 4), Bouma sequence (facies 5), Irregular Post-depositional Stratification (facies 6), and Volcanic layers/ Tuff (facies 7) (Table. 1). In order to gain a better understanding of the conditions in which these sediments were deposited, these facies were further subdivided into subfacies, allowing for a more detailed analysis.

Facies 1: Conglomerate

Facies 1 comprises about 3% of measured sections and can only be found in the upper member of MPF. Beds of F1 are 1 to 20 cm thick, and laterally continuous over 10 km. Bed geometries are tabular with sharp and erosive basal contacts, and sharp top contacts. F1 is divided into 2 subfacies: clast-supported and matrix-supported conglomerate (Fig. 2.1; Table 2.1).

F1A. Matrix-supported Conglomerate

F1A consists of massive, 5 to 20 cm thick beds of moderately sorted, subrounded to subangular granule conglomerate. The clasts consist of sedimentary lithics (particularly mudstone), feldspar, quartz, and minor volcanic clasts embedded in poorly sorted medium sand to silt matrix. Most of the beds are inversely coarse-tail graded with an upward decrease in the proportion of matrix from 60% to 30%. The clast fabric in F1A is poorly developed where less than a half of clasts are aligned with their a-axes to the bedding orientation. Small-scale (2-5 cm) scours and load casts are also present at the base of beds (Fig. 2.1). Most of the beds have sharp and erosive basal contacts. F1A is associated with F1B and F3.

Interpretation: Gravelly non-cohesive hyper-concentrated density flows

Due to the broad range in grain size, moderate-sorting, lack of fabric, medium to thick bedding, and the absence of sedimentary structures, F1B is interpreted to record sedimentation from gravelly, non-cohesive high-concentration, possibly hyper-concentrated turbidity flows (Mulder and Alexander, 2001; R1–R3 of Lowe, 1982; Facies A2.5-6 of Pickering and Hiscott, 2015). Local inverse-grading may reflect the development of traction carpets under highly concentrated bedload layers (Hiscott, 1994; Sohn, 1997) which are believed to have had sufficiently high shear rates and low apparent viscosity to permit the upward migration of larger clasts by dispersive pressure (Hiscott, 1994).

F1B. Thin clast-supported Conglomerate

F1B is defined by 7-12 cm thick beds of clast-supported, moderately to well-sorted, granule conglomerate with 15% sand matrix. The grain size of matrix decreases upward in each bed from medium sand to silty fine sand. Clasts consist of subrounded to angular quartz, feldspar, volcanic and sedimentary lithic clasts with minor igneous and metamorphic clasts. The clast fabric in F1B is well developed (most if not all with their a-axes parallel to bedding). F1B beds have sharp basal contacts with 2-5 cm of localized scour into underlying strata and have sharp top contacts (Fig. 2.1C).

Table 2.1 Facies Organization of seven facies and fifteen subfacies based on lithology by field- and microscopic observations, including sedimentary textures, structures, geometry and interpretation

LITHOFACIES		DISTRIBUTION	DESCRIPTION				INTERPRETATION	
Facies	Sub-facies		TEXTURE	Sedimentary Structures and/or secondary features	Bed thickness, geometry, amalgamation degree and contacts	LOG	SEDIMENTARY PROCESS	FA
F1. CONGLOMERATE (3%)	**F1A. Matrix-supported conglomerate**	2%	Moderately sorted, subrounded to subangular, granule to pebble-sized clasts of sed. lithics and minor volc, mudstone embedded in 30-60% a poorly sorted matrix	Mostly ungraded, inversely ooarse-tail graded, and local small-scale internal scours and load casts. No imbrication.	5-20 cm, plannar, sharp to erosive base and sharp top	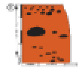	Fully turbulent, gravelly non-cohesive, hyper-concentrated density flow. Locally inverse grading may because of the development of traction carpet	FA2
	F1B. Clast-supported breccia/ conglomerate	1%	Moderately to well-sorted, subrounded to angular, granule to pebble-sized of volcanic and sed. lithics clasts, embedded in 15% a m sand to silt matrix, organized fabric	Ungraded, a-axis aligned to the bedding orientation	7-12 cm, plannar, localized scour, sharp bed bases and sharp top	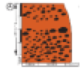	Gravelly non-cohesive concentrated density flows. Silt-sized matrix at the top as a result from suspension due to the velocity fluctuations	FA2
F2. SANDSTONE (35%)	**F2A. Massive, structureless Sandstone Beds with Graded Tops**	8%	Medium- to thick-bedded, moderately sorted, f to m sand. Most of the beds shows the absence of sedimentary structures, weekly stratified, and ungraded. Very-thin (<5cm) bed at the top.	Dewatering structures (dish-and-pillar) in the lower part, sub rounded/ rounded rip-up mudclast (up to 20 cm) near the top, erosional scours and flute cast locally	5cm, 30 – 120 cm, tabular, amalgamated, sharp to erosion and flute bases, sharp top	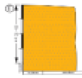	Deposition from sand-rich high-density turbidity currents where near-bed sediment concentrations and rapid aggradational rates	FA1, FA2
	F2B. Planar-stratified, Normally graded sandstone	12%	Thin- to thick-bedded, normally graded, ranging from m – vf sand with mud caps	Parallel lamination, normally-graded, or very minor portion cross-laminated, local bigradational present	10-60 cm, tabular, partly amalgamated, the base of the beds is sharp with sharp and gradational top		Waning turbulent flow from low-density turbidity current under upper-flow-regime plane-bed conditions	FA1, FA2, FA4
	F2C. Thin cross-stratified sandstone sets	7%	Thin to medium-bedded, vf to upper f sand, normally grading sets	(<5cm) sets of current ripples laminations, low angle (5') small-scale cross-stratification, trough cross-stratification. Locally angular to sub rounded mud clast occur.	10-40 cm, tabular to lenticular, sharp to erosional bases and sharp to gradational top, pinching out with small scour		Current ripples under lower flow regime	FA1, FA2
	F2D. Climbing ripple cross-stratified sandstone	5%	Poorly sorted, medium to thick-bedded (40 cm to 1m), vf to m sand, normally grading sets	Tabular cross-stratification (5'-15'), trough cross-stratification, and up to 10cm climbing ripples (15'-20'), and angular to sub rounded mud clast	40-100 cm, tabular, sharp to erosional bases and sharp top, pinching out with small scour		Climbing ripples/ Incipient dune stratification	FA1
	F2E. Hummocky Cross-stratified sandstone	3%	Poorly sorted, medium-bedded (30 cm), f to m sand	Decimetre-scale HCS, occurs axially at 3 generations/ bed stack, amalgamated sandstone packages, thickening up, h/l ratio about 0.25	30 cm, 0.2 m wavelength of low-relief formsets, base contact of the swale is a non-erosional surface		Ponded sandstone	FA1, FA4

Table 2.1 *(continued)*

F3. MUDSTONE (30%)	**F3A. Thin massive mudstone**	10%	Clay-rich (1:4 silt to clay), thin to medium bedded. Mineral composition shows >80% illite and/chlorite and 20% microcystalline qz	Indistinct textural, faint lamination, normally grading, absence of primary and secondary structures	3-20 cm, tabular (poorly-defined bed), sharp to gradational bases and sharp top	 Suspension fallout from dilute tails of turbidity flows	FA1, FA2, FA3, FA4
	F3B. Thick massive mudstone	12%	Siliceous:argillaceous is 2:1, green and red-purple, silt- and clay-sized, med- to thick bedded.	Lack of primary and secondary structures, locally developed faint lamination	30 to 110 cm, tabular (poorly-defined bed), sharp and non-erosive top and base	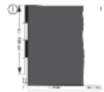 Rapid, sustained fallout of flocs from suspended sediment (Ponded turbidite)	FA4
	F3C. Laminated mudstone-siltstone	8%	Med- to thick-bedded, thin regular to irregular well sorted silt-mud laminae (<1cm). Ratio of silt and mud reaches 3:1	Irregular load structures, small scale of lenticular and indistinct wispy laminae (pin-stripe like), normally graded. Local Ediacaran fossil presents	30 to 100 cm, sharp to erosional top and sharp bases	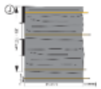 Sustained low velocity unidirectional currents with relatively weak bottom currents (deep sea current)	FA3, FA4
F4. HETEROLITHICS (5%)			Alternating sand, silt, and mud layers (2:1:1), rhythmic layers of thin laminae (1-2mm), moderately sorted, interbeds of thin- to med-bedded shale or mudstone. The silt content: 75-85%	Low-amplitude ripples, double mud layers, loading, elongate silt lenses with pinch out, lenticular. Organic matter is present. No bioturbation	5-15 cm, individual silt laminae discontinuous with pinch-out/onlap, distinctly lenticular. Sharp base and gradational to sharp top	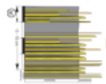 Reworked turbidites	FA3, FA4
F5. BOUMA SEQUENCE (TA-TE) (5%)			Complete Ta-Te (Bouma, 1962) in thin to thick bed, lower m to silt/mud	Normally graded, (Ta) poorly sorted, structureless, with a scoured base/ load casts (Tb) planar-laminated (Tc) ripple cross-laminated (Td) vf-f sand/ silt, often wispy planar-laminated (Te) pelitic silt/mud	10-40 cm, tabular, sharp base and sharp top	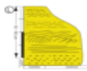 Sedimentation under progressive waning low-density turbidity currents. Partial Bouma sequence indicate turbidity current were by passed or eroded by following flows	FA3
F6. IRREGULAR POST-DEPOSITIONAL STRATIFICATION (8%)			Coarse silt- to med sand, moderately sorted, thin- to thick-bedded, comprises irregular sedimentary structures	Up to 20 cm length, dewatering structures (dish and pillar), vertical pipes, shrinkage cracks, convolute laminations, load structures, load casts, sand injectites, flute cast, and flame structures	10-80 cm, tabular to lenticular, sharp bases and sharp to gradational contacts	 Soft-sediment deformation of poorly consolidated sediment by liquefaction and fluidization in a high sedimentation rates	FA1, FA2

Table 2.1 *(continued)*

F7. TUFF (Volcanic Layers) (14%)	**F7A. Thin Crystal Ash Tuff**	2%	Microcrystalline, recrystallized ash size, white (weathers to brown), the layers approx. 1-3 mm thick, angular f-m, mod sorted, sand phenocrysts of fd (60%), qz, felsic lithic ash	Massive, absence of sedimentary structure, no bioturbation, burrow, or any fossil preservation	<3mm thick, well exposed on bedding plane, sharp base and sharp top	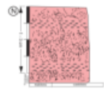	Volcanic fall-out ash formed by gravitational settling produced by multiple volcanic eruption events
	F7B. Vitric Lapilli Tuff	7%	Recrystallized, poorly sorted, coarse-grained ash or lapilli, small sub-circular lapilli to pebble size (2-64mm) of volcanic glass shard, rock fragments, and various phenocrysts	Structureless, flattened pumice lapilli, non-welded. Thinnest strata exhibit wavy and pinch-out	2-10mm thick, well-exposed on bedding plane and well-stratified in turbiditic beds, sharp base and sharp top	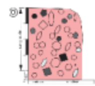	Deposited by both fall-out ash suspension and eruption-fed density currents, with varying degrees of suspended-load fallout rate, traction, and sorting
	F7C. Tuffite/ Tuffaceous Beds	5%	Yellowish to olive gray, fine sand to silt (<0.25mm), and very thin to medium bedded, clay-rich volcaniclastic sediments (50% volcanic-lithic grain)	Typically normally graded, parallel lamination, ripple and cross lamination, and erosional or scour base are rare	10-30 cm, amalgamation, interstratified with F2, F3, F5, sharp base and sharp top		Reworked and resedimented tuff by low-density turbidity current

Interpretation: Gravelly non-cohesive concentrated density flow

Due to the a-axis aligned fabric, relatively thin bedding, and normal grading of matrix, F1B is interpreted to record sedimentation from non-cohesive concentrated density flows (Alexander and Mulder, 2001; S2-S3 Lowe, 1982; Facies A2.4 of Pickering et al., 1986). Silt-sized matrix at the top of the bed records fallout from suspension due to near-bed velocity fluctuations (Pickering et al., 1986). This suggests that the flows associated with F1B were partly influenced by turbulence, and therefore may have developed continuously from hyperconcentrated density flows (F1A) (Alexander and Mulder, 2001).

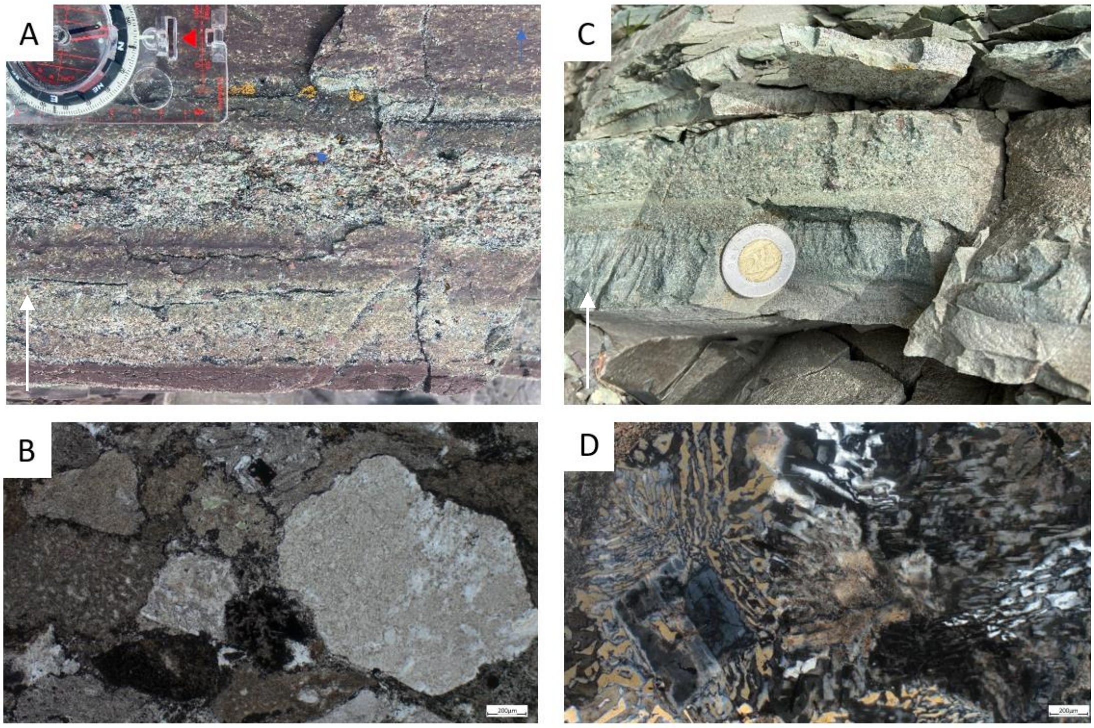

Figure 2.1 Conglomerate Facies (F1) (A) Thin (7 cm) granule-sized clast-supported conglomerate associated with the other two units (from bottom) interlaminated red mudstone and greyish pebbly sandstone **(B)** Micrograph (Sample T-28) shows poorly sorted clast supported (F1B) conglomerate **(C)** 10 cm, granule- to pebble-sized moderately sorted matrix-supported conglomerate (F1A) associated with the underlying units vc-c sandstone (white lines shows the erosional base contact) and sharply overlying by tuff and interlaminated c-m sandstone and mudstone **(D)** Micrograph (Sample PC-13) shows granophyric texture as igneous rock fragment. White arrow indicates younging direction or stratigraphic up.

Facies 2: Sandstone

Facies 2 (F2, Fig. 2.2, Table 2.1) constitutes about 35% of the measured sections. F2 is subdivided into 4 subfacies, including massive sandstone (F2A), planar-stratified normally graded sandstone (F2B), thin cross-stratified sandstone (F2C), and climbing ripple cross-stratified sandstone (F2D). F2 encompasses a variety of mineralogical compositions, including volcaniclastic lithic arenite, quartz arenite, and feldspathic wacke (classification of Dott, 1964).

F2A. Massive Sandstone Beds with Graded Tops

F2A is comprises 8% of the measured stratigraphy, and consists of grey, thin- to thick-beds (~5cm, 30 –100 cm) of moderately sorted, fine- to medium-grained sandstone. Beds lack sedimentary structures and are ungraded except for the upper ca. 5 cm of beds, which commonly grade normally upward to siltstone. Dish-and-pillar structures are present in the lower to middle part of the thick beds. Subrounded granule- to cobble-sized platy mud clasts occur locally within or near the top of beds. Beds are often amalgamated and have tabular geometries with sharp bases, minor erosional scours with flute casts of 5 cm depth (Fig 2.2A)

Interpretation: sedimentation from sand-rich high-density turbidity currents

The lack of stratification and occurrence of grading only at the tops of beds suggest deposition from sand-rich, high-density turbidity currents where near-bed sediment concentrations and fallout rates were high, and bed traction, selective deposition, and bedform initiation were inhibited (Lowe, 1982; Mutti, 1992; Kneller and Branney, 1995; Mulder and Alexander, 2001). The lack of sedimentary structures except for local dish and pillar structures and the dominance of fine sand size suggests rapid aggradation rates (Arnott and Hand 1989; Leclair and Arnott 2005; Talling et al. 2012a) from decelerating high density turbidity currents due to sudden loss of capacity or competency by gradual aggradation from sustained flow (Facies B1.1 of Pickering and Hiscott, 2015; S3 of Lowe, 1982) preventing any bedform development and trapping ambient fluid (Rotzien, 2014; Jamil et al., 2021). The mud clasts are lifted from the bed by shear and lift and then rise above the dense lower region of the flow, most likely due to buoyancy and progressive disaggregation between high-density and low-density flow (e.g, Mutti and Nilsen, 1981). The dish and pillar are additional signs that such high upward-directed pore pressures may have also driven mud clasts upward.

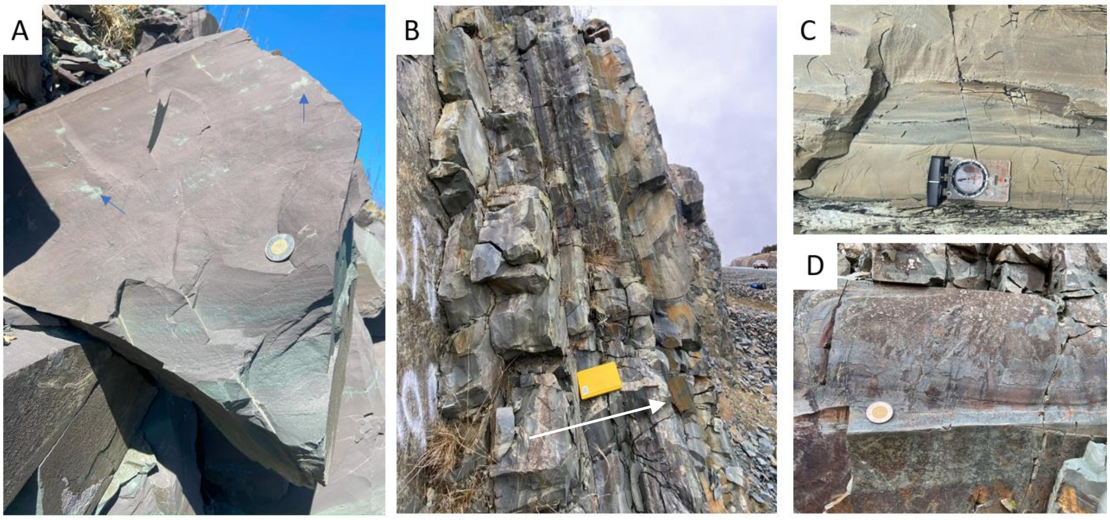

Figure 2.2 Sandstone Facies (F2) examined from outcrop-based **(A)** 35 cm normally graded sandstone from med sand to silt, capped sharply with 1 cm vf sand, mostly structureless with dewatering structures (blue arrow). Photo was taken at Trans-Canada Highway **(B)** Amalgamated massive and normal graded parallel-laminated sandstone, thinning upward, m to vf, with parallel lamination in the middle of 25 cm sandstone overlying the massive mudstone facies. Photo was taken at Brier Ave (Fig. 1.2) **(C)** Cross-stratified sandstone represented by climbing ripples and wavy laminae correlated with mudstone and massive sandstone. Photo was taken at Middle Cove **(D)** Trough cross stratification as a feature of F2D. Photo was taken at TCH 3. White arrow indicates younger direction or stratigraphic up.

F2B. Planar-Stratified, Normally Graded Sandstone

F2B makes up approximately 12% of the measured stratigraphy. It consists of green to light grey, thin- to thick- bedded (10-60 cm) normally graded planar stratified sandstone. The base of F2B beds are generally sharp and planar, without scouring, and tops of beds are gradational. F2A is predominantly normally graded with parallel laminated lower medium sand and rare coarse sand at their base grading upward to structureless very fine sand to mud.

Interpretation: waning upper-flow-regime of turbidity current

F2B was deposited from waning high-density turbidity currents under upper-flow-regime plane-bed conditions (Bouma, 1962; Allen, 1984; Talling et al., 2012) corresponding to the "Tb" division of turbidites, related to high near-bed shear stress conditions (Alexander & Mulder, 2001). For a very long time, it was believed that this structure were caused by low-density turbidity currents, which resulted in low sedimentation rates (Best and Bridge, 1992; Lowe, 1982; Mutti, 1992). It is now known, however, that horizontal lamination can develop from the same high-concentration flows as F2A, but following a decrease in bedload sediment concentrations and fallout rates (Leclair and Arnott, 2005). The upward gradation to mudstone further suggests fine-grained sediment fallout occurred during the terminal stages of these waning turbidity flows.

F2C. Thin Cross-Stratified Sandstone Sets

F2C constitutes about 7% of the measured stratigraphy and forms 10 cm to 40 cm thick bedsets of moderately sorted upper fine to very fine cross-stratified sandstone. Individual beds are typically normally graded. Bed geometries are tabular or lenticular with mostly sharp and erosive basal contacts and sharp tops. Internally, these beds comprise <5 cm sets of unidirectional low angle (15-20^{o}) cross-stratification of and associated asymmetric formsets. Angular to subrounded mud clasts occur locally.

Interpretation: Current ripples under lower flow regime

The thin sets of F2C and unidirectional character of the cross-lamination point to current ripple migration under low-energy unidirectional currents (Allen, 1984), and are related to the Tc division of the idealized Bouma turbidites (Bouma, 1962) and F9 of Mutti (1992). Accordingly, these ripples were deposited under decelerating turbidity currents over relatively low-concentration sandy non-cohesive bedload (Allen, 1968; Baas, 1999; Baas et al., 2019).

F2D. Climbing Ripple Cross-Stratified Sandstone

F2D constitutes about 5% of the measured stratigraphy and forms normally graded or ungraded bedsets 40cm to 1m thick consisting of poorly sorted very fine- to lower medium-grained sandstone. The average grain size is fine sand. Bed geometries are generally tabular, but with local low-relief asymmetric scours at their base, and sharp planar tops. Internally, F2D cosets are 20 cm thick consisting of 5-10 cm thick tabular cross-stratified sets of unidirectional moderate-angle cross-strata with preserved formsets, and stoss sides with angles of 10-20^{o}. Climbing sets of cross laminations can exhibit angles of climb of 5–20°.

Interpretation: Climbing ripple/ Incipient dune stratification

Based on (1) climbing ripple sets, (2) thickness of set and coset, and (3) grainsize dominance, F2D is interpreted as climbing ripple and incipient dune stratification. Ripple sets with climbing angles >15^{o} and stoss side dips <20^{o} are interpreted as supercritical climbing ripples and climbing angles <15^{o} are interpreted as subcritical climbing ripples (Allen, 1973; Hunter, 1977). The development of climbing-ripples requires suspended sediment fallout (Allen, 1973; Jobe et al., 2012) and coeval bedload transport, which typically occurs during decreasing turbulence intensity over relatively short distances, resulting in an abrupt loss of suspended load capacity (Hiscott, 1994; Kneller, 1995). The rare occurrence of relatively thick sets (~10 cm) suggests the formation of incipient dunes and therefore the periodic influence of coherent turbulence at the bed under relatively low suspended sediment concentrations (Arnott, 2012). The narrow grain size range and extensive climbing ripple cross lamination in the study area suggests abrupt flow deceleration, possibly as result of an abrupt decrease in degree of structural confinement, a decrease in down flow slope, or the flow encountering an up-flow dipping slope (Jobe et al., 2012).

F2E. Hummocky Cross-Stratification (HCS)-like Sandstone

F2E makes up approximately 3% of the measured stratigraphy. It mainly consists of decimetre-scale hummocky cross-stratification (HCS) occuring in the middle to upper MPF. Sets are up to 30 cm thick, with 0.2 m wavelength of low-relief formsets (Fig 3.1E). F2E's HCS occurs in three beds stacked vertically and consists of amalgamated sandstone packages. The geometry of lamina sets are well-preserved, consisting of a set of thickening up toward the top. Lateral variations in the thickness of laminae sets with an h/l ratio (height/ half width) about 0.25. The basal contact of the swale is a non-erosional surface and shows topographic depression resulting from hummock growth and fills by aggradation.

Interpretation: Ponded sandstone

The (1) decimeter-scale thickness of HCS, (2) non-erosional surface at the base of the swales, (3) fine-grained sand, (4) association with turbidites all indicate that F2E's HCS was controlled by oscillatory flow from internal shear waves in refracted turbidity flows, rather than from storms in a shallow marine setting (Mulder et al., 2009). Bypassing flows, which carried finer-grained sediment to the distal lobe, reflected against the basin margins or close to the basin margin producing complex internal oscillatory-flow patterns that deformed the aggrading deposits, producing HCS

(Pickering and Hiscott 1985; Tinterri et al., 2016; Cunha et al., 2017; Patacci et al., 2015).

Facies 3: Mudstone

Facies 3 makes up 30% of the measured sections and form regionally extensive strata associated with other lithofacies. Black greenish-gray, red, to bluish mudstone forms thin and thick massive (F3A, F3B) and laminated (F3C) fine-grained subfacies. Mineralogical compositions are mainly divided into two endmembers: clay-rich (argillaceous) and silica-rich (chert-like).

F3A. Thin Massive Mudstone

F3A comprises very thin- (3 cm) to thin- (20 cm) beds of clay-rich mudstone composed of mixed silt- and clay-sized sediment with a ca. 1:4 ratio of silt to mud. The mineralogical composition includes ~80% illite and/or chlorite and ~20% microcrystalline quartz. There is no preferred particle orientation or primary sedimentary structures (Fig. 2.3a). Sharp tops, and gradational to sharp non-erosive bases are typical. F3A usually caps strata of F2 and F4 with gradational contact.

Interpretation: Suspension fallout from dilute tails of turbidity flows

The thinness of beds, homogeneous, and structureless fabric of F3A suggests deposition by fallout from suspension by the dilute tails of low-density turbidity currents (E3 division of Piper, 1978; T7 of Stow and Shanmugam, 1980; Mulder and Alexander, 2001; Daele et al., 2017). F3A, which contain a mixture of illite and quartz, was brought to the basin by weathering and transport, implying terrigenous sources, even if the weathered rocks were volcanic in origin.

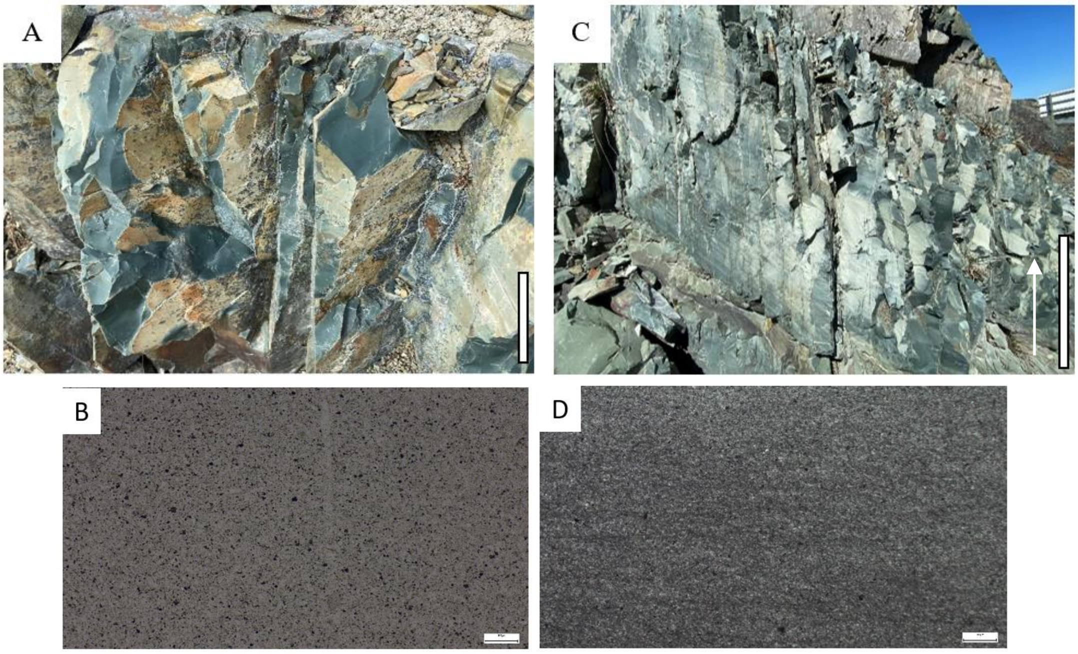

Figure 2.3 Mudstone Facies (F3) (A) Si-rich, massive mudstone facies (F3A). Photo was taken at Airport Heights (Fig 1.2) **(B)** Photomicrograph PPL, massive mudstone (F3A) shows the lack of internal structures. White bar equals to 1 m **(C)** laminated mudstone facies (F3C). Photo was taken at TCH 3 **(D)** Photomicrograph PPL, fissile-looking, clay-rich laminated mudstone shows faint wavy-lenticular lamination (F3C)

F3B. Thick Massive Mudstone

F3B is volumetrically abundant (almost 50% of mudstone distribution) and comprises medium (30 cm) to very thick (110 cm) beds of siliceous mudstone and lesser clay-rich green and red-purple mudstone composed of mixed silt- and clay-sized sediment with a ca. 1:2 ratio of silt to clay. The siliceous mudstone or chert-like mudstone is more abundant than clay-rich mudstone at a ratio of about 2:1. Primary structures are absent except for a locally developed faint planar lamination (Fig. 2.3). Typically, the top and base of beds are sharp, and non-erosive. The mineralogy of siliceous mudstone includes ca. 90% cryptocrystalline quartz, <10% clay (chlorite, smectite), and minor fine disseminated epidote. The subordinate clay-rich mudstone comprises >80% illite and/or chlorite and microcrystalline quartz for less than 20%.

Interpretation: Ponded turbidite

Due to the thickness of beds and ungraded massive structure, and absence of evidence of liquefaction, F3B is interpreted as the product of rapid but sustained fallout of flocs from suspended sediment in distal turbidity flows (Potter et al. 1980; O'Brien and Slatt 1990; Partheniades 1990). Accordingly, F3B is interpreted as thick mud caps deposited from ponded turbidity flows refracted off of basin margins (Sinclair and Tomasso, 2002; Lomas and Joseph, 2004; Patacci et al., 2015). These ponded mudstones likely formed by upslope flow of turbidity currents onto bathymetric highs (Muck and Underwood, 1990). The abundance of siliceous (chert-like) mudstone suggests that most of these ponded turbidites were sourced from fresh volcanic and/or volcaniclastic sources.

F3C. Laminated Siltstone/Mudstone

F3C comprises laminated mudstone that forms laterally persistent medium- to thick-beds (30 to 100 cm) of very thin (<1 cm) well-sorted siltstone and mudstone interlaminations (Fig. 2.3). Distinct mm-scale pinstripe-like laminations are common, and at the microscopic scale exhibit sharply defined, slightly irregular ("crinkly") lenticular concentrations of silt (Fig 2.3D). F3C beds commonly have sharp tops and sharp to gradational bases. The ratio of silt to mud is 1:1 to 3:1. In some beds, silt laminae are underlain by load structures. Thin laminae of volcanic ash (F7A) occur within these laminated mudstone beds.

Interpretation: Sedimentation under deep-sea currents

Planar laminae of silt and mud that are only a few mm thick are common features in the deep marine but their origins are not well understood. It has been speculated that these may be the result of hemipelagic sedimentation (Te Bouma 1962; O'Brien et al., 1980) or multiple turbiditic event with varying energy (Moore, 1969; O'Brien et al., 1980). According to Benus (1988) and Jenkins (1992), facies similar to F3C strata represent sedimentation the ‘background’ environment in which Ediacaran organisms lived under low rates of sedimentation. These processes may be best described by a flume experiment by Yawar & Schieber (2017), suggesting that as turbid suspensions of clay and silt travel over long distances under sustained low velocity (20 cm/s) unidirectional currents; coarser silt destabilizes floccules and accumulates at the bed surface forming silty lamina, whereas fine silt remains in suspended clay flocs and becomes part of overlying silty mudstone. This low velocity unidirectional flow related are considered to be similar or resembling contour current. Similar reworked facies host frondose Ediacaran organisms in other parts of the Mistaken Point Formation, with their preferred orientations interpreted to be controlled by bottom current flow directions (Narbonne et al., 2001; Wood et al., 2003; Ichaso et al., 2007; Mason et al., 2012).

Facies 4. Heterolithic Facies

F4 constitutes about 5% of the measured stratigraphy and comprises thin (5cm) to medium (15cm) beds of moderately sorted interlaminated sand, silt, and mud. Beds of F4 have sharp bases and gradational to sharp tops. F4 displays rhythmic mud and silt laminae occasionally interstratified with fine-grained sandstone laminae. Thinly laminated black mudstone containing organic matter is present locally. Individual laminae are <1 mm to 5 mm thick, and the relative laminae thicknesses of sand:silt:mud is approximately 2:1:1. Sandstone laminae are laterally discontinuous elongate lenses with pinch-out/onlap terminations onto underlying mudstones, and laminae <2mm thick pinch and swell over <30 cm along strike. Sandstone commonly have erosional contacts or load structures at their base. Most sandstone laminae are internally parallel laminated, but rare (20% of bed; Fig 2.4) low amplitude heterolithic cross-laminated ripple formsets and lenses are also present.

Interpretation: Reworked turbidites

The (1) lateral discontinuity of the laminae, (2) the presence heterolithic ripple and low-angle cross lamination formsets, (3) abruptly partitioned grain size (mud and fine/lower medium sand), and (4) well-developed mm-scale mud layers in sand-silt (inferred as 'double mud layer' by Shanmugam, 2021), F4 are not typical characteristics turbidity current deposits (Bouma, 1962). Instead, these characteristics are of turbidites reworked by bottom currents (Klein, 1975; Shanmugam, 2013). This process is commonly developed in fringe to distal fringe lobe systems (Fig 3.1).

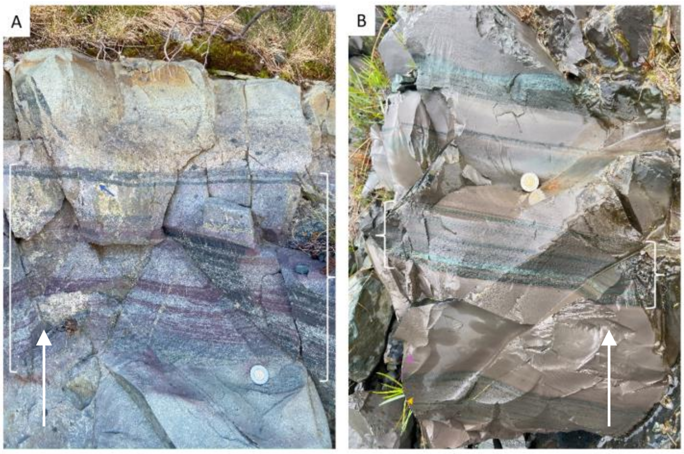

Figure 2.4 Heterolithic Facies (F4) (white brackets) **(A)** Medium-bedded interlamination between red mudstone, dark grey siltstone, and greyish fine sandstone, with black organic-rich on top of the facies (blue arrow). F4 then overlain by yellowish normally graded tuffaceous sandstone **(B)** Thin-bedded interlamination between dark grey mudstone, greenish siltstone, and dark grey fine sandstone. F4 here associated with thin dark red massive mudstone (pink arrow) and planar laminated sandstone (yellow arrow). White arrow indicates younger direction or stratigraphic up.

Facies 5. Bouma Sequence (Ta-Te)

Facies 5 constitutes about 5% of the measured sections and consists of complete T_a-T_e of the Bouma Sequence (Bouma, 1962) forming 10-40 cm thick beds. The five divisions that make up this facies from bottom to top are 1) fine- to lower medium-grained, poorly sorted, structureless sandstone, often with a scoured base and/or load casts (T_a); 2) fine-grained, planar-laminated sandstone (T_b); 3) fine-grained small-scale cross-laminated sandstone (T_c); 4) fine sand to silt, often wispy planar-laminated (T_d); 5) and massive silt and mud (T_e).

Interpretation: Sedimentation under waning low-density turbidity currents

Overall, complete T_a-T_e divisions record the sedimentation under a progressively waning turbidity currents from relative high-concentration high velocity to low-concentration and low velocity near-bed conditions (Bouma 1962). The relatively fine grain size (coarse silt – fine sand) suggests a near-bed low-density turbidity flows (Stow and Bowen, 1980; Stow, 1985).

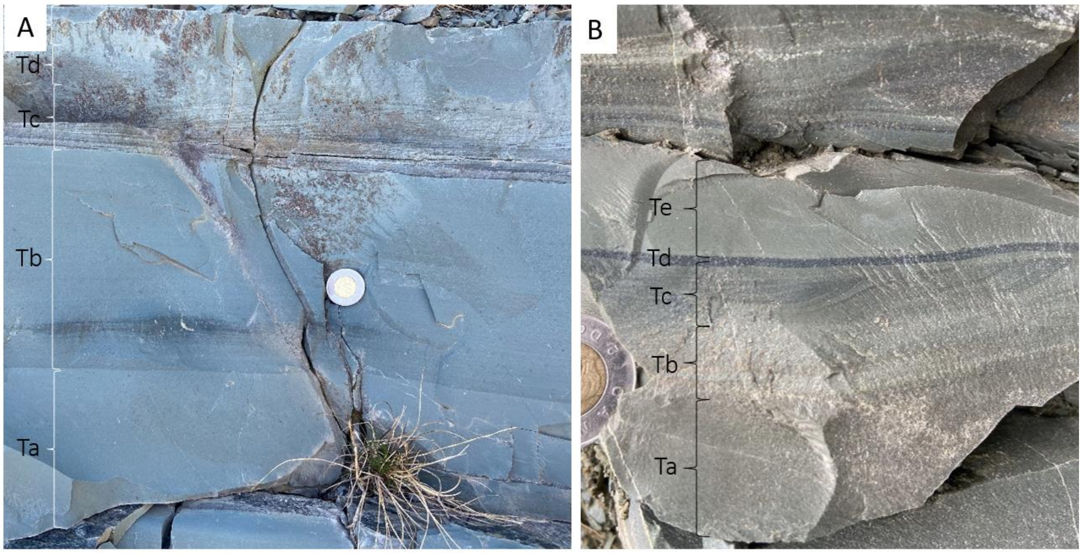

Figure 2.5 Ideal Bouma Sequence (F5) (A) Medium bedded (30 cm) of Ta-Te located in Team Gushue Highway 3 **(B)** Thin bedded (<10cm) Bouma sequence in small scale (Ta-Te) located in Brier Ave. Location details in Fig 1.2.

Facies 6. Irregular Post-Depositional Stratification

Facies 6 constitutes about 8% of the measured sections and comprises irregular sedimentary structures clearly post-dating earlier stratification, including dish and pillar, vertical pipes, shrinkage cracks, convolute laminations, load structures, load casts, sand injectites, and flame structures. Most of F6 occur in thin- (10 cm) to thick- (80 cm) bedded moderately sorted coarse siltstone to lower medium sand. Most of these irregular sediment structures extend laterally over less than 15 cm, except for convolute laminations which commonly more than 20 cm in length. Characteristically, the intensity of folding of convolute lamination increases upward from the undeformed bed, such as F2A, and the wavelength of folding with the thickness of the bed or deformed layer. The beds containing F6 are tabular to lenticular, have sharp bases and sharp to gradational upper contacts (Fig 2.6).

Interpretation: soft-sediment deformation

Features of F6 are interpreted as products of soft-sediment deformation caused by liquefaction and fluidization processes (e.g., Mills, 1983; Tasgin and Altun, 2019). Convolute laminations are formed by the liquefaction and deformation of unlithified sand (Tasgin and Altun, 2019), which in turbidites is often triggered by bed-scale density inversions (Gladstone et al., 2017) or sediment loading (e.g., Al-Mufti and Arnott, 2020) enhanced by high local rates of sedimentation that facilitate high pore fluid saturation. Dewatering structures such as vertical pipes and dish-and-pillar structures were formed by subsequent fluidization of sand and silt during liquefaction and dewatering of underlying strata (Owen, 1987; Stow and Smillie, 2020). Overall, F6 indicates high sedimentation rates, leading to deposits with open grain packing, fluid saturation, and sediment loading that has led to subsequent fluidization and liquefaction processes in poorly consolidated sediment.

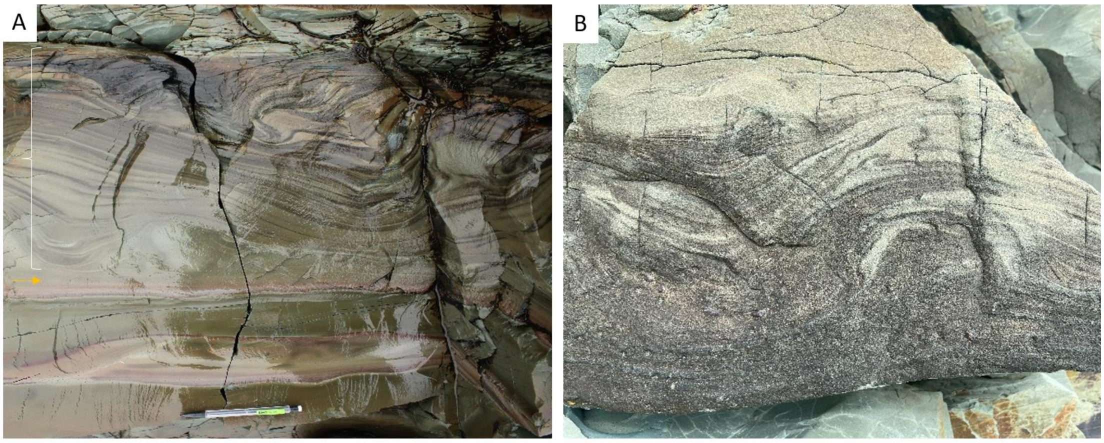

Figure 2.6 Irregular Post Depositional Stratification Facies (F6) by Soft-sediment deformation **(A)** Thin laminar parallel lamination (*yellow arrow*) overlain by fine-grained convolute lamination sandstone **(B)** Convolute bedding medium-grained sandstone. Both photos are located in Middle Cove coast.

Facies 7: Tuff (Volcanic Layers)

Facies 7 constitute around 14% and is well-developed throughout the MPF, particularly in the lower member, making up about 14% of the entire measured stratigraphic thickness. F7 is divided into crystal ash tuff (F7A), vitric lapilli tuff (F7B), and tuffite (F7C), based on tuff composition (Pettijohn, 1975) and texture.

F7A. Thin Crystal Ash Tuff

F7A mainly occurs in the lower member of MPF. It forms white or weathered to light- to dark brown, 1-3mm thick strata consisting of microcrystalline, recrystallized ash (≤2mm size; based on the scheme of Tucker, 1982) traceable over 100 m along strike. It consists of internally massive strata of moderately sorted, silt-sized angular crystal ash. F7A beds contain ca. 60% feldspar (K-feldspar and plagioclase) and 40% embayed quartz crystals and felsic lithic ash, such as microcrystalline Qz, chlorite, and glass shards (Fig 2.7A). This subfacies is well exposed on bedding surfaces, interlaminated with or capping F3. F7A strata have sharp lower and top contacts, and layers are abruptly intercalated with unrelated facies such as parallel laminated sandstone and massive mudstone.

Interpretation: Ash Fall-out

These thinly laminated and laterally continuous tuff strata with their internally consistent grain size distributions and abrupt intercalation with unrelated facies are interpreted as volcanic ash fall-out formed by gravitational settling of windblown ash produced by volcanic eruptions from adjacent eruptive centres (Carey, 1997; Wetzel, 2000; Goswami and Dey, 2018; Dodd et al., 2020). The relative continuity and abrupt intercalation of thin ash layers with clastic facies suggest rapid settling of ash from suspension (Sohn et al., 2008). The ash is a key component of what Narbonne et al. (2005) called Conception-style preservation of Ediacaran fossils.

F7B. Vitric Lapilli Tuff

F7B is composed of poorly sorted lapilli (2-64 mm; based on the scheme of Tucker, 1982) consisting of recrystallized volcanic glass shards, rock fragments, and crystals. Strata of F7B are 2-10mm thick. Locally flattened lapilli, likely flattened pumice, are exposed on bedding surfaces, composed of non-welded, sand- and silt-sized pyroclastic detritus. The thinnest strata (<5mm) exhibit wavy structures and pinch-outs, are composed of lapilli (Fig. 2.7B, D), and are interstratified with sandstone (F2) or mudstone (F3A, C). F7B strata are abruptly interstratified with unrelated sedimentary facies and have sharp bases and tops. The largest angular clast flattened clast has an a-axis of 3cm.

Interpretation: Suspension fall-out and eruption-fed density current

The lateral pinching-out, lack of sedimentary structures, and abrupt contacts of these strata suggests deposition by both suspension fallout and eruption-fed density currents, with varying degrees of suspended-load fallout rates, traction, and sorting (Sohn, 1997; Kneller and Branney, 1995; White; 1996, 2000). The impingement of these vertical density currents on a sloping seafloor led to a lateral translation from high- to low-density turbidity currents (Manville and Wilson, 2004). In comparison with F7A, F7B are interpreted to have been sourced from closer, possibly subaqueous, volcanic centres.

F7C. Tuffite/ Tuffaceous Beds

F7C consists of 5 to 30 cm thick beds of yellowish to olive grey, volcaniclastic fine sandstone to siltstone. F7C is moderately sorted and is composed largely of volcanic grains: 50% pyroclastic including volcanic-lithic grains, recrystallized glass shards, altered pumice grains, polycrystalline quartz and orthoclase feldspar, and clay minerals. F7C beds are typically normally graded and laterally continuous over at least 4 km, with sharp basal and upper contacts. Parallel and cross lamination occur but are rare, as are basal scours. These beds are commonly amalgamated and interstratified with turbiditic facies such as F2A, F2B, F2D, F3A, and F5 (Fig 2.7C, E).

Interpretation: Reworked and resedimented tuff

F7C is interpreted as fresh volcanic tuffaceous material that was reworked by low density decelerating turbidity flows, forming volcanoclastic turbidites deposited during and between eruptions (ash-turbidites by dilute turbidity currents of Wright and Mutti, 1981; see also Dodd et al., 2019b; White, 2000). The abundance of siliciclastic material and the close association with turbidites (F2, F3, F5) suggests significant admixing during transport.

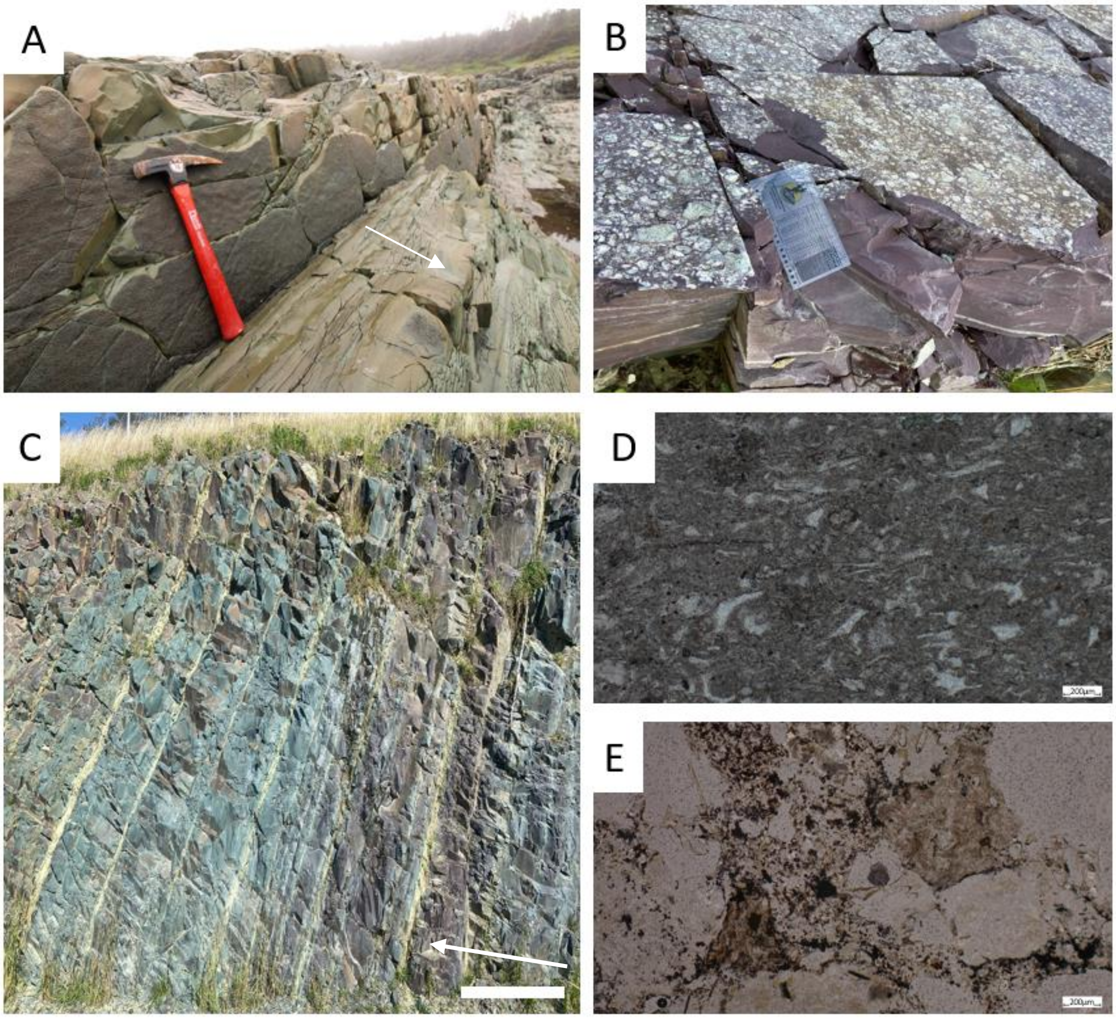

Figure 2 7 Tuff and Tuffaceous Facies (F7) (A) Crystal ash tuff F7A located in Middle Cove coast **(B)** Phenocryst stratified lapilli tuff facies **(C)** Tuffaceous beds. Photos B and C were taken at Hyundai outcrop. White block identifies 1 m scale. **(D)** Micrograph (Sample C3-43) PPL - Slightly altered volcanic glass shard, Y—shaped and curved forms are well-preserved. Biotite phenocryst is visible **(E)** Micrograph (Sample C3-43) XPL - Crystal-vitric tuff, contain altered plagioclase. White arrow indicates younger direction or stratigraphic up.

CHAPTER III - FACIES ASSOCIATION AND ARCHITECTURE

Seven facies (F1-F7) and fifteen subfacies are grouped into four facies associations (FA1–4). Facies associations FA1-FA4 are interpreted with respect to deep-marine fan environments, based on the abundance diversification of facies and turbidity currents, lobe-like architectural elements, and context from previous work (Williams and King, 1979; King, 1990; O'Brien and King, 2004). Facies from the previous chapter are here combined with paleocurrent readings, architectural analysis, thin section petrography, and SEM-EDX analysis. Qualitative and semi-quantitative field observations, including the characteristics and distribution of lithofacies, bed geometries, and stacking patterns, are observed and summarized in Table 3.1. Specifically, each facies association is interpreted with respect to unique *lobe elements* (FA 1-4; Appendix C, see a five-fold hierarchy of lobes follows a nomenclature by Prelat et al., 2009) which here represented by amalgamated tabular sandstone bed sets (FA1), interbedded sandstone and mudstone (FA2), tabular to lenticular heterolithic bed sets (FA3), thick massive mudstone and HCS-like structures (FA4).

FA1: Amalgamated Sandstone

FA1 is characterized by 0.8-6 m thick amalgamated bedsets consisting internally of very fine to lower medium-grained sandstone beds (F2, ~80% of measured FA1), interstratified with tuff (F7a-b, ~10%) minor mudstone (F3a; ~7%) and minor soft-sediment deformation (F6, ~3%), and contains the highest proportion of sandstone of all facies associations. FA1 amalgamated bedsets are laterally continuous and consist of thinning- and thickening-upward successions of beds. They dominantly consist of 0.4 to 1.2 m thick sand-rich, high-density turbidity current strata (F2a, more than 40% of measured FA1) locally containing granule-sized mud clasts and dewatering structures. F2a beds are interstratified with the others sandstone facies, including 0.5-1 m scour-and-fill climbing ripple to incipient dune stratified sandstone (F2d, ~25%) and minor 0.1-0.6 m upper plane bed strata (F2b, ~15%). FA1 amalgamated bedsets are capped by very thin-beds (<10cm) of mudstone deposited at the tails of surge-like turbidites (F3a, ~7%). Rare very thin beds (<3mm) of stratified ash and lapilli tuff facies of volcanic ash fallout (F7a-b, ~10%) occur between the amalgamated bedsets of F2a with sharp contacts. FA1 is commonly observed in the basal to middle sections of the Mistaken Point Formation and are well exposed in Middle Cove and along the lower parts of the Gushue Highway section (Fig 1.2B). Beds are tabular and laterally continuous at outcrop scale, and generally have sharp basal contacts with only minor erosion (<10 cm) except for rare local scours (>1.5 m) and load casts. FA1 tends to be overlain by FA2 or FA3.

Interpretation: Lobe axis

Based on the (1) amalgamation of medium to thick bedsets of sandstone facies with (2) low mud content, and (3) lack of sedimentary structures, FA1 records a sedimentation from highly concentrated turbidity currents with high local aggradation rates due to a sudden loss of flow capacity. The predominance of (1) a high degree of bed amalgamation, (2) tabular geometries, and (3) coarse, high-density turbidty flow facies demonstrate that they are associated with axial/ proximal positions in depositional lobes (see Mutti & Normark, 1991; Prelat & Hodgson, 2013; Spychala et al., 2017). Thick, ungraded, massive beds with soft sediment deformation in the lower parts of FA1 bedsets suggest rapid sedimentation through collapse and continuous aggradation high-density turbidity currents (Kneller, 1995; Kneller & Branney, 1995), which may have been triggered by a sudden decrease in local slope, loss of structural confinement, and/or running upslope of turbidity currents. The minor deposition of surge tail mudstone as a cap of FA1 supports proximal interlobe where materials build up between an avulsion from and back to the same point, similar to the overbank in fluvial systems.

FA2: Sandstone Interbedded with Soft-Sediment Deformation and Mudstone

FA2 is characterized by 3.5-5 m thick tabular bedsets of 0.3-1 m beds of sandstone and mudstone facies. These bedsets consist of interbedded very fine- to fine-grained planar- and cross- stratified sandstone (F2b-c, ~55% of measured thickness of FA2), irregular post-depositional stratification (F6, ~17%), massive mudstone (F3a, ~15%), minor massive sandstone (F2a, ~5%), minor granule-conglomerate (F1, ~3%), and tuff facies (F7, ~5%). Compared to FA1, beds are thinner, and the sand-to-mud ratio is lower (~60% of thickness composed of sandstone), and there is less amalgamation of sandstone beds. The succession of a typical FA2 bedset, from bottom to the top, consists of basal tabular to lenticular beds of soft-sediment deformed sandstone (F6, 0.3-0.8m), succeeded by thin beds of massive sandstone deposited under high-concentration turbidity flows (F2a, ~5cm), then planar stratified sandstone formed under a high aggradation rate and high near-bed shear stress conditions (F2b, ~0.3-0.6 m), and capped by <5cm thick sets of current ripple cross-strata, recording sedimentation under relatively dilute, low-energy turbidity currents (F2c, ~0.1-0.4 m). Massive mudstone (F3a, 3-20cm beds) deposited as a tail of surge-like turbidites commonly overlie sand-rich bedsets. Also, in FA2 are rare < 10 cm-thick non-cohesive concentrated-density gravelly flow deposits (F1a-b, ~3%, <10cm) which are interstratified with low-density turbidity current deposits (F2b-c) and mainly overlain by fine turbidites of (F3a) with sharp lower and upper contacts. F1 is rare (2-3 beds throughout FA2) but laterally persistent throughout the succession, (up to 10 km along-strike), making them reliable marker beds. Tuff facies (F7a-b, <10mm beds, ~5% of FA2) occur locally between and near the top of F3a bedsets. Bed contacts frequently have sharp to slightly erosive bases, load structures, and sharp tops. Beds in FA2 bedsets usually is thin upward.

Interpretation: Off-axis to proximal fringe lobe deposits

The sharp to erosive basal bed contacts, generally tabular bed geometries, high sand content, abundance of fluidization features, and evidence of successively turbidity flows in FA2 bedsets suggest that these bedsets represent individual lobe deposits with successively decreasing near bed sediment concentrations and velocities prior to and/or during lobe abandonment (Prelat et al., 2009; Zhang et al., 2017). Massive mudstone (F3a) capping these lobe deposits are interpreted to record inter-lobe sedimentation (Prelat et al., 2009). The predominance of planar-(F2b) and ripple-stratification (F2c) shows that FA2 beds were deposited by waning unidirectional turbulent flows transitioning from upper to lower flow regimes which were able to generate stratification and bedforms. Similar thin bedded, ripple stratified sandstones are commonly identified in lobe fringe deposits (e.g., Prelat et al., 2009; Grundvåg et al., 2014; Marini et al., 2015; Spychala et al., 2017). Compared to FA1, FA2 has a finer grain size, relatively low degrees of bed amalgamation, and less mudstone (F3a), which point to a more off-axis or basinward environment than FA1, referred to as off-axis lobe (see Mutti & Normark, 1991; Prelat et al., 2009; Prelat & Hodgson, 2013). The dominance of liquefaction and fluidization processes (F6) in the lower sections of FA2 are linked to high rates of sediment aggradation grain size control (Tinterri et al., 2017). The occurrence of continuous thin non-cohesive F1 deposits within FA2 is indicative of the local development in the presence of highly concentrated bedload layers. The presence of a fine silt matrix at the upper part of the F1 layer can be attributed to sediment settling from suspension In summary, FA2 was deposited by waning high-to-low density turbidity currents in an off-axis or lobe fringe position. The characteristic stacking pattern of FA2 bedsets with progressively thinner beds upward from progressively more dilute flows relates to upstream avulsions or shallowing and widening of feeder channels during progressive abandonment (Mutti & Ricci-Lucchi, 1975) and/or decreasing sediment supply from a feeder channel during lobe abandonment.

FA3: Mudstone Interbedded with Siltstone and Sandstone

FA3 is characterized by recurring 0.4-6 m thick tabular to wavy bedsets consisting of mudstone interbedded with heterolithic sandstone-mudstone-siltstone laminae, and minor sandstone. Within each bedset, these facies occur within four architectural elements: tabular thin-to-medium bedded mudstone (F3b-c, ~57%), amalgamated thin to medium tabular Bouma turbidite beds (F5, ~15%), tabular normal graded and cross-stratified sandstone (F2b-c, ~12 %), lobate to tabular thin heterolithic facies (F4, ~10%) and normally graded tuffaceous sandstone (F7, ~6%). Tabular normal graded and cross-stratified sandstone occurs at the base of each bedset and consist of 0.1-0.3 m thick beds of tabular fine-grained low-density turbidites (F2b-c). These are succeeded by ca. 20 cm of low-density turbidity current deposits (ideal Bouma sequence, F5), then typically by an erosive contact overlain by <15 cm of lobate to tabular thin heterolithic reworked turbidite facies (F4, Fig 2.4). Tabular reworked and resedimented tuffaceous sandstone beds (F7c, 0.1-0.3 m) are commonly associated with mudstone in FA3 bedsets with sharp basal and upper contacts. Fall out crystal ash-lapilli tuff (F7a-b, <5mm) are less common. Fine-grained deposits of deep-sea currents (F3c, 0.1-0.4 m, ~30% of the measured FA3) occur near the middle to top some FA3 bedsets, where a few Ediacaran fossils have been discovered on bedding surfaces by Olschewski (in preparation). Thick siliceous-argillaceous mudstone deposited by ponded turbidites (F3b) commonly cap

FA3 bedsets. FA3 bedsets have good lateral continuity, being correlated over 10 km from the northeast to the south of the study area (Figure 4.1, Figure 1.2). Over this scale, FA3 bedsets exhibit either narrowing or pinching geometries. Of all associations, FA3 has the least amount of sand and highest proportion of silt and mud, and consists of the thinnest bedsets of any other facies association.

Interpretation: Distal lobe deposits

Similar extensive thin-bedded successions with fining stacking patterns have been interpreted as the distal fringes of lobes, originally referred to as "*interlobes*" by Prelat et al. (2009). The thin-bedded, sharp-based, and normal graded siltstone and sandstone beds (F2, F3; Table 1) are interpreted as terminal fall out and tractional deposition from depletive waning turbidity currents (e.g. Bouma, 1962; Mutti, 1992; Kneller, 1995). The low concentration and density of these turbidity currents allowed them to traverse gradient changes associated with depositional relief across the pre-existing axis and off-axis lobe deposits (Groenenberg et al., 2010). Upward bed thinning in FA3 bedsets may indicate either lobe/fan retreat (i.e., retrogradation; *(Figure 4.2)*), across-strike lobe/fan shifting (i.e., avulsion), or a combination of both (Prélat & Hodgson, 2013; Spychala et al, 2017). The tabular to wavy geometries with minimal or rare bed amalgamation, predominance of mudstone and siltstone compared to FA1 and FA2, the presence of complete Bouma sequences, and the local occurrence of Ediacaran fauna all indicate that FA3 records sedimentation at the most distal parts of lobes with 'background' reworking by deep marine bottom currents (Narbonne et al., 2001; Shanmugam, 2013; Spychala et al., 2017). Moreover, the significant occurrence of ponded turbiditic mudstone and variable paleo-current directions in primary and reworked turbidites suggests sedimentation under dilute flows that have been reflected off the local confined topography (Kneller et al., 1991; McCaffrey and Kneller, 2001; Patacci et al., 2015).

Tabel 3 1 The overall distribution of lithofacies in each facies association, divided into three sections ranging from rare to abundant. FA1 and FA2 are dominated by F1 and F6. F2 and F7 relatives are found in all facies associations, but are more common in FA1 and FA2, whereas F2E, F3, F4, and F5 are abundance in FA3 and FA4.

FACIES DISTRIBUTION, ASSOCIATION, AND INTERPRETATION		F1: Conglomerate		F2: Sandstone					F3: Mudstone			F4. Heterolithics (sand-mud-silt)	F5. Bouma sequence	F6. Irregular Post Depositional	F7: Tuff		
		F1A	F1B	F2A	F2B	F2C	F2D	F2E	F3A	F3B	F3C				F7A	F7B	F7C
		Gravelly non-cohesive hyper-concentrated density flows	Gravelly non-cohesive concentrated density flow	Sedimentation from sand-rich high-density turbidity currents	Waning upper-flow-regime of turbidity current	Current ripples under lower flow regime	Climbing ripple/ Incipient dune stratification	HCS formed under reflected turbidity currents	Suspension fallout from dilute tails of turbidity flows	Ponded Turbidite	Sedimentation under deep-sea currents	Reworked turbidites, limited erosion	Sedimentation under waning low-density turbidity currents	Soft sediment deformation caused by liquefaction & fluidization	Ash fall out	Suspension fall-out and eruption-fed density current	Reworked and resedimented tuff
FA1: Amalgamated Sandstone	Lobe axis																
FA2: Sandstone Intbd with SSD and Mudstone	Off-axis to proximal fringe lobe deposits																
FA3: Mudstone Intbd with Siltstone and Sandstone	Distal lobe deposits																
FA4: HCS-Like CS Sandstone Intbd Thick Mudstone	Ponded Turbidites																

Absent/Rarely occur (<5%)

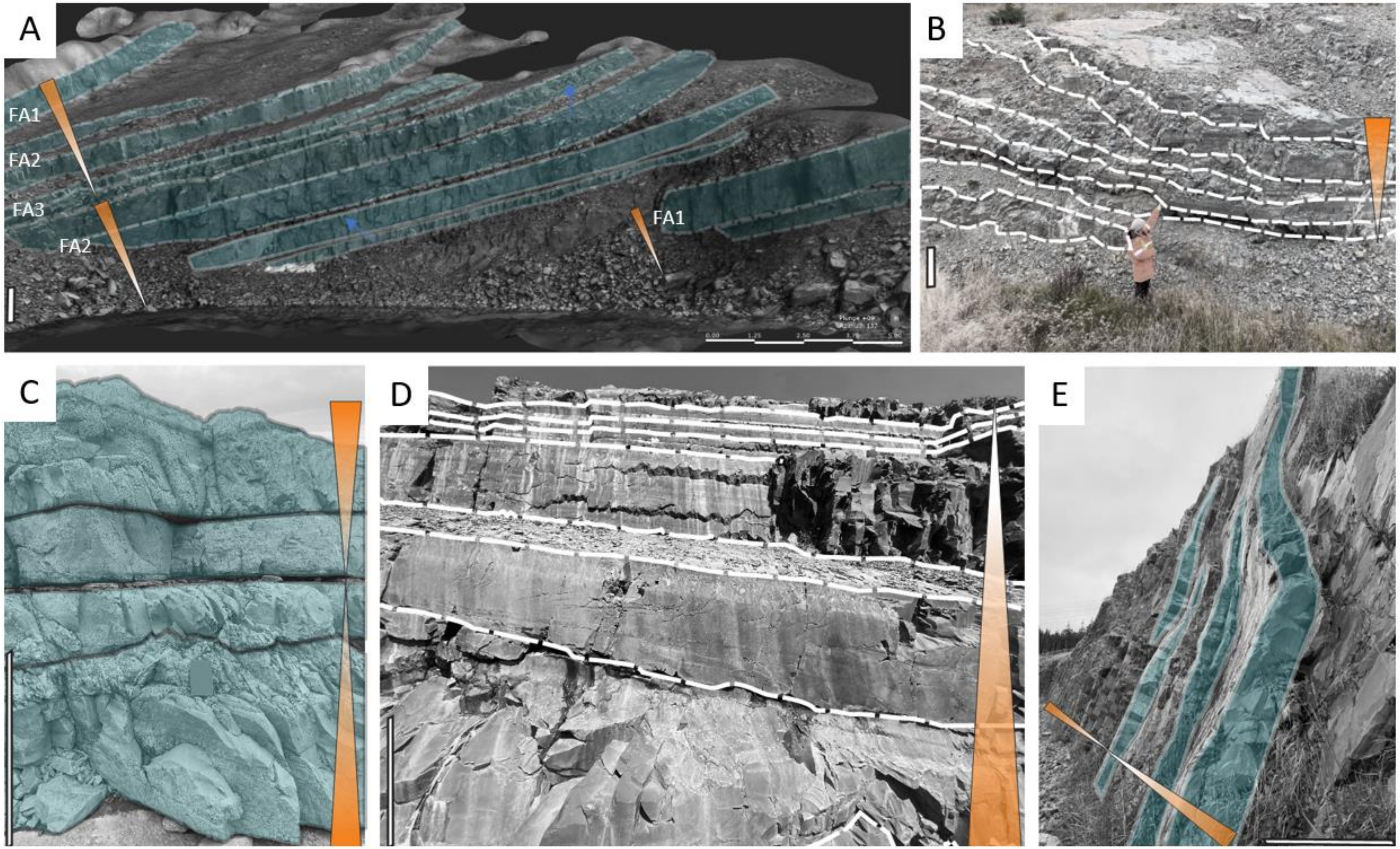

Figure 3.1 Architectures and interpretation with overall staking patterns of the measured Lobe and Lobe Complexes **(A)** It is at approximately 8 m stratigraphic height of lobe axis (FA1) to distal lobe (FA3) **(B)** Lobe fringe (FA2) with erosional contacts, thickening upward **(C)** Lobe axis (FA1) shows thinning and thickening upward **(D)** Off axis to Proximal Lobe Fringe (FA2) shows thinning upward **(E)** HCS-like sandstone (FA4) shows 3-4 vertical generations. The white rectangular scale represents one meter. Dashed lines represent bedding planes.

FA4: HCS-Like Cross-Stratified Sandstone Interbedded with Thick Mudstone

FA4 mainly consist of scoured/ HCS-like sandstone (F2e, ~35%), thick cross-stratified sandstone (F2d, ~22%), planar-stratified and normally graded, upper fine to very-fine sandstone (F2b, ~12%), thick mudstone (F3b, ~25%), and minor tuff (F7a, ~6%). FA4 bedsets are laterally discontinuous and consist of thinning- and thickening-upward successions of beds. Unlike the other facies association, FA4 lack of bed amalgamation and are limited to the western and southwestern reaches of the study area. They dominantly consist of 0.3 m thick sand-rich, HCS-like sandstone strata (F2e) indicating reflection of turbidity currents. F2e beds are interstratified sharply with the others sandstone facies, including 0.5-1 m scour-and-fill climbing ripple to incipient dune stratified sandstone (F2d, ~25%) and minor 0.1-0.3 m upper plane bed strata (F2b, ~15%). These sandstone facies are commonly overlain by thick to very thick ponded mudstone (F3b, 0.8-1.2 m) indicate the upper most part of of FA4. Rare very thin beds (<3mm) of stratified ash and lapilli tuff facies of volcanic ash fallout (F7a-b, ~6%) occur between the sandstone bedsets with sharp contacts.

Interpretation: Confined lobe fan

The (1) the majority of decimeter-scale thickness of F2e, (2) non-erosional surface at the base of the swales, (3) association with turbidites all indicate that FA4 sedimentation occurred in a confined basin setting, allowing for the deposition of ponded turbidites and the generation of oscillatory currents. As a major deposit in FA4, F2d is commonly formed where the slope gradient abruptly decreases (Bursik and Woods, 2000) or when confinement is lost (Walker, 1967). Bypassing flows, which carried finer-grained sediment to the distal lobe, deflected against the basin margins or close to the basin margin producing complex internal oscillatory-flow patterns that deformed the aggrading deposits, producing HCS and locally soft sediment-deformation (Pickering and Hiscott 1985; Tinterri et al., 2016; Cunha et al., 2017; Patacci et al., 2015). The association with thick to very thick ponded turbidity flow mudstone (F3b) strengthens the idea that this facies association records sedimentation in an environment where turbidity currents were reflected off of confining bathymetry.

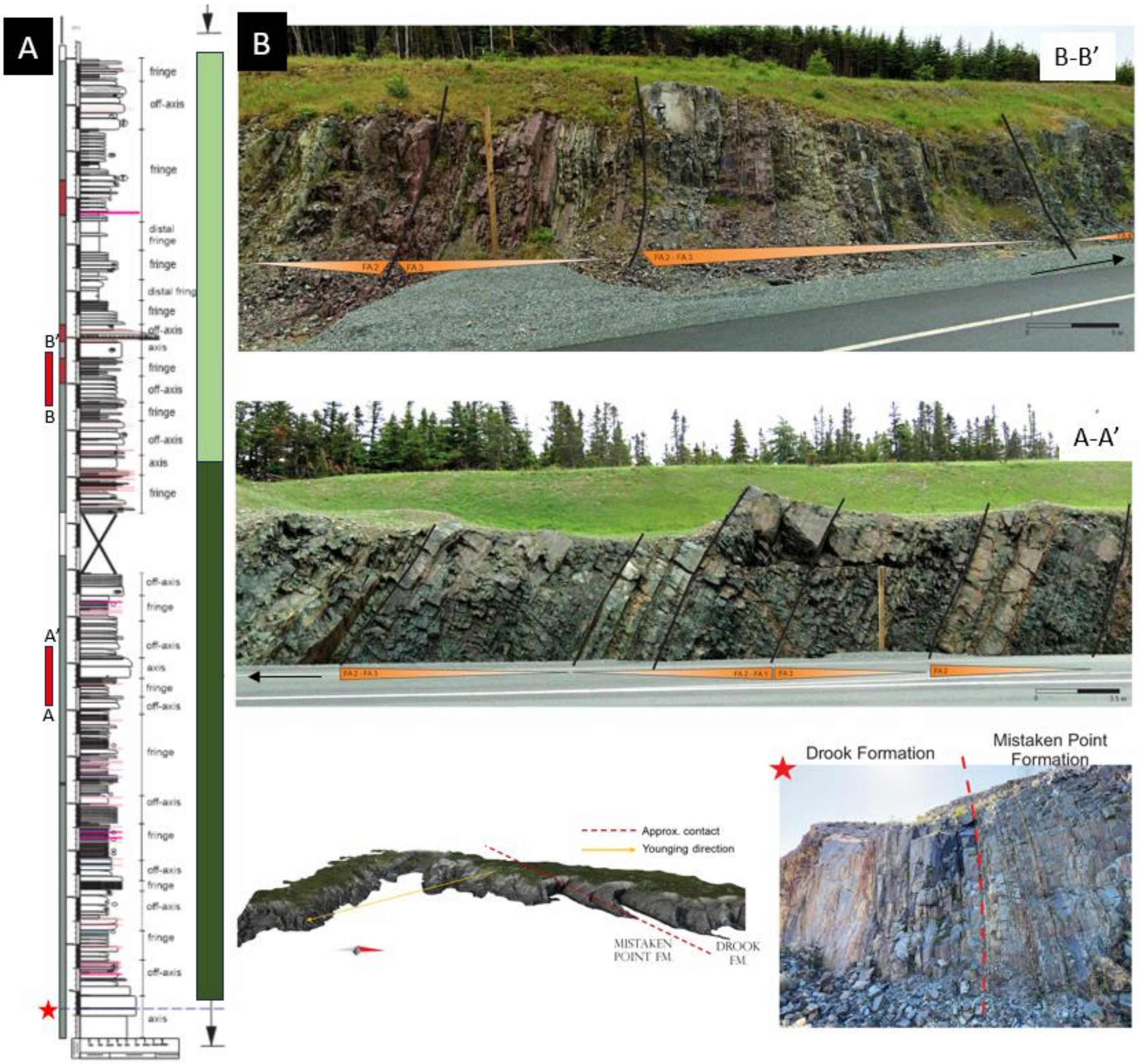

Figure 3.2 (A) 180 hundred meters stratigraphic column comprises of two lobe complexes (*dark green square* represent MPF1 and *light green square* represent MPF 2 or younger member) **(B)** Cross section of A-A' and B-B' shows dimension, changing in lobe staking pattern (thickening-thinning), and some observed lobe element from field observation. *Black arrow* indicates younging direction. *Red star* in the right below picture indicates the contact boundary between MPF and older Drook Formation. All attached pictures are located in Team Gushue Highway (contact approx. 47.547763, -52.765821).

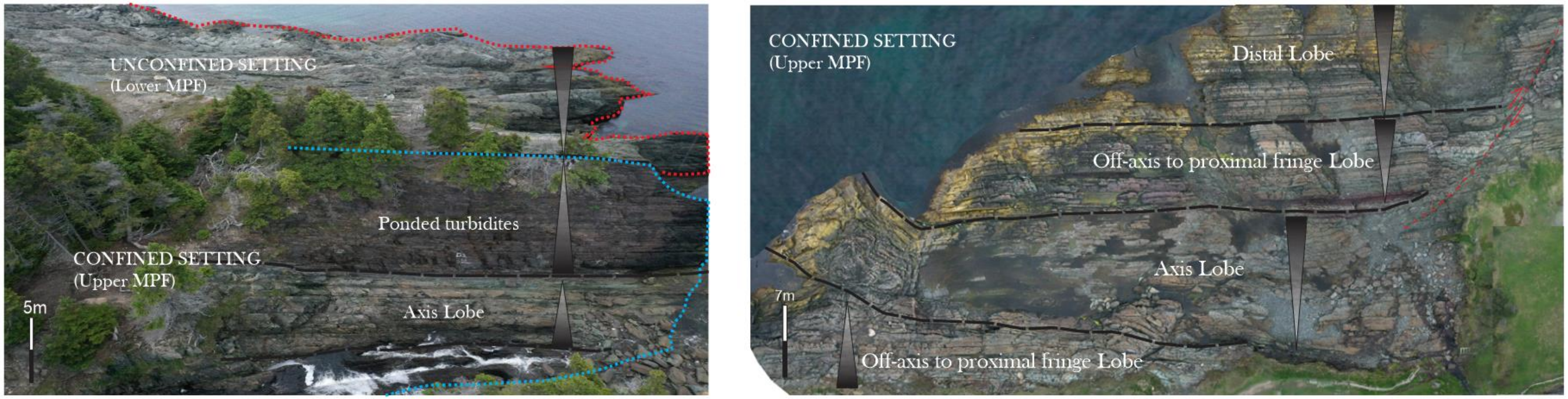

Figure 3 3 Conformity relationship between MPF 1and MPF 2 which distinguished by their degree of confinement (channelization in the fan system), exposed in Middle Cove section close to Torbay area (see Fig. 1.2 for area locations). **B)** Interpreted Upper MPF lobe elements or confined setting exposed in Section Middle Cove hundred meters east from A. Red arrow, respectively indicate paleoflow directions. Red solid lines represent fault near section; black dashed line represents sharp contact; red and blue dashed line represents upper and lower members. Black triangles represent upward coarsening and thickening trends.

CHAPTER IV STRATIGRAPHIC ORGANIZATION

Based on the stratal staking patterns of lobe facies associations, regional correlations, and detrital compositions, two broad dominant submarine fan paleoenvironments (Appendix A; C), termed MPF1 and MPF2, are recognized and shown in the correlation panel on Figure 4.1. The area covered by this correlation is 4 km (E to W) by 12 km (NE to SW) (*Figure 4.1*). Detailed sedimentologic and stratigraphic observations from existing and new outcrop sections show that the MPF evolves vertically from amalgamated medium- and thick-bedded axis lobe facies (FA1) alternating and interfingering with off-axis lobe facies (FA2) in MPF1; to less-amalgamated, more laterally continuous thinning-fining upward distal lobe successions (FA3) intercalated with confined turbidites (FA4) and rare pinching-out lobe axis elements in MPF2. This subdivision of the MPF closely resembles the two members of the MPF defined by King (1990), namely the lower Middle Cove Member (~MPF1) and the upper Hibbs Cove Members (~MPF2).

The MPF1 conformably overlies Drook Formation, and it is in sharp, conformable contact with the overlying argillaceous rocks of the MPF2. The lower boundary of MPF1 with the underlying Drook Formation is exposed along the Team Gushue Highway in St. John's (section GH2) and is defined by an abrupt change in bed thickness and lithology from thick massive coarse sandstone to thinner siltstone beds. The upper contact of the MPF2 with the Fermeuse Formation is not exposed. Near Middle Cove, northeast of St. John's and exposed along the coast, these units are in faulted contact. Nevertheless, in the same area (section MC2) in the upper part of the exposed MPF2 a thinning and fining succession of beds with interlaminated black shale may represent the base of a transitional contact between the MPF and overlying

Fermeuse Formation. Argillaceous rocks of the MPF2 are apparently conformably overlain by the grey sandstones and shales of the Trepassey Formation (St. John's group) in the northeastern part of the Donovans Industrial Park (King, 1990).

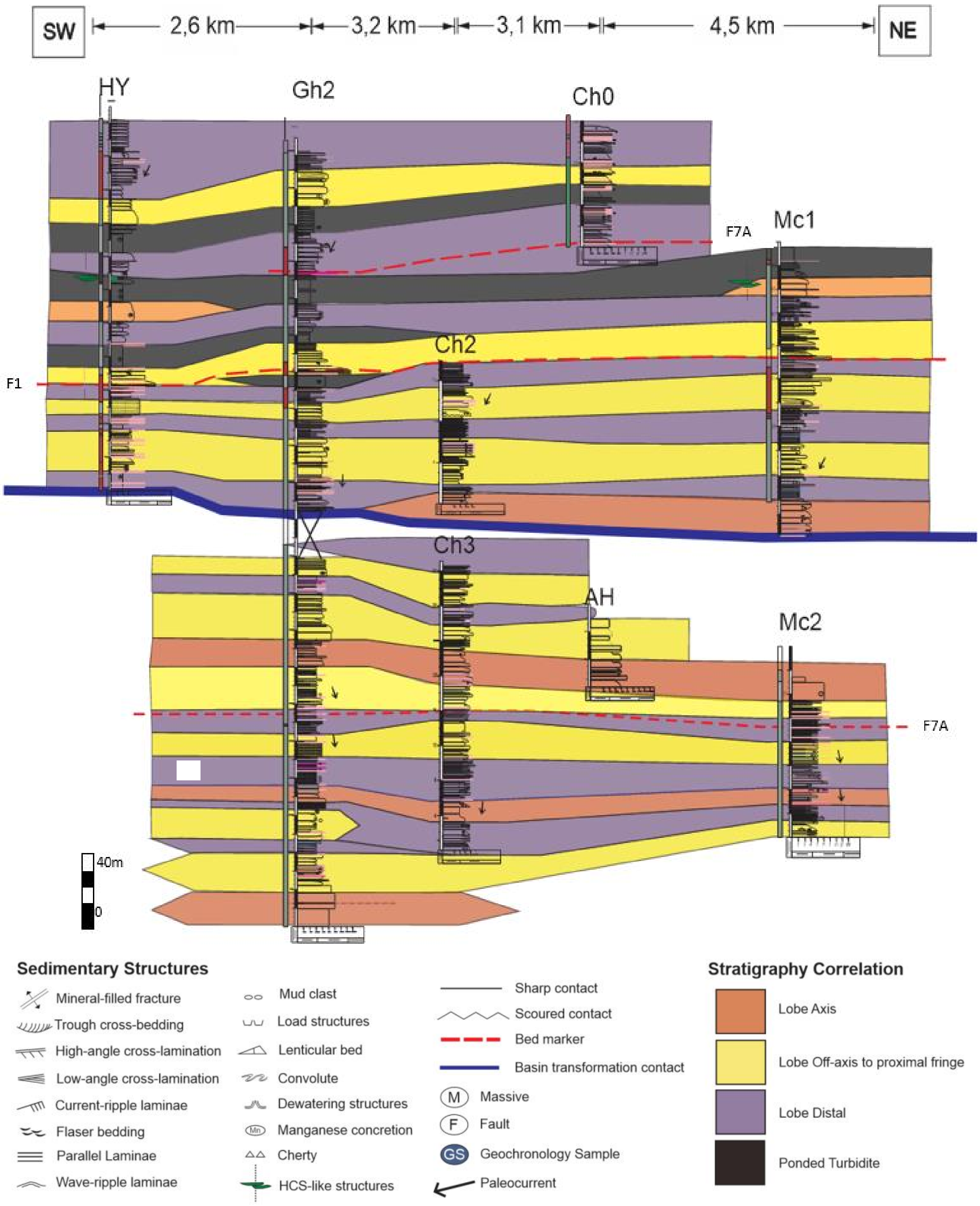

Figure 4.1 NE-SW, ±400m thick stratigraphic correlation of selected measured section in the northeastern Avalon Peninsula. The diagram shows a change of predominance facies association (lobe) from the older (MPF1) FA1-FA3 interlobes to the younger (MPF2) FA2-FA4 interlobes. The transition of MPF 1 and MPF 2 represent by blue line. Paleocurrent from current-ripple reading represent in black arrows is shown shifting from SE to SSW, respectively. Bed markers or marker horizons are lithography, including crystal ash tuff and conglomerate. They are shown in the red dashed line.

Nametag above each section refers to site names with numbers in dividing sub-section [HY, Hyundai; GH, Team Gushue Highway; CH, Trans-Canada Highway; MC, Middle Cove; AH, Airport Heights].

The following distinctive beds and surfaces were used for stratigraphic correlation across the study area:

- Two distinctive <5 mm-thick, well-preserved crystal ash beds within the tops of thinly bedded turbidites in distal lobe successions (FA3).
- The MPF1-MPF2 contact, generally between green medium-bedded turbidites of FA2 and interbedded green and red-purple unit of the thin bedded FA3 and FA4. Although there are along-strike differences in the thickness, grain size, and internal structures, the typical alternating red-purple beds at the base of MPF2 are distinctive and easily correlated
- A conglomerate bed in FA2 typically overlying a distinctive red distal lobe mudstone stratum (FA3) in MPF2.
- The very thick to thick bedded ponded mudstone beds (F3a) and HCS-like beds (FA4) in MPF2.

<u>*MPF Submarine fan evolution*</u>

MPF1 is 170 m thick and consists of 15-16 stacked lobes, mainly axis lobes (FA1, ~30%), off-axis to proximal fringe lobes (FA2, ~40%), and minor thin-bedded distal fringe lobes (FA3, ~30%). They are correlated over distances 11 km (*Figure 4.1*). The contact with MPF2 is sharp, marked by an abrupt change in bed thicknesses, from thin-bedded distal lobe strata to a thick-bedded sandstone with a slightly erosive base. MPF1 has a large distribution of tuff, including extremely angular (glass shard) and fragile-looking volcanic fragments (Fig. 2.7). The composition of MPF1's sandstone is shown to be generally quartz-lithic (sublitharenite) and feldspathic wacke. Reconstructed paleoflow directions measured from current ripples are generally to the south-southeast.

MPF2 is 245 m thick and is made up of 14-16 stacked lobe elements. All types of lobe elements (FA1-4) occur, including distal fringe lobe elements (FA3, ~35%), confined/ reflected turbidite lobe elements (FA4, ~30%), off-axis to the proximal fringe lobe elements (FA2, ~25%), and axis lobe elements (FA1, ~10%). MPF2 is correlated over distances 8.9 km (*Figure 4.1*). Evidence of fan confinement (channelization in the fan system) increases upward through MPF2, favouring ponding effects. Ponding processes are more evident in the upper portion of the MPF2, suggesting that fan confinement was much more pronounced during upper MPF2 sedimentation, which is also supported by the northward pinching out of these deposits shown in *Figure 4.1*. The sandstones of MPF2 are mostly feldspathic wacke. Some contain glass shards that have devitrified into chlorite minerals. Trace amounts of other heavy minerals, including zircon and rutile, have been observed. Unlike MPF1, the influx of fall ash tuff is not as abundant in MPF2. A rapid decline in volcaniclastic sediment and tuff facies occurs along the the MPF1 and MPF2 boundary which also denotes a divide between highly silicified rocks below (MPF1) and weakly to non-silicified rocks above (MPF2). Compared to MPF1, reconstructed paleoflow directions of MPF2 are generally to the south-southwest.

Changes in facies and detrital composition from MPF1 to MPF2 reflect variations in sediment supply and the degree of confinement (*Appendix D*) on the basin floor. The upward decrease in grain size and bed thickness and the increase in more distal fan elements upward, suggesting that the entire fan system was back-stepping over time *(Figure 4.2)*. This retrogressive trend of thinning and fining upward is attributed to progressive decrease in sediment supply from hinterlands to the basin, which also implies reduction in sediment concentration and flow energy.

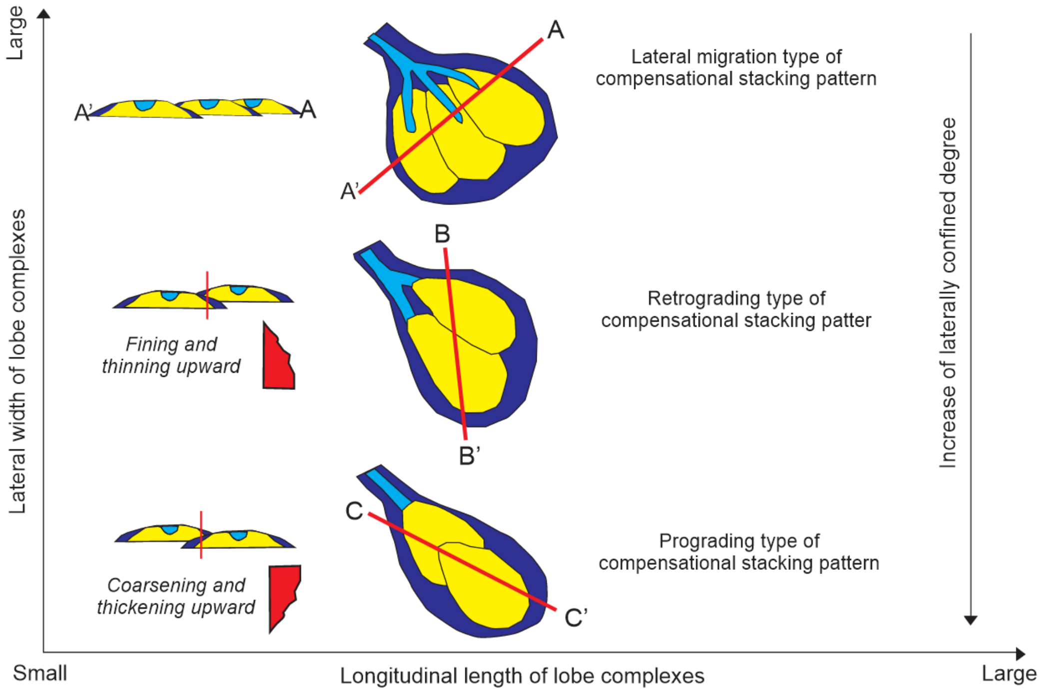

Figure 4.2 The graph demonstrates the compensational stacking pattern of lobe complexes, explaining the differences between lateral migration, retrograding, and prograding compensational staking pattern (modified from Zhang, 2016).

The development of barriers to turbidity currents on the basin floor are notable in MPF2. Two key characteristics, such as HCS-like structures and ponded turbidites, support the evidence of progressive confinement from less confined MPF1 to more confined MPF2 setting (*Appendix D*). This confinement is controlled by deformation that favour fault reactivation of the basin to generate boundaries to turbidity flows. The anomalous conglomerate beds in MPF2 may reflect reworking of talus shed from such local fault scarps.

Detrital composition from MPF1 to MPF2 generally reflects a change of provenance from volcaniclastic to terrigenous sources. In the transition of MPF2 towards the overlying Fermeuse Formation, black shale is more common. This supports an increase in supply from clay-dominated weathered terrigenous sources rather than clay from directly from coeval volcanic sources. Based on the detrital composition typical of MPF2's sandstone, including chlorite, iron oxide phases, and heavy minerals; basin oxygenation increased upward, possibly due to the influx of O_2 by dilute turbidity currents or a decrease in local sedimentation rates.

The preliminary results of paleoflow measurements show a slight shift in paleoflow from MPF1 to MPF2 (*Figure 4.1; Illustration 6.2*). Reconstructed paleoflow directions from current ripples are generally to the south but appear to shift from SSE in MPF1 to SSW in MPF2. This paleoflow shift along with overall upward reductions in sediment concentration, flow energy, and syn-sedimentary volcanism are a transformation in the orientation of feeder channels.

CHAPTER V - SEDIMENT PROVENANCE

Sandstone Petrography

Petrographic analysis facilitates in the interpretation of sedimentology and provenance based on detailed characterization of detrital mineral compositions and textural relationships of the detrital and diagenetic phases. For provenance analysis, petrography was carried out to 10 representative sandstone samples from both lower and upper members of the MPF, observed based on point counting (200-300) following the Gazzi-Dickinson method (Dickinson, W.R., 1970). The detrital framework components per sample were plotted on the tectonic discrimination diagram of Dickinson (1988) and QFL diagrams proposed by Ingersoll and Suczek (1979).

Ten samples of sandstone from MPF 1 and MPF 2 consist primarily of subrounded, moderately to well-sorted framework sand grains, with very fine (most common) to lower medium (rare) grain size. The primary components of the framework are plagioclase feldspar, volcanic and sedimentary lithic grains, polycrystalline and monocrystalline quartz, and rare metamorphic lithic fragments. As shown in Figure 5.2, volcanic grains are primarily of intermediate to felsic composition. As shown in Figure 5.2, rare metamorphic grains are present, including very low to low-grade pelitic grains. Five samples of MPF 1 plot on the dissected arc field in the QmFLt (Dickinson, 1988) diagram and on the magmatic arc field in the Qp-Lvm-Lsm diagram (Ingersoll and Suczek, 1979). The remaining five samples of MPF 2 plot between the basement uplift and dissected arc fields in the QmFLt diagram, and between the magmatic arc and rifted continental margin fields of the Qp-Lvm-Lsm diagram. Overall, the framework composition of the MPF 1 samples shows that they were sourced primarily from volcanic arc sources, with a minor contribution from low-grade metamorphic basement.

By contrast, the composition of the MPF 2 suggests derivation from exhumed plutonic and volcanic rocks, with insignificant additions from low-grade metamorphic rocks and sedimentary strata, respectively. This indicates a significant change in provenance between the sedimentation of the MPF 1 and MPF 2, from the erosion of an adjacent arc massif during MPF 1 sedimentation to exhumation of crystalline basement in sediment hinterlands during MPF 2 sedimentation.

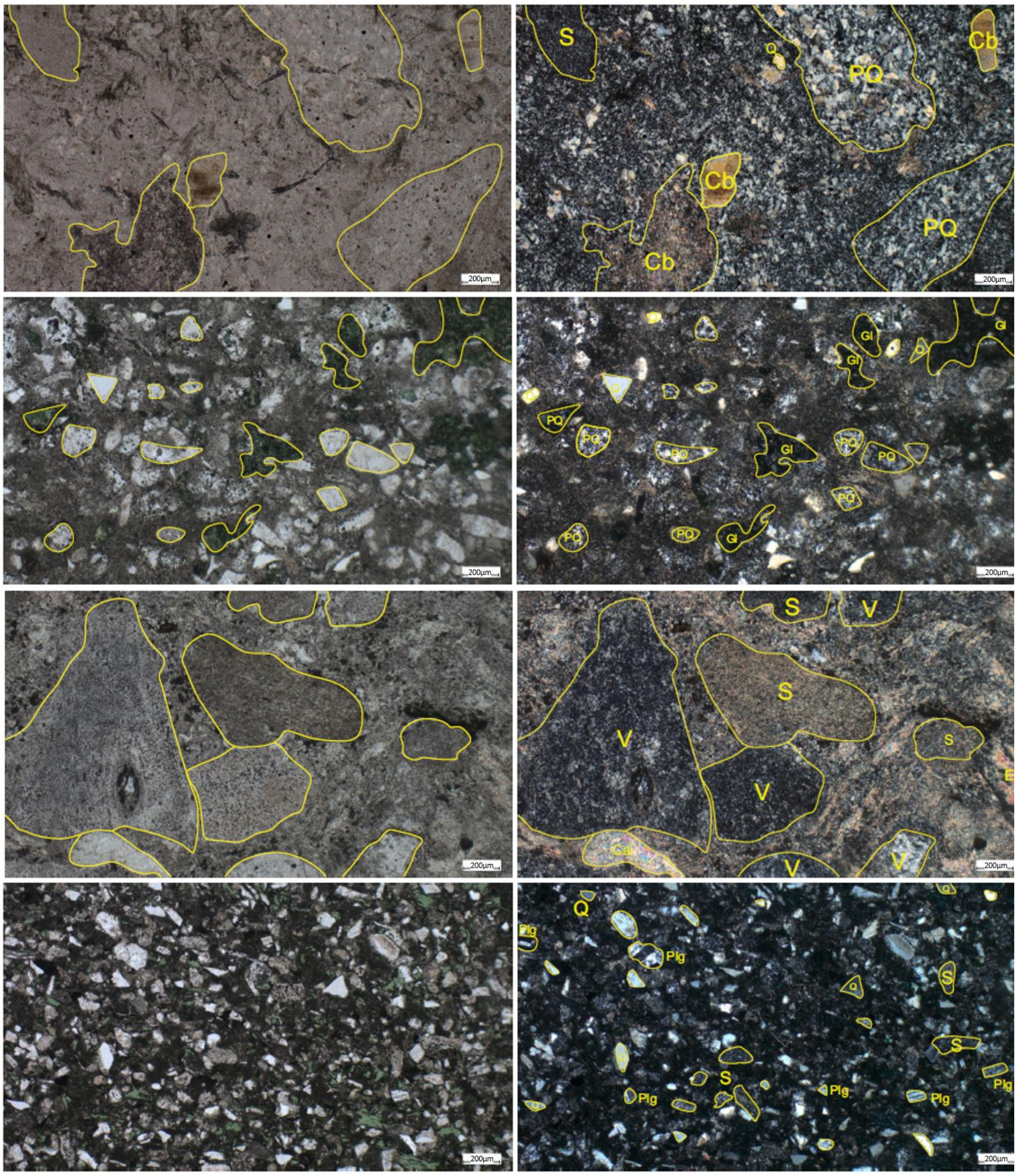

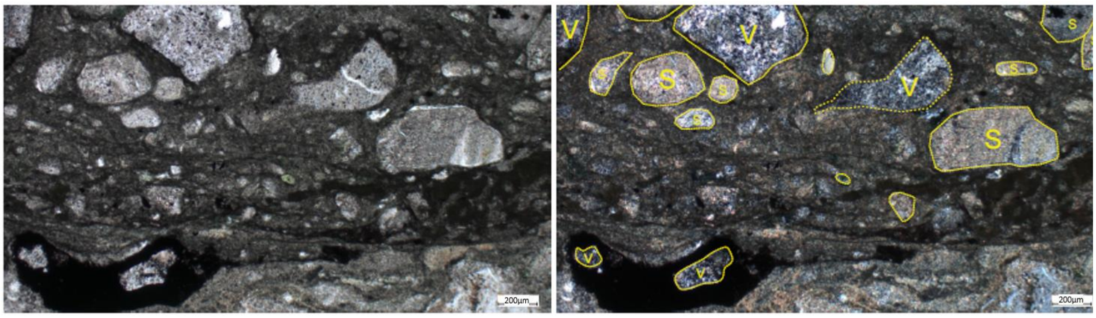

Figure 5.1 Selected thin section photomicrographs in PPL and XPL shows mineral composition. The methodology employed for this analysis is point-counting (Gazzi-Dickinson) (V-volcanic clast; S-sedimentary clast; PQ-polycrystalline quartz; Gl-gluconite; Q-monocrystalline quartz; Cb-carbonate; Plg-plagioclase; Fd-feldspar; Cal-calcite; Ep-Epidote m-matrix)

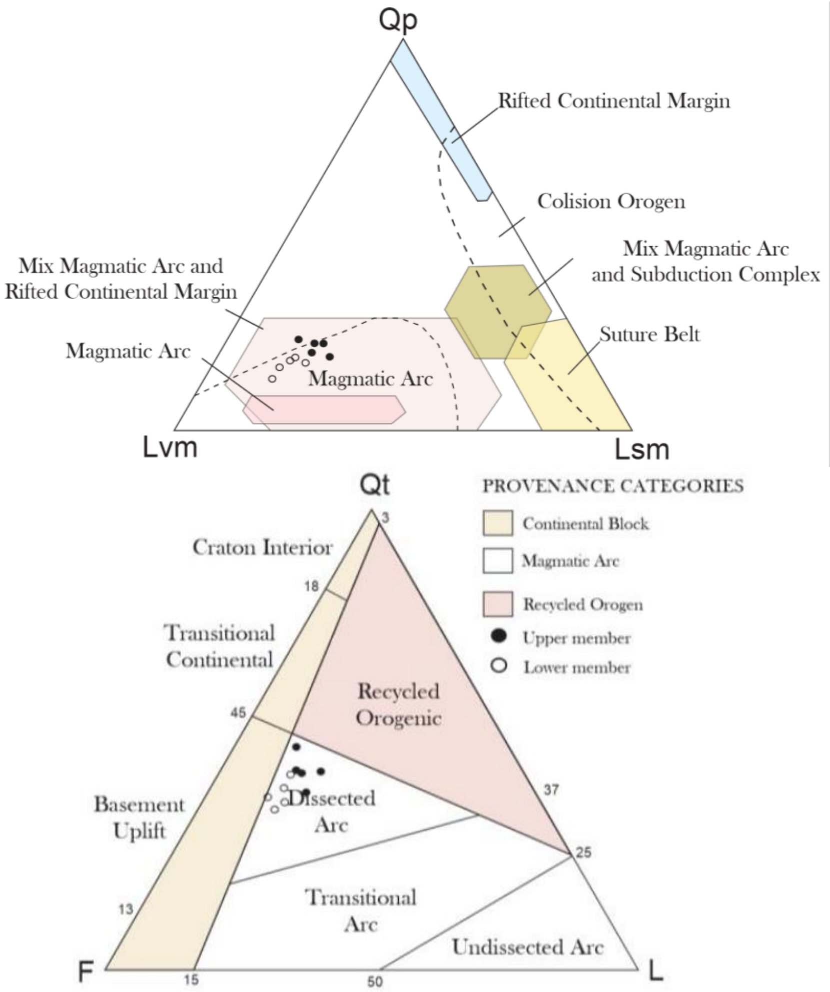

Figure 5.2 The QFL and QpLvmLsm ternary plots from selected ten samples. Five samples of MPF 1 plot on the dissected arc field in the QFL (Dickinson, 1988) diagram and on the magmatic arc field in the Qp-Lvm-Lsm diagram (Ingersoll and Suczek, 1979). The remaining five samples of MPF 2 plot between the basement uplift and dissected arc fields in the QmFLt diagram, and between the magmatic arc and rifted continental margin fields of the Qp-Lvm-Lsm diagram.

Intersample Detrital Zircon Comparison

This study focuses on the St. John's sections thus far, however, in this section regional provenance data is integrated from the Mistaken Point Ecological Reserve and Spaniard's Bay area. The strata from which rock samples were collected at Spaniard's Bay and Mistaken Point correlate to MPF1 and MPF2 in St. John's, based on the original lithostratigraphic definitions of the Middle Cove and Hibbs Cove Members, which here are correlative to the MPF1 and MPF2 subdivision in St. John’s. These subdivisions serve as criteria for correlation from St. John's to Spaniard's Bay and Mistaken Point. The lower member (=MPF1) is characterized everywhere by generally grey, sand-rich fan axis facies with abundant tuffaceous beds, while the upper member (=MPF2) contains red-purple mudstone with crystal ash tuff and dominated by distal fan facies with a and a relative paucity of tuff compared to the lower member.

These regional provenance data are used to more accurately understand the provenance changes associated with regional basin transformation observed across the Avalon Peninsula during MPF sedimentation (e.g., Ichaso et al., 2007; this thesis). Six samples weighing between 1-2 kgs were collected, processed for detrital zircons, and analysed using U-Pb geochronology (Appendix G). Data reduction and U-Pb age calculations were carried out using the VizualAge data reduction scheme developed for Iolite (Paton et al., 2011; Petrus & Kamber, 2012). Out of these, three samples contained a sufficient number of zircons (>150 grains), one sample had a very limited number of zircons (<20 grains), and the remaining two samples did not contain any zircon grains.

The KDE plots illustrating detrital zircon ages from the MPF 2 samples (HC-ER and HC-SB) exhibit comparable age peak distributions and abundances of Precambrian ages, contrasting with the age peaks and abundances of Precambrian ages observed in the MPF 1 sample (MC-SB) (Fig. 5.3). The results indicate a minimal level of distinction in the detrital zircon age distributions among the MPF 2 specimens, while showing a notable variation between the MPF 1 and MPF 2 samples. The cross-correlation coefficient matrix was employed to measure the levels of dissimilarity (Saylor and Sundell, 2016; 2017) (Table 5.1). The MPF 2 samples HC-ER and HC-SB exhibited cross-correlation coefficient values exceeding 0.90, indicating a high degree of similarity in their detrital origins and identical detrital zircon distribution. Conversely, the low cross-correlation coefficient values derived between the MPF 1 sample and the MPF 2 samples indicate that despite a considerable level of resemblance in the origins, distinct variations in the detrital zircon distribution are present. Given the identical detrital zircon age distribution of the MPF 2 samples, they are grouped into a single representative sample, which will be treated as such from here onwards.

Table 5.1 Cross-correlation Coefficient Matrix

	HC-ER	HC-SB	MC-ER
HC-ER	1	0.90	0.32
HC-SB	0.90	1	0.24
MC-ER	0.32	0.24	1

Detrital Zircon Geochronology

Detrital zircon ages from the MPF1 at Spaniard's Bay (MC-SB) define a unimodal peak at ca. 606 Ma consisting mostly of Ediacaran (66%) and Cryogenian (6%) zircons, a Tonian peak at ca. 752 Ma (7%), Mesoproterozoic peak at ca. 1550 Ma (7%), and a Paleoproterozoic peak at ca. 2050 Ma (14%; Fig. 5.3). A combined sample from the overlying MPF2 in Spaniard's Bay and Mistaken Point depicts a polymodal distribution with peaks at ca. 607 and 560 Ma comprising 80% Ediacaran and Cryogenian ages spanning from 542 to 720 Ma. Subordinate peaks include 3.5% Tonian ages with a peak at ca. 766 Ma, 16.5% Mesoproterozoic and Paleoproterozoic with peak ages ca. 1230 Ma, and between 1400 to 1700 Ma (Fig. 5.3).

Samples from both MPF1 and MPF2 yield Maximum Depositional Ages (MDA) estimates that vary by method. Samples have *Youngest Grain Cluster of Dickinson and Gehrels* (2003) (YGC2σ) are 7 Ma younger than calculated *Maximum Likelihood Age* (MLA). By enlarging the sample size and employing method YGC2σ, the tails of the normal distribution are extended, leading to a younger distribution. For the best estimate and approach, MLA was chosen for this study (*refer to Methodology ch*). Maximum depositional ages calculated for the MPF1 and MPF2 facies yield 567.2 ± 10.1 Ma and 560.33 ± 3.72 Ma, respectively (Fig. 5.4). The results of the MLA method are best visualised on radial plots (Vermeesch, 2021) (Fig. 5.4).

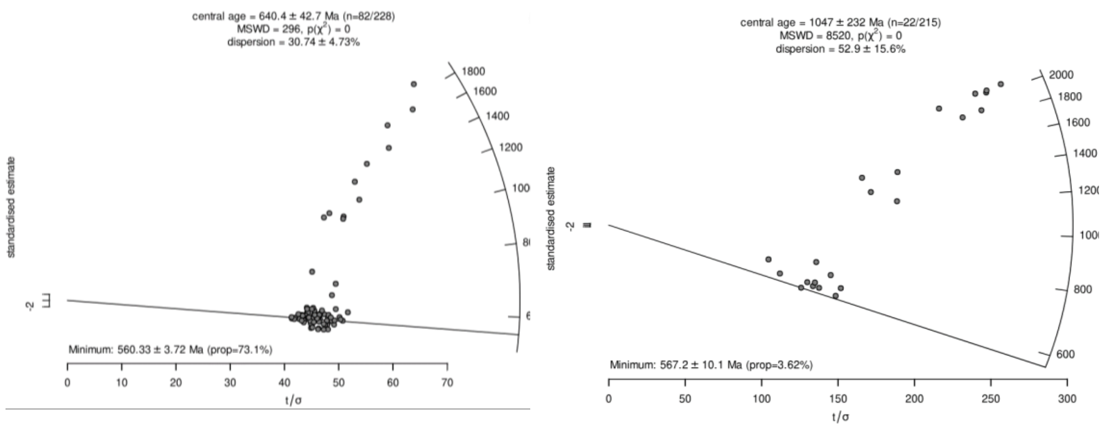

Figure 5.3 The maximum depositional ages determined for the MPF1 (left) and MPF2 (right) facies are 567.2 ± 10.1 Ma and 560.33 ± 3.72 Ma, respectively. MLA was selected as the preferred method for this study to obtain the most accurate estimate and approach. The findings obtained through the MLA technique are most effectively presented using radial plots as suggested by Vermeesch (2021).

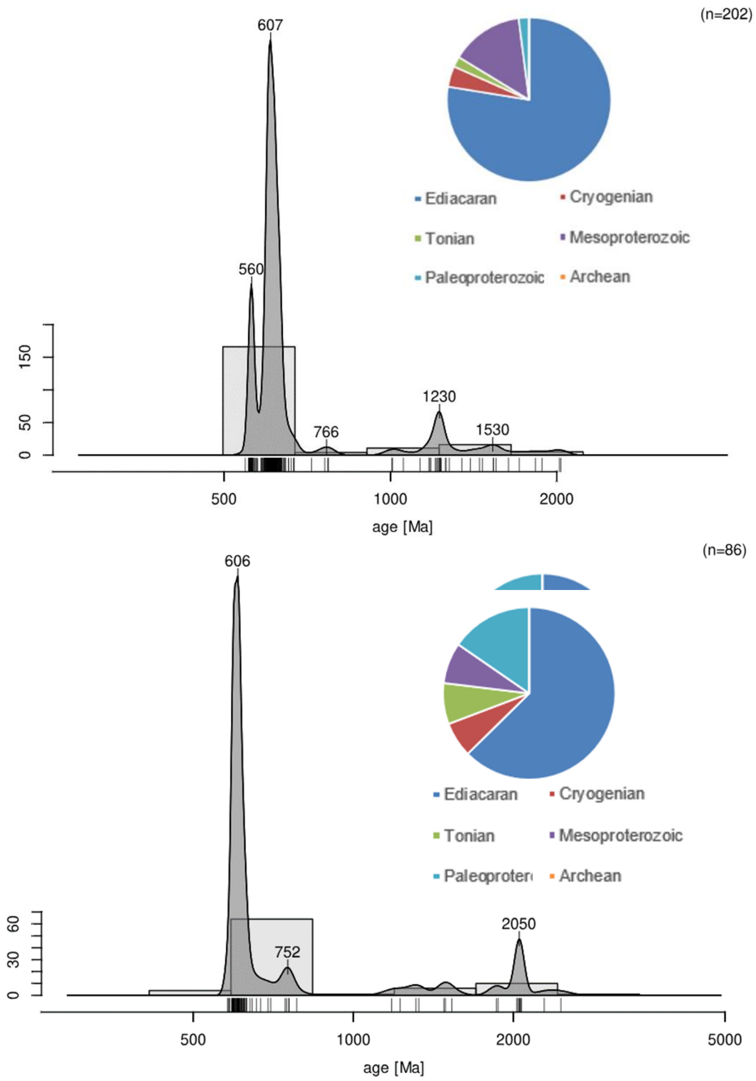

Figure 5.4 The detrital zircon geochronology analysis conducted on the MPF1 at Spaniard's Bay (MC-SB) reveals a unimodal peak at approximately 606 Ma, predominantly composed of Ediacaran zircons (66%) and Cryogenian zircons (6%). Additionally, there is a Tonian peak at around 752 Ma (7%), a Mesoproterozoic peak at approximately 1550 Ma (7%), and a Paleoproterozoic peak at about 2050 Ma (14%). On the other hand, the combined sample from the overlying MPF2 in Spaniard's Bay and Mistaken Point displays a polymodal distribution with peaks at approximately 607 and 560 Ma, with 80% of the zircons falling within the Ediacaran and Cryogenian age range spanning from 542 to 720 Ma. There are also subordinate peaks, including 3.5% Tonian ages with a peak at around 766 Ma, and 16.5% Mesoproterozoic and Paleoproterozoic ages with peak ages ranging from approximately 1230 to 1400 to 1700 Ma.

CHAPTER VI - DISCUSSION

Provenance Interpretation

The petrography and detrital zircon ages of the MPF 1 and MPF 2 facies indicate a combination of sediment sources, including exposed Ediacaran to Tonian intermediate plutonic, intermediate to felsic volcanic, sedimentary, and low to medium-grade metamorphic rocks. The detrital zircon ages found in the MPF 1 and MPF 2 samples, which belong to the Ediacaran (635-538.8 Ma) and Cryogenian (720-635 Ma) periods, respectively, exhibit similarities to the ages obtained from granitic and volcanic rocks in the exposed igneous basement (Skipton et al., 2013; Mills et al., 2020) and bimodal volcanic cover sequences that are exposed throughout the Avalon Peninsula, specifically within the Harbour Main Group during the main arc phase around 620 Ma (King, 1990).

Tonian detrital zircon ages exhibit a paucity of exposed potential sources within the Avalon Zone. The Burin Group, composed of mafic-ultramafic rocks, and the rhyolitic Hawke Hills tuff, represent the remains of an early Avalonia volcanic arc and the initial phase of composite West Avalonia magmatism, are among the limited sources (Israel, 1998; Murphy et al., 2008). In the studied area, Tonian peaks between 765-750 Ma suggests a potential derivation from sources related to the immature arc phase of the Burin Group, and detrital ages from 739-727 Ma suggests potential derivation from rocks of the ‘first arc phase’ of composite West Avalonia as interpreted by Beranek et al. (2023). The presence of these Tonian peaks in the MPF therefore indicates the exposure of earlier arc basement in sediment hinterlands.

Sourcing from low-to-medium grade metamorphic rocks was notable in samples from MPF 2 based on the presence of metasedimentary grains. West Avalonian terranes or basement complexes are potential source candidates including the Gamble Brook formation and the Mount Thom in the Cobequid Highlands (White et al., 2022) and Hammondvale metamorphic suite in the Caledonia terrane that is associated with subduction (White et al., 2001). The reported MDA results by White et al. (2001) for the metamorphic rocks in the Cobequid Highlands are between ca. 776-1000 Ma and estimated the metamorphism of Mount Thom Formation between 800-770 Ma. However, these ages are not found in zircons of the MPF samples, indicating that Cobequid Highland-type sources were unlikely. On the other hand, 605-618 Ma metamorphism corresponds to the Hammondville metamorphic suite, which also contains inherited zircons with Cryogenian, Meso- and Paleoproterozoic ages (Satkoski et al., 2010; White et al., 2001). Such peaks occur in both samples, and it is feasible to explain them by sourcing of rocks of or like the Hammondvale metamorphic suite, since the exhumation and erosion of the Hammondville accretionary subduction complex was underway by ca. 550 Ma, and perhaps earlier (White et al., 2001).

MPF 1 exhibits a broad spectrum of pre-Tonian zircon grain ages ranging from 1677 to 2457 Ma, whereas MPF 2 comprises a narrower range of pre-Tonian detrital zircon ages between 1239 and 1690 Ma. The presence of ages from the Paleoproterozoic suggests that these may have been recycled detrital zircons from Cyrogenian – early Ediacaran cover sequences (van Staal et al., 2021) or from unexposed Avalonian sub-arc metamorphic basement rocks with Baltican affinity (Beranek et al., 2023).

The provenance changes between the MPF 1 and the MPF 2 are interpreted to reflect the reconfiguration of hinterland sources. Exhumed Ediacaran-Tonian plutonic rocks and contemporaneous volcanic and sedimentary cover sequences, minor Cryogenian to low-grade metamorphic rocks with inherited Meso to- Paleoproterozoic zircons were replaced by dominantly Ediacaran to Cryogenian volcanic cover sequences and minor

Tonian to older low to medium-grade metamorphic basement with Mesoproterozoic zircons. These changes in provenance may indicate hinterland uplift by contemporaneous deformation of a tectonically active fore-arc or back-arc area, manifested in the basin by changes in routing, lobe backstepping, and progressive fan confinement from MPF 1 to MPF 2. Therefore, we infer that these stratigraphic changes were caused by changes in the tectonic regime of sedimentation, from arc-adjacent (fore-arc or back-arc) sedimentation to a foreland basin (van Staal et al., 2021; Serna Ortiz and Lowe, 2024).

Depositional System

In the study area (St. John's, Northeastern Avalon Peninsula) the MPF exposes thicker and more diverse units compared to the equivalent strata exposed near Spaniard's Bay and Mistaken Point, indicating a locally unique flow evolution and paleo-depositional system. The current interpretation of the MPF is limited to a portion of the submarine fan lobe system with evidence of intense volcanism, due to several reasons:

- Turbidite and suspension-product facies are widely observed in the stratigraphy, including the dominance of silt to fine sand in moderately thin to medium beds.
- The absence of shallow-water or tidal characteristics, slump, and debris deposits. The existence of HCS-like structures in MPF 2 indicates the presence of an oscillatory-flow pattern near or at the basin margin, suggesting the reflection of turbidity currents with confining bathymetry (Mulder et al., 2009; Tinterri, 2022).
- The abundance of lobate-tabular features and the scarcity of channel or erosional features.

- The observed thickening-thinning stacking patterns and the predominance of fining upward cycles.

The exposures of the MPF near St. John's are interpreted to represent only a small part of a larger submarine fan system. Changes in facies and detrital composition observed between MPF1 and MPF2 from Spaniard's Bay to Mistaken Point suggest the entire fan system was back-stepping over time, with a coinciding reduction in sediment concentration, flow energy, and syn-sedimentary volcanism (see Chapter IV. Stratigraphic Organization). The upward decrease in sandstone-rich turbidites and volcanogenic and ash beds supports the overall reduction of the volcanic-arc influences during MPF deposition. In addition, ponded and HCS-like facies in MPF 2 (F2E, F3B, FA4) suggests a progressively confined basin architecture implying that the MPF 2 was influenced by bathymetric barriers to flow, potentially associated with the emergence of the Harbour Main volcanic ridge as suggested by Ichaso et al. (2007).

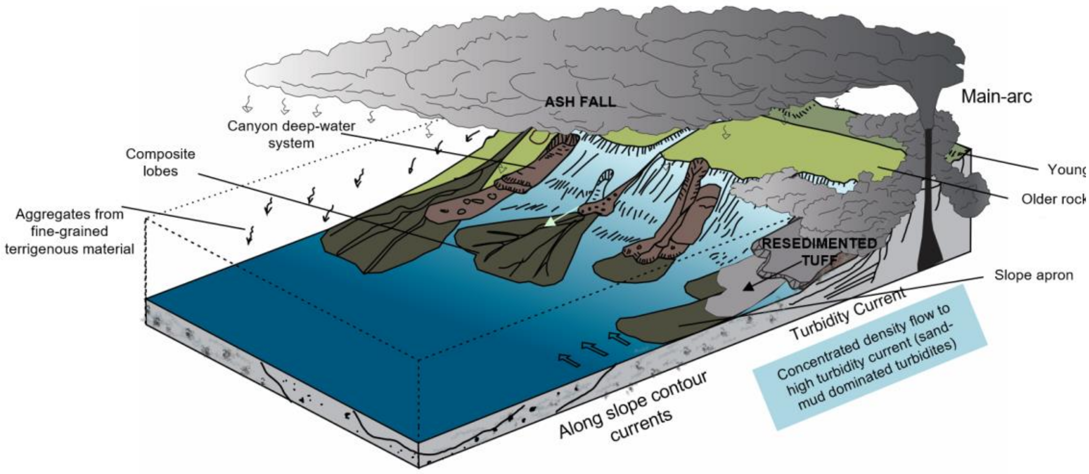

Illustration 6.1 Conceptual Model of the MPF Depositional System. MPF represents an active period of volcanic activity concurrent with submarine fan sedimentation, with an overall reduction of flow energy and degree of volcanic supply through time. Stratigraphic evidence suggests MPF strata were deposited by concentrated density flows to low-energy turbidity currents, which are represented by facies conglomerate, sandstone, and mudstone. Two different mechanisms of volcanic ash deposit: (1) hemipelagic settling by wind-derived and suspension (2) resedimented and transported downslope with turbidity current, resulted in three sub facies of tuff. Along slope process (bottom current deposit) may be the influence of heterolithic facies deposition.

Basin Reconstruction

Avalonia represents the most extensive accreted crustal block within the Appalachian Caledonian orogen, documenting a Neoproterozoic tectonomagmatic evolution as a peri-Gondwanan composite arc terrane. During the deposition of the Conception Group, Williams and King (1979) concluded that the eastern portion of the Avalon Terrane was closely located to volcanic centers. This inference was made, in part, due to its basal contact which onlaps arc volcanic rocks of the Harbour Main Group (King, 1990). Furthermore, thorough regional mapping enabled previous researchers to correlate lithostratigraphic units across the Avalon Peninsula (King, 1979; 1990). This suggests that the entire region underwent a relatively similar sedimentary history. Therefore, with this study, we can compare paleocurrent patterns throughout the area extent of MPF to reconstruct the geometry of the depositional basin and its evolution.

These new and existing paleoenvironmental interpretations of the MPF suggest that ponded turbidites were widespread near St John's and Spaniard's Bay (Ichaso et al., 2007), but that southeasterly advancing debris flows were more common at Mistaken Point (Wood et al., 2003), and hemipelagic sedimentation and southeasterly facing turbidity currents predominated at the Catalina Dome (Mason et al., 2012). Another distinction is the absence of red beds at the Catalina Dome, which are prominent in the MPF 2 in St. John's and Conception Bay. This suggests that the fan paleoenvironment of the northeastern Avalon Peninsula (St. John's area) had more similarities to those preserved in the Conception Bay area than the paleoenvironments of the Mistaken Point or the Catalina Dome sections.

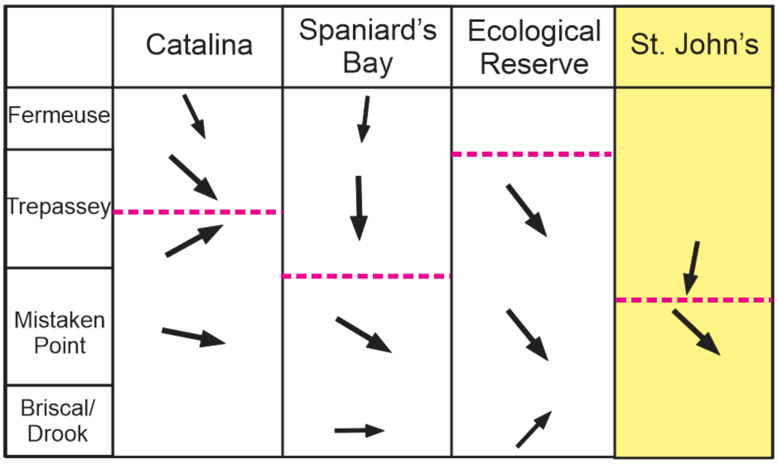

Illustration 6.2 The comparison of basin transition based on paleocurrent measurements in four distinct study areas within the Avalon and Bonavista Peninsula. The pink dashed lines indicate a gradual shift of basin transformation. The transition firstly occurred in the St John's area approximately halfway through the MPF's succession., then followed in the Spaniards Bay (Conception Bay, 42 kms western St John's) within the upper MPF formation. It then occurred in the Catalina Dome, Bonavista Peninsula (nearly 100 kms northwest St. John's) within the Trapasssey Formation. Finally, it observed between the Trepassey and Fermeuse formations in the Ecological Reserve MPF in the southeastern Avalon Peninsula

A change in paleocurrent directions from east to south is recorded across the Avalon Peninsula, including in the current study area of St. John's, Conception Bay (Ichaso et al., 2007), Mistaken Point (Wood et al., 2003) and the Catalina Dome (Mason et al., 2012). However, assuming that lithological boundaries are roughly synchronous, this change in flow direction is diachronous across the Avalon Peninsula. For example, in the Mistaken Point Ecological Reserve area, the transition from east-to-south directed paleocurrents occurs at the boundary between the Trepassey and Fermeuse formations (Wood et al., 2003). In the Catalina Dome, this transition occurs within the Trepassey formation (Mason et al., 2012), while in the Conception Bay, it occurs within the upper MPF formation (Ichaso et al., 2007). In the St John's sections, the paleocurrent directions change from southeast to south-southwest at approximately halfway through the MPF's succession. This is at a lower boundary compared to the Catalina Dome, but is very close to the same boundary in the western Conception Bay, indicating that both may have been in proximity to an uplift caused by compressional or strike-slip faulting

(King, 1990; Calon 2001; Ichaso et al., 2007). The differences in relative timing in this shift in paleoflow (Appendix E) may therefore have been attributed to its location farther northeast, nearer uplifted hinterlands.

The exact timing of basin transformation is uncertain; however, the evidence suggests that it was caused by a change in tectonic regime leading to the reorganization of the basin's topography. New stratigraphic and provenance data from this research has addressed some of the previous limitations in understanding the changes in basin reconfiguration. These observations support a two-phase tectonic model proposed by Murphy et al. (1999) and Nance et al. (2002), which suggests an initial deposition in an active, ash-generating, back-arc setting (Myrow, 1995; Skipton et al., 2013) and subduction zone, followed by a gradual transition to strike-slip or compressional regime. Recent stratigraphic and provenance work suggests that sedimentation in the overlying St. John's and Signal Hill groups occurred in a foreland basin (Serna Ortiz and Lowe, 2024).

The statistical similarity in the detrital zircon distribution of the MPF 1 samples from Spaniard's Bay and Mistaken Point suggest that at least these parts of this MPF 1 system were linked to the same source area, defined mostly by exhumed Ediacaran-Tonian plutonic rocks and contemporaneous volcanic and sedimentary cover sequences. These results support the initial interpretations of continuous southeastward MPF 1 progradation mainly sourced by exhumed Avalonian arcs (King, 1990). The conformable transition between the MPF 1 and the MPF 2 suggests a gradual upward change of basin setting. A QFL ternary plot from 10 point-counted samples inferred a trend from dissected arc toward basement uplift, where the QpLvmLsm showed a trend from magmatic arc to mix magmatic arc to rifted continental margin. Based on the provenance and stratigraphic evidence, this suggests synchronous hinterland uplift, coinciding with tectonically driven basin confinement.

The MDA results of the MPF 1 and MPF 2 facies yielded 567 ± 10.3 Ma and 560 ± 3.72 Ma (Fig. 5.4), suggesting that these hinterland changes, uplift, lobe retrogradation *(Figure 4.2)*, and basin confinement occurred at circa. 565 Ma.

The results of upper MPF (560 ± 3.72 Ma) presented in this study appear to show a younger age compared to the established ages reported by Matthews et al. (2021) at 564.13 ± 0.65 Ma. The adoption of the MLA technique is preferable as it does not skew the results towards a younger age, yet it still yields a younger age than anticipated. There is a potential risk regarding Pb-loss which could result in a younger age of the grains; nevertheless, this issue has been addressed through the implementation of chemical abrasion. This procedure likely resolved the issue by removing any parts of the grains affected by radiation damage where Pb-loss occurred. Therefore, the analysis conducted, and the subsequent outcome are considered accurate based on the procedures employed.

The observed difference in ages of the onset of Fermeuse Formation sedimentation from southern Avalon Peninsula (ca. 564 Ma; Matthews et al., 2021) and MPF2 strata along the eastern shore of Conception Bay (ca. 560 Ma) could be explained by sedimentation in sub-basins separated by the Harbour Main High (Ichaso et al., 2007). Notably, also the thickness of the upper MPF (MPF2, equivalent to the Hibbs Cove Member) increases significantly from the MPF Ecological Reserve to the eastern shore of Conception Bay (St John’s area), from 20 m to over 200 m. Along with the noted diachronism, this major isopach discrepancy supports the existence of separate sub-basins separated by the Harbour Main High as suggested by Ichaso et al. (2007), each with unique successions and temporally-distinct onset of Fermeuse Formation sedimentation, which occurred later in the west Conception sub-basin (*sensu* Ichaso et al., 2007) than elsewhere in the main Conception Basin.

CHAPTER VII - CONCLUSION

This research details the environmental and morphodynamic response of the MPF submarine fan system to basin reconfiguration, using facies and paleoflow analyses, and provides regional paleogeographic reconstructions of this reconfiguration and links to hinterland and basin margin deformation constrained by provenance data and maximum age relationships.

The Mistaken Point Formation (MPF) is a ~400m thick, late Neoproterozoic siliciclastic-volcaniclastic unit that crops out in the Avalon Zone of Newfoundland. The MPF is located at the top of a thick sequence of volcaniclastic submarine fan layers within the Conception Group, which were deposited during the transition from a back-arc basin to a foreland basin. Hence, the MPF strata provides valuable understanding regarding the impact of basin transformation on crucial aspects of the local sedimentary environment. Detailed stratigraphic, petrographic, and facies analysis were integrated, supporting a submarine fan depositional system with four lobes that stack to form two lobe complexes: MPF1 (lower) and MPF2 (upper). Generally, it is concluded that:

1. The succession throughout the entire area accumulated in a submarine fan system, particularly deepwater basin that shallowed upward from a flat basin floor to a basin-bounding slope, with ash beds supplied from an adjacent volcanic arc. Stratal stacking patterns indicate a lobe abandonment process characterized by "back stepping", resulting in a gradual decrease in sediment concentrations, flow energy, and syn-sedimentary volcanism. Facies analysis reveals the presence of ponded turbidites and HCS-like stratification, reflecting the progressive confinement of the basin over time.

2. The reconstructed paleoflow directions (Appendix E) derived from current ripples predominantly shift from SE to S-SW is similar to what is seen in strata across the Avalon Peninsula, and supports a two-phase tectonic history hypothesized for the Late Neoproterozoic (Ediacaran) rocks of the Avalon Zone. This shift in paleoflow, coupled with the overall decrease in stratal stacking patterns holds great significance as it signifies a transformation in the orientations of sediment input. The change in flow directions was diachronous across sections of the MPF, occurring much earlier in the northern sections near St. John's and Spaniard's Bay, suggesting the influence of a southward-propagating uplift.

3. A ternary plot was constructed using QFL data from 10 point-counting petrography samples, reveals a shift from a dissected arc towards basement uplift. In addition, the QpLvmLsm ternary plot displayed a transition from a magmatic arc to a mixed magmatic arc and a rifted continental margin. This outcome highlights the changes in mineral composition observed in samples from both members which hold substantial importance in relation to the shifts in provenance.

4. Detrital zircons within the MPF are dominated by ages corresponding to the main Avalonian Arc (ca. 620-630 Ma). Sediment sources changed upward within the MPF, characterized by increasing contributions of Mesoproterozoic zircons (ca. 1.2 Ga), a decrease in Tonian sources (730-780 Ma) and the loss of Paleoproterozoic grains (~2.1 Ga).

5. The detrital zircon distribution of the MPF 1 samples from Spaniard's Bay and Mistaken Point indicates a statistical similarity, implying a link between these

regions within the MPF 1 system, which attributed to the presence of exhumed Ediacaran-Tonian plutonic rocks, as well as contemporaneous volcanic and sedimentary cover sequences in the defined source area. These findings align with the initial hypothesis of continuous southeastward MPF 1 progradation, which was predominantly sourced by exhumed Avalonian arcs. The provenance and stratigraphic evidence further suggest synchronous hinterland uplift, coinciding with tectonically driven basin confinement.

6. Maximum depositional age estimates and sediment provenance for the MPF1 and MPF2 facies yield 567.2 ± 10.1 Ma and 560.33 ± 3.72 Ma, respectively suggesting that these hinterland changes, uplift, lobe retrogradation, and basin confinement occurred at circa. 565 Ma.

Future Research

Despite the extensive approaches that have been implemented in this study, there remains room for further expansion and research, particularly in the Atlantic Canada. The intricate nature of structural complexity in St John's MPF presents opportunities for more detailed structural measurements. This approach is expected to address issues related to tectonic complexity in the research area which aim to tackle potential stratigraphic offsets. Secondly, the study has pinpointed a stratigraphic boundary between MPF and underlying Drook formation, with one evidence located along the Gushue highway. However, the boundary to the upper Fermeuse formation remains ambiguous. Therefore, it is worthwhile to carry out comprehensive fieldwork at inaccessible locations that have not been incorporated into the study. Thirdly, despite the scarcity of crossbed, ripple, or sole structures in deepwater deposits, a comprehensive examination of regional paleoflow can be optimized to enhance basin configuration analysis on a more intricate scale. Finally, the determination of the maximum depositional age can be carried out through the examination of tuffaceous or coarser wacke sandstones from the St John's area. This approach is expected to enhance the accuracy of geochronology and provenance studies and provide a more comprehensive understanding of the tectonics and paleogeography of this tectonically and ecologically significant stratal succession.

References

Allen, J. (1973). A Classification of Climbing-Ripple Cross-Lamination. *Geological Society of London, Journal, V. 129*, 537–541.

Allen, J. (1984). Parallel lamination developed from upper-stage plane beds: a model based on the larger coherent structures of the turbulent boundary layer. *Sedimentary Geology, v. 39 https://doi.org/10.1016/0037-0738(84)90052-6*, 227–242 https://doi.org/10.1016/0037-0738(84)90052-6.

Al-Mufti, O. N., & Arnott, R. W. (2020). The Origin And Significance Of Convolute Lamination And Pseudonodules In An Ancient Deep-Marine Turbidite System: From Deposition To Diagenesis. *Journal of Sedimentary Research, v. 90*, 480–492, http://dx.doi.org/10.2110/jsr.2020.29.

Anderson, M. M. (1987). Late Precambrian glaciomarine sequence, Conception Group Double Road Point, St. Mary's Bay, Southeast Newfoundland. (pp. 473-476). Geological Society of America Centennial Field Guide-Northeastern Section.

Arnott, R., & Hand, B. (1989). Bedforms, primary structures, and grain fabric in the presence of suspended sediment rain. *Journal of Sedimentary Petrology v. 59*, 1062–1069.

Baas, J. H. (1999). An empirical model for the development and equilibrium morphology of current ripples in fine sand. *Sedimentology*, 123-138.

Baas, J. H., Baker, M. L., Malarkey, J., Bass, S. J., Manning, A. J., Hope, J. A., . . . Parson, D. R. (2019). Integrating field and laboratory approaches for ripple development in mixed sand–clay–EPS. *Sedimentology v.66*, 2749-2768.

Baas, J. H., BAKER, M. L., MALARKEY, J., BASS, S. J., MANNING, A. J., HOPE, J. A., . . . THORNE, P. D. (2019). Integrating field and laboratory approaches for rippledevelopment in mixed sand–clay–EPS. *Sedimentology*, 2749–2768.

Benus, A. P. (1988). Sedimentological context of a deep-water Ediacaran fauna (Mistaken Point, Avalon Zone, eastern Newfoundland). In: Trace Fossils, Small Shelley Fossils and the Precambrian-Cambrian Boundary. . (pp. 8-9). New York : State Museum and Geological Survey Bulletin 463.

Beranek, L. P., Hutter, A. D., Pearcey, S., James, C., Langor, V., Pike, C., . . . Oldham, L. (2023). New evidence for the Baltican cratonic affinity and Tonian to Ediacaran tectonic evolution of West Avalonia in the Avalon Peninsula, Newfoundland, Canada. *Precambrian Research, 390*, 1–19. https://doi.org/10.1016/j.precamres.2023.107046.

Best, J., & Bridge, J. (1992). The morphology and dynamics of low amplitude bedwaves upon upper stage plane beds and the preservation of planar laminae. *Sedimentology, v. 39*, 737-752.

Bouma, A. H. (1962). Sedimentology of some flysch deposits, a graphic approach to facies interpretation. *The Netherlands* (p. 168). Amsterdam: Elsevier.

Bowring, S. M. (2003). Geochronological constraints on terminal Neoproterozoic events and the rise of the Metazoans. In Early Biosphere Evolution Session VI. Nasa Astrobiology Institute (NIA). *General Meeting*, (pp. 113-114).

Bursik, M., & Woods, A. W. (2000). The Effects of Topography on Sedimentation from Particle-Laden Turbulent Density Currents. *Journal of Sedimentary Research 70(1)*, 53-63.

Canfield, D., Knoll, A., Poulton, S., Narbonne, G., & Dunning, G. (2020). Carbon isotopes in clastic rocks and the Neoproterozoic carbon cycle. *American Journal of Science, v. 320, no. 2*, 97–124.

Cardozo, N., & Allmendinger, R. W. (2013). Spherical projections with OSXStereonet. *Computers & Geosciences*, 193-205.

Carey, S. (1997). Influence of convective sedimentation on the formation of widespread tephra fall layers in the deep sea. *Geology 25*, 839–842.

Clapham, M. E. (2003). Paleoecology of the oldest known animal communities: Ediacaran assemblages of Mistaken Point, Newfoundland. (pp. 527-544). Paleobiology, 29.

Cunha, R. S., Tinterri, R., & Magalhaes, P. M. (2017). Annot Sandstone in the Peïra Cava basin: An example of an asymmetric facies distribution in a confined turbidite system (SE France). *Marine and Petroleum Geology v.87*, 60-79.

Dalrymple, R. W., & James, N. P. (2010). *Facies Models 4*. Geological Association of Canada.

Dec, T. O. (1992). Late Precambrian volcaniclastic deposits of the Avalonian Eastport basin (Newfoundland Appalachians): petrofacies, detrital clinopyroxene geochemistry and palaeotectonic implications. *Precambrian Research*, 59, 243–262.

Dickinson, W. (1970). Interpreting detrital modes of graywacke and arkose. *Journal of Sedimentary Petrology*.

Dickinson, W. R. (2009b). Use of U-Pb ages of detrital zircons to infer maximum depositional ages of strata: A test against a Colorado Plateau Mesozoic database. (pp. 115–125). In Earth and Planetary Science Letters Vol. 288, Issues 1–2.

Dickinson, W. R. (1983). Provenance of North American Phanerozoic sandstones in relation to tectonic setting. *Geological Society of America Bulletin*, 94: 222-235.

Dickinson, W. R. (1988). Provenance and Sediment Dispersal in Relation to Paleotectonics and Paleogeography of Sedimentary Basins. In *New Perspectives in Basin Analysis.*

Dickinson, W. R. (2009a). U-Pb ages of detrital zircons in Jurassic eolian and associated sandstones of the Colorado plateau: Evidence for transcontinental dispersal and intraregional recycling of sediment. (pp. 408-433). Bulletin of the Geological Society of America, 121(3-4).

Dodd, T. J., Leslie, A. G., Gillespie, M. R., Dobbs, M. R., Bide, T. P., Kendall, R. S., . . . Chiam, K. (2020). Deep to shallow-marine sedimentology and impact of volcanism within the Middle Triassic Palaeo-Tethyan Semantan Basin, Singapore. *Journal of Asian Earth Sciences*.

Dott, R. H. (1964). Wacke, graywacke and matrix; what approach to immature sandstone classification? *Journal of Sedimentary Research 34(3)*, 625-632.

Folk, R. L. (1980). *Petrology of Sedimentary Rocks.* Austin, Texas.

Gardiner, S. a. (1988). Deep water facies and depositional setting of the Lower Conception Group (Hadrynian), southern Avalon Peninsula, Newfoundland. . (pp. 25: 1579-1954). Canadian Journal of Earth Sciences.

Gladstone, C., McClelland, H. L., Woodcock, N. H., Pritchard, D., & Hunt, J. E. (2017). The formation of convolute lamination in mud-rich turbidites. *Sedimentology, vol. 15, issue 5*.

Goswami, S., & Dey, S. (2018). Facies analysis of tuffaceous volcaniclastics and felsic volcanics of Tadpatri Formation, Cuddapah basin, Andhra Pradesh, India. *International Journal of Earth Sciences*, 107:2689–2710 https://doi.org/10.1007/s005.

Groenenberg, R., Hodgson, D., Prelat, A., Luthi, S., & Flint, S. (2010). Flow–deposit interaction in submarine lobes: Insights from outcrop observations and realizations of a process-based numerical model. *J. Sediment. Res. 80*, 252–267.

Grundvåg, S.-A., Johannessen, E. P., Helland-Hansen, W., & and Plink-Björklund, P. (2014). Depositional Architecture and Evolution of Progradationally Stacked Lobe Complexes in the Eocene Central Basin of Spitsbergen. *Sedimentology 61*, 535–569.

Hiscott, R. N. (1994). Traction-carpet stratification in turbidites; fact or fiction? *Journal of Sedimentary Research, 64*, 209–214.

Hughes, C., & Bruckner. (1971). Late Precambrian Rocks of Eastern Avalon Peninsula, Newfoundland-a Volcanic Island Complex. *Canadian Journal of Earth Sciences, Volume 8*, 899-915.

Hunter, R. (1977). Terminology of Cross-Stratified Sedimentary Layers and Climbing-Ripple Structures. *Journal Of Sedimentary Research, V. 47*, 697–706.

Hutchinson, R. D. (1953). *Geology of Harbour Grace map-area, Newfoundland.* Ottawa: E. Cloutier, Queen's Printer.

Ichaso, A., Dalrymple, R., & Narbonne, G. (2007). Paleoenvironmental and basin analysis of the late Neoproterozoic (Ediacaran) upper Conception and St. John’s groups, west Conception Bay, Newfoundland. *NRC Research Press Web*.

Ingersoll, R. V., & Suczek, C. A. (1979). Petrology and provenance of Neogene sand from Nicobar and Bengal fans, DSDP sites 211 and 218. *Society of Economic Paleontologists and Mineralogists*, Vol.49 (4), p.1217-1228.

Israel, S. (1998). *Geochronological, structural, and stratigraphic investigation of a Precambrian unconformity between the Harbour Main Group and Conception Group, east coast Holyrood Bay Avalon Peninsula, Newfoundland [Unpublished BSc honours thesis].* St John's: Memorial University of Newfoundland.

Jamil, M., Siddiqui, N. A., Rahman, A. H., Ibrahim, N. A., Ismail, M. S., Ahmed, N., . . . Imran, Q. S. (2021). Facies Heterogeneity and Lobe Facies Multiscale Analysis of Deep-Marine Sand-Shale Complexity in the West Crocker Formation of Sabah Basin, NW Borneo. *Appl. Sci. 11* , 5513 https://doi.org/10.3390/app11125513.

Jenkins, R. (1992). Functional and ecological aspects of Ediacaran assemblages. In J. H. Lipps, *Origin and early evolution of the Metazoa* (pp. 131–176). NewYork: Plenum Press.

Jobe, Z. R., Lowe, D. R., & Morris, W. R. (2012). Climbing-ripple successions in turbidite systems: depositional environments, sedimentation rates and accumulation times. *Sedimentology v.59 issue 3*, 867-898.

King, A. F. (1990). *Geology of The St. John's Area.* Memorial University, Department of Earth Sciences. St. John, Canada: Geological Survey Branch Department of Mines and Energy Government of Newfoundland and Labrador.

Klein, G. D. (1975). Resedimented Pelagic Carbonate and Volcaniclastic Sediments and Sedimentary Stuctures in Leg 30 DSDP cores from the western equtorial Pacific. *Geology*, 39-42.

Kneller, B. (1995). Beyond the turbidite paradigm: physical models for deposition of turbidites and their implications for reservoir prediction. *Geological Society of London, Special Publications, 94(1)*, 31–49, https:// doi.org/10.1144/gsl.sp.1995.094.01.04.

Kneller, B. C., & Branney, M. J. (1995). Sustained high-density turbidity currents and the deposition of thick massive sands. *Sedimentology v.42*, 607-616.

Kneller, B. E. (1991). Oblique Reflection of Turbidity Currents. *Geology 19*, 250, doi:10.1130/0091-7613(1991)0192.3.co;2.

Leclair, S. F., & Arnott, R. W. (2005). Parallel lamination formed by high-density turbidity currents. *Journal Of Sedimentary Research, 75*, 1–5, https://Doi.Org/10.2110/Jsr.2005.001.

Lisle, R. J., & Leyshon, e. (2004). Stereographic Projection Techniques for Geologists and Civil Engineers, 2 éd. *Cambridge University Press, Cambridge*, 112.

Lomas, S., & Joseph, P. (2004). Confined Turbidite System. *Geological Society London Special Publications*.

Lowe, D. (1982). Sediment Gravity Flows II: Depositional Models With Special Reference To The Deposits Of High-Density Turbidity Currents. *Journal Of Sedimentary Petrology, V. 52*, 279–297.

Lowe, G., & Arnott, R. (2016). Composition and architecture of braided and sheetflood-dominated ephemeral fluvial strata in the Cambrian-Ordovician Postdam Group: A case example of the morphodynamics of Early Phanerozoic fluvial systems and climate change. (pp. 587-612). Journal of Sedimentary Research v.86.

Manville, V., & Wilson, C. (2004). Vertical density currents: A review of their potential role in the deposition and interpretation of deep-sea ash layers. *Journal of the Geological Society*, 947-958.

Marini, M. M., Ravnås, R., & and Moscatelli, M. (2015). A Comparative Study of Confined vs. Semi-confined Turbidite Lobes from the Lower Messinian Laga Basin (Central Apennines, Italy): Implications for Assessment of Reservoir Architecture. *Mar. Pet. Geology. 63*, 142–165. doi:10.1016/ j.marpetgeo.2015.02.015.

Mason, S., Narbonne, G., Dalrymple, R., & O'Brien, S. (2013). Paleoenvironmental analysis of Ediacaran strata in the Catalina Dome, Bonavista Peninsula, Newfoundland. *Canadian Journal of Earth sciences v.50*, 197-212.

Matthews, J. J., Liu, A. G., Yang, C., McIlroy, D., & Levell, B. &. (2021). *A Chronostratigraphic Framework for the Rise of the Ediacaran Macrobiota: New Constraints from Mistaken Point Ecological Reserve, Newfoundland.* GSA Bulletin .

McCaffrey, W., & Kneller, B. (2001). Process Controls on the Development of Stratigraphic Trap Potential on the Margins of Confined Turbidite Systems and Aids to Reservoir Evaluation. *AAPG Bull. 85*, 971–988, doi:10.1306/8626ca41-173b-11.

Miall. (1985). Architectural elements and boundaries: A new method of facies analysis applied to fluvial deposits. pp. v, 22, p. 261-308.

Mills, A. J., Dunning, G. R., & and Sandeman, H. A. (2020). Lithogeochemical, isotopic, and U–Pb (zircon) age constraints on arc to rift magmatism, northwestern and central Avalon Terrane, Newfoundland, Canada: implications for local lithostratigraphy. *Canadian Journal of Earth Sciences, 23*, 1–23. https://doi.org/10.1139/cjes-2019-0196.

Mills, P. C. (1983). Genesisi and diagnostic value of soft sediment deformation structures - a review. *Sedimentary Geology, 35*, 83-104.

Misra, S. B. (1981). Depositional environment of the Late Precambrian fossil bearing rocks of southeastern Newfoundland, Canada. (pp. 22: 375-382). Journal of the Geological Society of India.

Moores, H. T. (1969). The Position of Graptolites in Turbidites. *Sedimentary Geology, 3*, 241-261.

Muck, M. T., & Underwood, M. B. (1990). Upslope flow of turbidity currents: A comparison among field observations, theory, and laboratory models . *Geology 18(1)*, 54-57.

Mulder, T., & Alexander, J. (2001). The Physical Character of Subaqueous Sedimentary Density Flows and Their Deposits. *Sedimentology 48*, 269–299, doi:10.1046/j.1365-3091.2001.00360.

Mulder, T., Phillipe, R., & Jean-Claude, F. (2009). Hummocky cross-stratification-like structures in deep-sea turbidites: Upper Cretaceous Basque basins (Western Pyrenees, France). *Sedimentology 56*, 997-1015.

Murphy, J. B., Keppie, J. D., Dostal, J., & Nance, R. D. (1999). Neoproterozoic-early Paleozoic evolution of Avalonia. *Geological Society of America Special Paper, 336*, 253–266. https://doi.org/10.1130/0-8137-2336-1.253.

Murphy, J. B., McCausland, P. J., O'Brien, S. J., Pisarevsky, S., & Hamilton, M. A. (2008). Age, geochemistry and Sm-Nd isotopic signature of the 0.76 Ga Burin Group: Compositional equivalent of Avalonian basement? *Precambrian Research, 165(1–2)*, 37–48. https://doi.org/10.1016/j.precamres.2008.05.006.

Mutti, E. (1992). Turbidite Sandstones. *Agip, Istituto di Geologia, Universita di Parma, San Donato Milanese*, 275.

Mutti, E., & Nilsen, T. H. (1981). *Significance of Intraformational Rip-up Clasts in Deep Sea Fan Deposits.* IAS 2nd.

Mutti, E., & Normark, W. (1991). An integrated approach to the study of turbidite systems. In P. In: Weimer, & M. Link, *Seismic Facies and Sedimentary Processes of Submarine Fans and Turbidite Systems* (p. 75e106). New York: Springer-Verlag.

Mutti, E., & Ricci-Lucchi. (1975). Examples of Turbidite Facies and Facies Associations from Selected formation of the Northern Apennines. In E. P.

Mutti, *Turbidite Facies and Facies Association* (pp. 21-37). Nice: Ninth Int. Congr. of Sedimentology, Field trip A 11.

Myrow, P. (1995). Neoproterozoic rocks of the Newfoundland Avalon Zone. Precambrian Research. pp. 73: 123-136.

Nance, R. D. (1996). Basement isotopic signatures and Neoproterozoic paleography of Avalonian-Cadonian and related terranes in the circum-North Atlantic. In: Avalonian And Related Peri-Gondwanan Terranes Of The Circum-North Atlantic. (R. N. Thompson, Ed.) pp. 304: 333-346.

Nance, R. D., Murphy, J. B., & Keppie, J. D. (2002). A Cordilleran Model for The Evolution of Avalonia. (pp. 11-31). Tectonophysics, 352.

Narbonne, G., Dalrymple, R., Gehling, J. G., Wood, D. A., Clapham, M. E., & Sala, R. A. (2001). *Neoproterozoic fossils and environments of the Avalon Peninsula, Newfoundland. In: Field Trip B5.* St. John, Newfoundland: Geological Association of Canada/Mineralogical Association of Canada. Joint annual Meeting.

Narbonne, G., Dalrymple, R., Laflamme, M. G., & Boyce, W. (2005). *Life After Snowball: The Mistaken Point Biota and the Cambrian of Avalon.* North American Paleontological Convention Fieldtrip Guidebook.

O'BRIEN, N. R., NAKAZAWA, K., & TOKUHASHI, S. (1980). Use of clay fabric to distinguish turbiditic and hemipelagic siltstones and silts. *Sedimentology*, 47-61.

O'Brien, S., & King, A. (2004). Ediacaran Fossils from The Bonavista Peninsula (Avalon Zone), Newfoundland: Preliminary Descriptions and Implications for

Regional Correlation. *Current Research (2004) Newfoundland Department of Mines and Energy Geological Survey*, pp. 203-212.

O'Brien, S., Wardle, R., & King, A. (1983). The Avalon Zone: A Pan-African terrane in the Appalachian Orogen of Canada. *Geological Journal, Volume 18*, 195-222.

O'Brien, R., & Slatt, N. R. (1990). Argillaceous Rock Atlas. In *Geological Magazine* (p. xvi + 136 pp). Berlin, Heidelberg, New York, London, Paris, Tokyo, Hong Kong, Barcelona: Springer-Verlag.

Owen, G. (1987). Deformation processes in unconsolidated sands. . *Geol. Soc. Lond. Spec. Publ., 29,* , 11–24.

Parthaniades, E. (1993). Turbulence, Flocculation and Cohesive Sediment Dynamics. In A. J. (Editor), *Coastal and Estuarine Studies: Nearshore and Estuarine Cohesive Sediment Transport Vol. 42* (pp. 40-59). Washington, DC: American Geophysical Union.

Patacci, M., Haughton, P., & and McCaffrey, W. (2015). Flow behaviour of ponded turbidity current. *Journal of Sedimentary Research, 85 (8)*, 885 - 902.

Paton, C. H. (2011). Iolite: Freeware for the visualisation and processing of mass spectrometric data. . (pp. 2508-2518.). J. Anal. At. Spectrom, Vol. 26.

Petrus, A. &. (2012). VizualAge: A novel approach to laser ablation ICP-MS-U-PB geochronology data reduction. (pp. 247-270). Geostandards and Geoanalytical Researc, Vol. 36 (3).

Pettijohn, F. (1975). *Sedimentary Rocks* . New York: Harper and Row Publishers, 2nd Edition, 628 p.

Pickering, K. T., & Hiscott, R. N. (2015). *Deep Marine Systems: Processes, Deposits, Environments, Tectonics and Sedimentation.* UK: American Geophysical Union & Wiley.

Pickering, K., & Hiscott, R. (1985). Contained (reflected) turbidity currents from the Middle Ordovician Cloridorme Formation, Quebec, Canada: an alternative to theantidune hypothesis. *Sedimentology v.32*, 373–394.

Pickering, K., Stow, D., Watson, M., & Hiscott, R. (1986). Deep-Water Facies, Processes and Models: A Review and Classification Scheme for Modern and Ancient Sediments. *Earth-Science Reviews, 23* , 75-174.

Piper, D. (1978). Turbidite muds and silts on deep sea fans and abyssal plains. In: D.J. In S. a. (Editors), *Submarine Canyon and Fan Sedimentation.* Dowden, Hutchinson and Ross, Stroudsburgh, Pa. .

Pollock, J. C. (2009). Early Ordovician rifting of Avalonia and birth of the Rheic Ocean: U-Pb detrital zircon constraints from Newfoundland. *Journal of the Geological Society, 166(3)*, 501–515.

Potter, P. E., Maynard, J. B., & Pryor, W. A. (1980). *Sedimentology of Shale.* New York: Springer-Verlag.

Prelat, A., & Hodgson, D. (2013). The full range of turbidite bed thickness patterns in submarine lobes: Controls and implications. *J. Geol. Soc., 170*, 209–214.

Prelat, A., Hodgson, D., & Flint, S. (2009). Evolution, Architecture and Hierarchy of Distributary Deep-water Deposits: A High-resolution Outcrop Investigation from the Permian Karoo Basin, South Africa. *Sedimentology v.56*, 2132–2154.

Rotzien, J. R., Lowe, D. R., King, P. R., & Browne, G. H. (2014). Stratigraphic architecture and evolution of a deep-water slope channel-levee and overbank apron: The Upper Miocene Upper Mount Messenger Formation, Taranaki Basin. *Marine Petroleum Geology 52* , 22-41.

Satkoski, A. M., Barr, S. D., & Samson, S. D. (2010). Provenance of late Neoproterozoic and Cambrian sediments in Avalonia: Constraints from detrital zircon ages and Sm-Nd isotopic compositions in southern New Brunswick, Canada. *Journal of Geology, 118*, 187–200. https://doi.org/10.1086/649818.

Saylor, J. E., & Sundell, K. E. (2016). Quantifying comparison of large detrital geochronology data sets. *Geosphere, 12(1)*, 203–220. https://doi.org/10.1130/GES01237.1.

Schieber, J., & Southard, J. (2009). Bedload transport of mud by floccule ripples—Direct observation of ripple migration processes and their implications. *Geology, 37*, 483-486.

Serna-Ortiz, S., & Lowe, D. G. (2024). Stratal evolution and provenance of a precambrian delta in a tectonically active terrane: The lower Signal Hill Group, Avalon Zone, Newfoundland. *Precambrian Research 401*.

Shanmugam, G. (2013). New perspectives on deep-water sandstones: Implications. *Petroleum Exploration and Development, 40 (3)*, 294-301.

Shanmugam, G. (2021). The turbidite-contourite-tidalite-baroclinite-hybridite problem: orthodoxy vs. empirical evidence behind the “Bouma Sequence”. *Journal of Palaeogeography*, 10:9.

Sinclair, H., & Tomasso, M. (2002). Depositional Evolution of Confined Turbidite Basins. *Journal of Sedimentary Research* .

Skipton, D. R., Dunning, G. R., & Sparkes, G. W. (2013). Late Neoproterozoic arc-related magmatism in the Horse Cove Complex, eastern Avalon Zone, Newfoundland. . *Canadian Journal of Earth Sciences, 50(4)*, 462–482. https://doi.org/10.1139/cjes-2012-0090.

Sohn, Y. K. (1997). On Traction Carpet Sedimentation. *Journal of Sedimentary Research v.67*, 502-509.

Sohn, Y. K., Park, K. H., & Yoon, S.-H. (2008). Primary versus secondary and subaerial versus submarine hydrovolcanic deposits in the subsurface of Jeju Island, Korea. *Sedimentology*, 899-924.

Sparkes, G., Beranek, L., & Mills, A. (2021). *From the Roof to the Basement: A Tour of Structures, Sedimentary Rocks and Epithermal System of the Northeastern Avalon.* St. John's: Geological Survey of Newefoundland and Labrador.

Spychala, Y., Hodgson, D., Prélat, A., Kane, I., Flint, S., & Mountney, N. (2017). Frontal and lateral submarine lobe fringes: Comparing sedimentary facies, architecture and flow processes. *Sediment. Res, 87*, 75–96.

Stow, D. D. (1985). Deep-sea clastics: Where are we and where are we going? *Geol. Soc. Lond. Spec. Publ, 18*, 67–93.

Stow, D., & Shanmugam, G. (1980). Sequence of structures in fine-grained turbidites: Comparison of recent deep-sea and ancient flysch sediments. *Sediment. Geol, 25*, 23–42.

Stow, D., & Smillie, Z. (2020). Distinguishing between Deep-Water Sediment Facies: Turbidites, Contourites, and Hemipelagites. *Geosciences 10*, 68.

Talling, P., Masson, D., Sumner, E., & Malgesini, G. (2012). Subaqueous sediment density flows: Depositional processes and deposit types. *Sedimentology, v. 59, p. 1937–2003, https:// doi.org/10.1111/j.1365-3091.2012.01353.x.*

Tasgin, C., & Altun, F. (2019). Soft-sediment deformation: deep-water slope deposits of a back-arc basin (middle Eocene-Oligocene Kırkgeçit Formation, Elazığ Basin), Eastern Turkey Arabian. *Journal of Geosciences*, DOI: 10.1007/s12517-019-4872-4.

Tinterri, R., Magalhaes, P. M., Tagliaferri, A., & Cunha, R. (2016). Convolute laminations and load structures in turbidites as indicators of flow reflections and decelerations against bounding slopes. Examples from the Marnoso-arenacea Formation (northern Italy) and Annot Sandstones (south eastern France). *Sedimentary Geology*.

Tinterri, R., Mazza, T., & Magalhaes, P. M. (2022). Contained-Reflected Megaturbidites of the Marnoso-arenacea Formation (Contessa Key Bed) and Helminthoid Flysches (Northern Apennines, Italy) and Hecho Group (South-Western Pyrenees). *Frontier in Earth Science*.

Tucker, M. E. (1982). *The Field Description of Sedimentary Rocks.* University Press - Geology - 112 pages.

Van Daele, M., Meyer, I., Moernaut, J., De Decker, S., Verschuren, D., & De Batist, M. (2017). A revised classification and terminology for stacked and amalgamated turbidites in environments dominated by (hemi)pelagic sedimentation. *Sediment. Geol, 357*, 72–82.

van Staal, C. R., Barr, S. M., McCausland, P. J., Thompson, M. D., & White, C. E. (2021). Tonian–Ediacaran tectonomagmatic evolution of West Avalonia and its Ediacaran–early Cambrian interactions with Ganderia: an example of complex terrane transfer due to arc–arc collision? . *Geological Society, London, Special Publications, 503(1)*, 143–167.

Vermeesch, P. (2013). Multi-sample comparison of detrital age distributions. (pp. 140–146). Chemical Geology, 341.

Vermeesch, P. (2021). Maximum depositional age estimation revisited. *Geoscience Frontiers Volume 12, Issue 2*, 843-850.

Walker, R. G. (1967). Turbidite sedimentary structures and their relationship to proximal and distal depositional environments. *ournal of Sedimentary Research 37 (1)*, 25-43.

Wetzel, R. (2000). Fundamental processes within natural and constructed wetland ecosystem: short-term vs. long-term objectives. *The seventh International Conference on Wetland Systems for Water Pollution Control Proceedings*, (pp. 3-10). Lake Buena Vista, FL.

White, C. E., Barr, S. M., Crowley, J. L., van Rooyen, D., & MacHattie, T. G. (2022). U-Pb zircon ages and Sm-Nd isotopic data from the Cobequid Highlands, Nova Scotia, Canada: New contributions to understanding the Neoproterozoic geologic history of Avalonia. In Y. D. Kuiper, J. B. Murphy, R. D. Nance, R. A. Strachan, & M. D. Thompson, *New Developments in the Appalachian-Caledonian-Variscan Orogen (Special Paper, Vol. 554)* (pp. pp. 135–172). Geological Society of America Special Paper. https://doi.org/10.1130/2021.2554(07).

White, C. E., Barr, S. M., Jamieson, R. A., & Reynolds, P. H. (2001). Neoproterozoic high-pressure/low-temperature metamorphic rocks in the Avalon terrane, Southern New Brunswick, Canada. *Journal of Metamorphic Geology, 19(5)*, 519–530. https://doi.org/10.1046/j.0263-4929.2001.00326.x.

White, J. (1996). Pre-emergent construction of a lacustrine basaltic volcano, Pahvant Butte, Utah (USA). . *Bull. Volcano v.58*, 249-262.

White, J. (2000). Subaqueous Eruption-fed Density Currents and Their Deposits. In: Processes in physical volcanology and volcaniclastic sedimentation: modern and ancient. *Precambrian Res., 101*, 87-109.

Wiedenbeck. M, A. P. (1995). Three natural zircon standards for U-Th-Pb, Lu-Hf, trace element and REE analyses. (pp. 1-23). Geostandards Newsletter, V. 19(1).

Williams, H., & King, A. (1979). *Trepassey Map Area, Newfoundland.* Geological Survey of Canada Memoir 389, 24 p.

Wood, D. A., Dalrymple, R. W., M., N. G., Gehling, J. G., & and Clapham, M. E. (2003). Paleoenvironmental analysis of the late Neoproterozoic Mistaken Point and Trepassey formations, southeastern Newfoundland. Canadian Journal of Earth Sciences.

Wright, J. V., & Mutti, E. (1981). The Dali Ash, Island of Rhodes, Greece: A problem in interpreting submarine volcanigenic sediments. *Bulletin of Volcanology, v. 44*, 153–167.

Yawar, Z., & Schieber, J. (2017). On the origin of silt laminae in laminated shales. *Sedimentary Geology 360*, 22–34.

Zhang, L., Pan, M., & Wang, H. (2017). Deepwater Turbidite Lobe Deposits: A Review of the Research Frontiers. *Acta Geologica Sinica v.91, Issue 1*, 283-300.

Appendix

Appendix A: Deepwater Flow, Deposits, and Mechanism

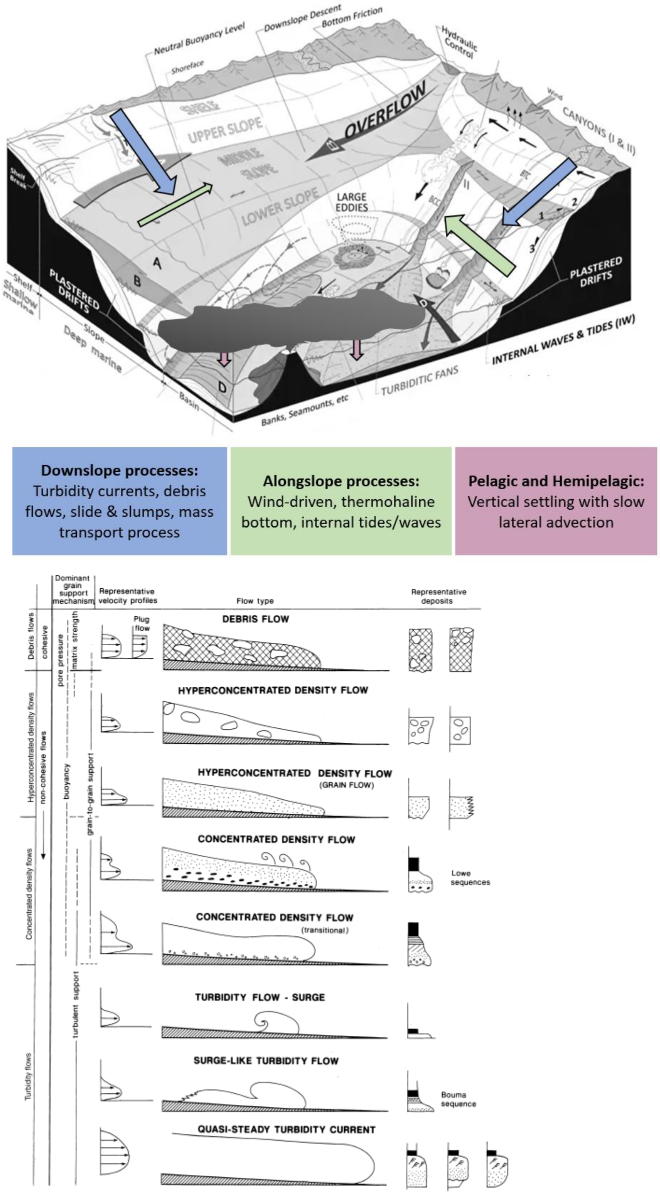

Appendix A. 3D sketch depicting the major oceanographic processes in deep-water environments. The velocity at the seafloor can be affected by density currents and overflows, as well as by deep sea storms, internal waves/ tides, and vertical setting carried by wind or turbulence (*modified from Robesco, 2004*) **(B)** Concept and classification of sediment gravity flow highlighting the mechanism and transformation of debris flow, hyper-concentrated density flow to turbidity flow *(modified from Alexander and Mulder, 2003)*

Appendix B: Methodology and Laboratorium Equipment

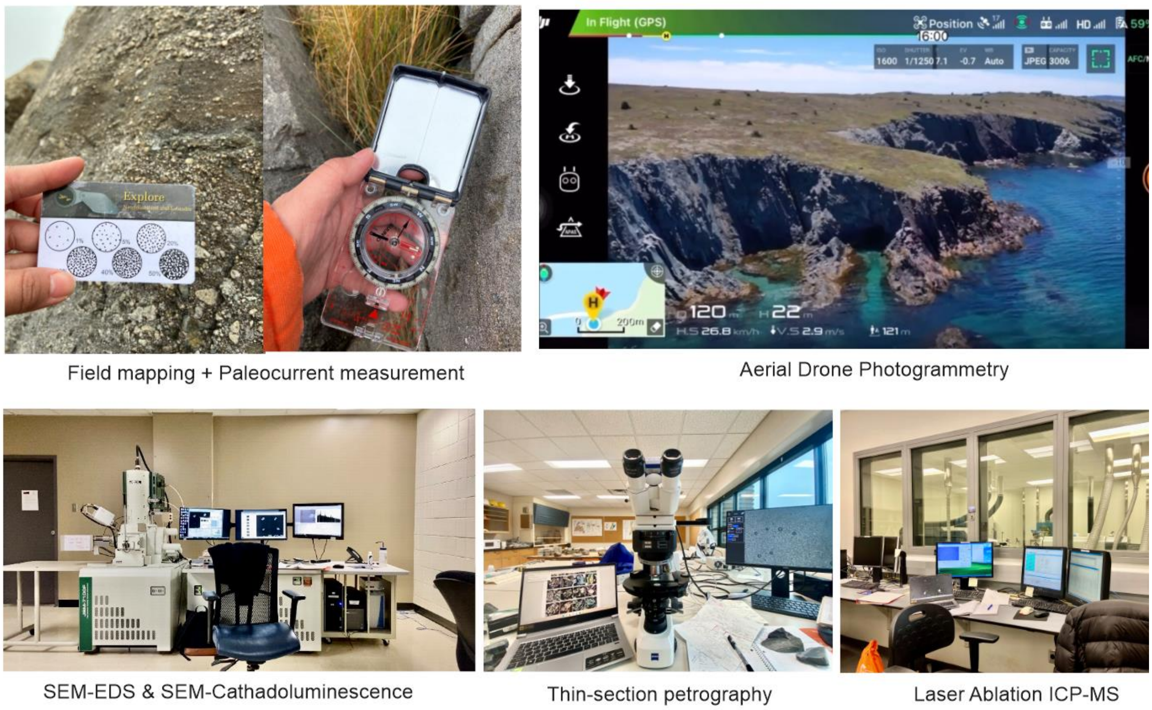

Appendix B. Laboratorium Equipment and Analysis of the research is supported by Memorial University Core Research Equipment & Instrument Training (MUN-CREAIT) Network. These include fieldwork, lapidary, mineral separation, and micro analysis facility.

Appendix C: Hierarchy of Lobe Architectural Elements

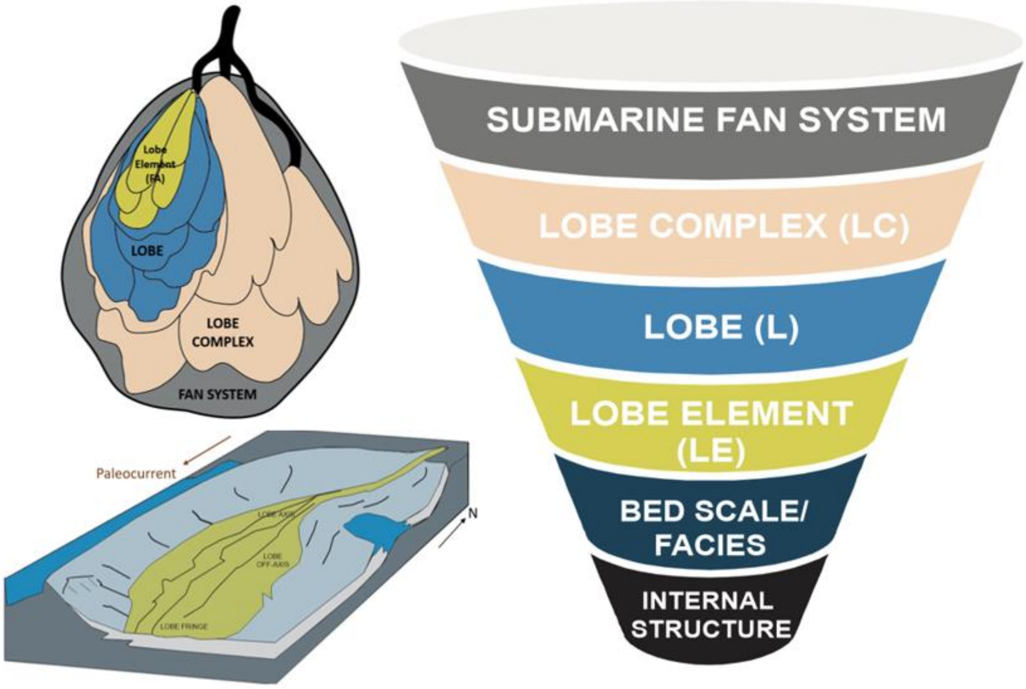

Appendix C. The hierarchy of “architectural elements" and their boundaries directly to the hierarchy of "stratal units". This hierarchical framework of the units is based solely on the physical stratigraphy of the strata and their thickness is time independent. The elements show a progressive increase in scale from the deposit of a single sediment gravity flow (bed) to the accumulated deposits that comprise entire slope or basin floor successions (complex system set)

Appendix D: Larger Version of Measured Sections in Selected Locations

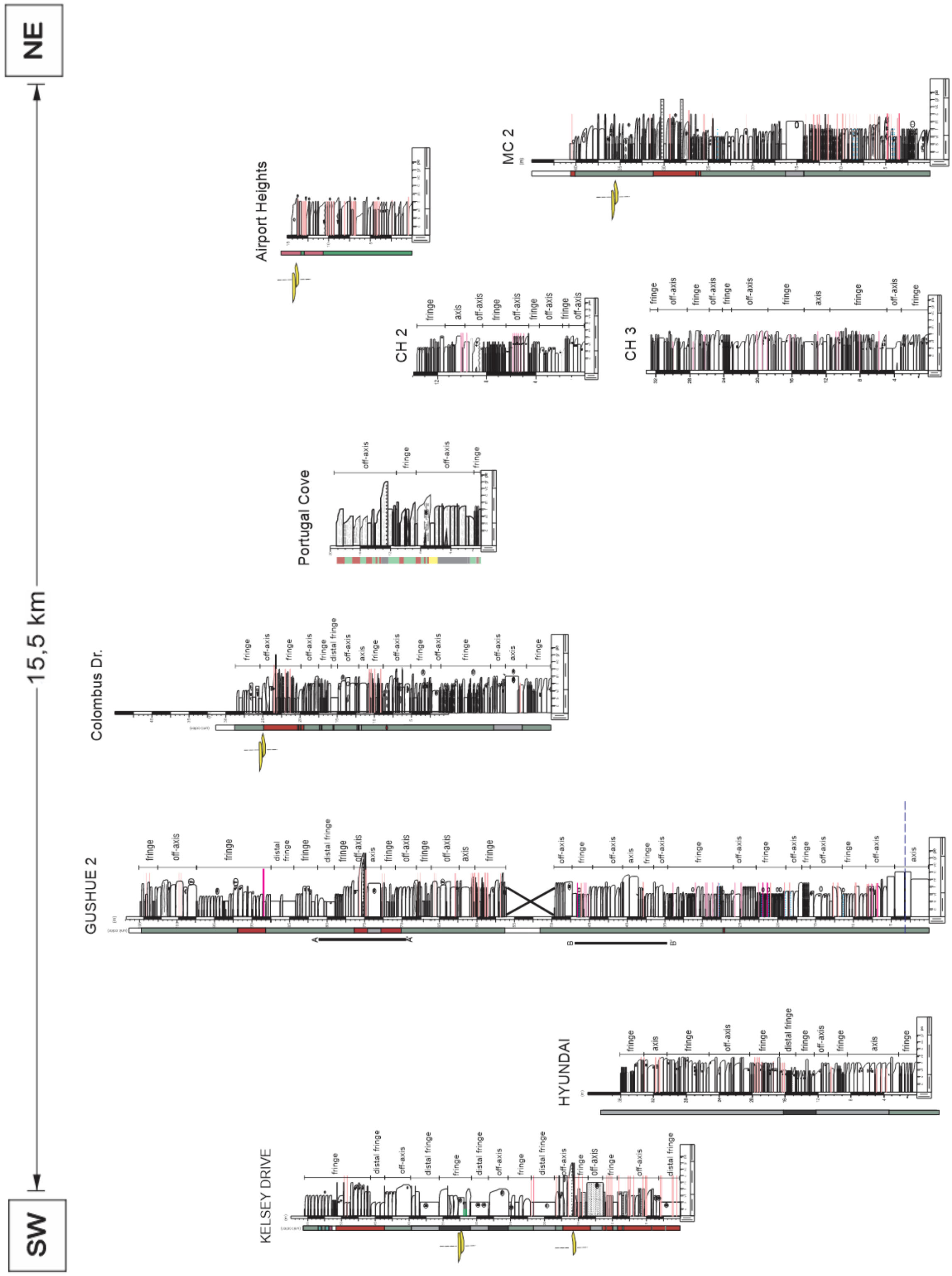

Appendix E: MPF 1 and MPF 2 Paleo flow Measurement (Rose diagram stereonet)

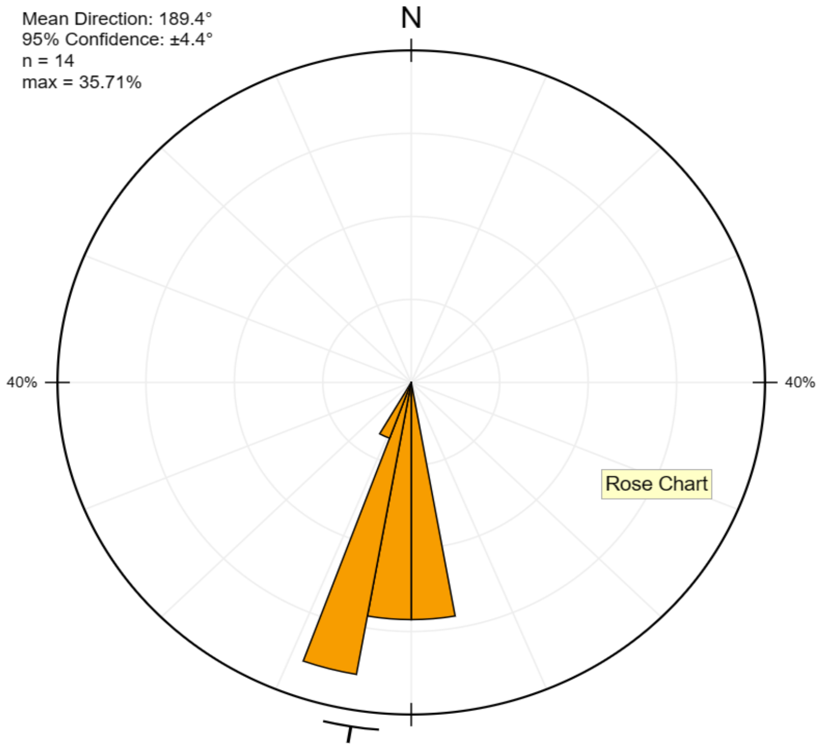

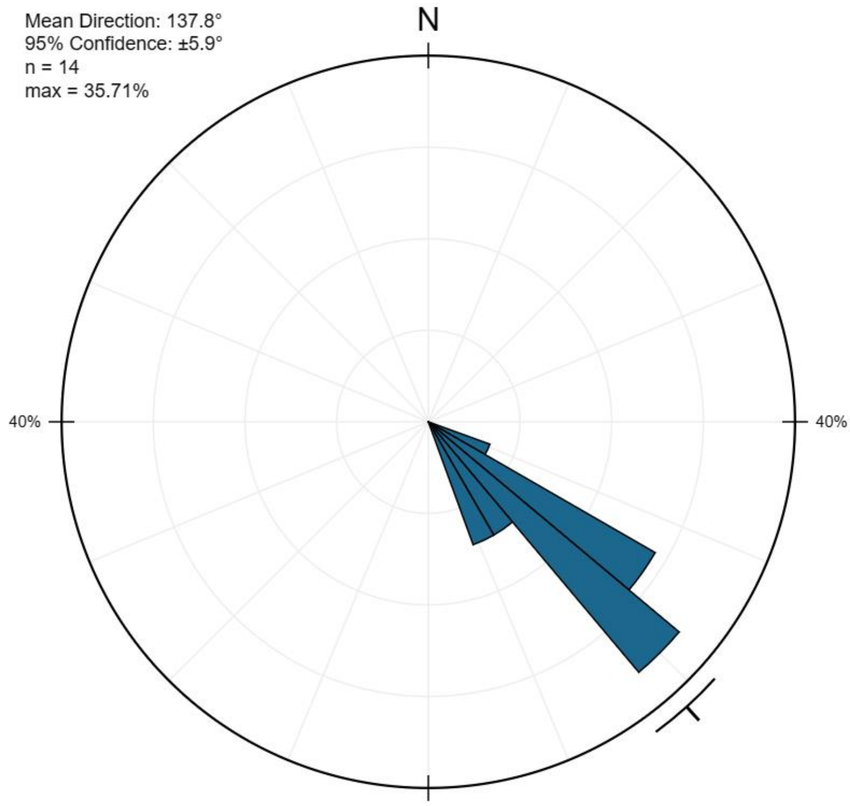

Appendix F: Workflow of U-Pb Geochronology Analysis for the study

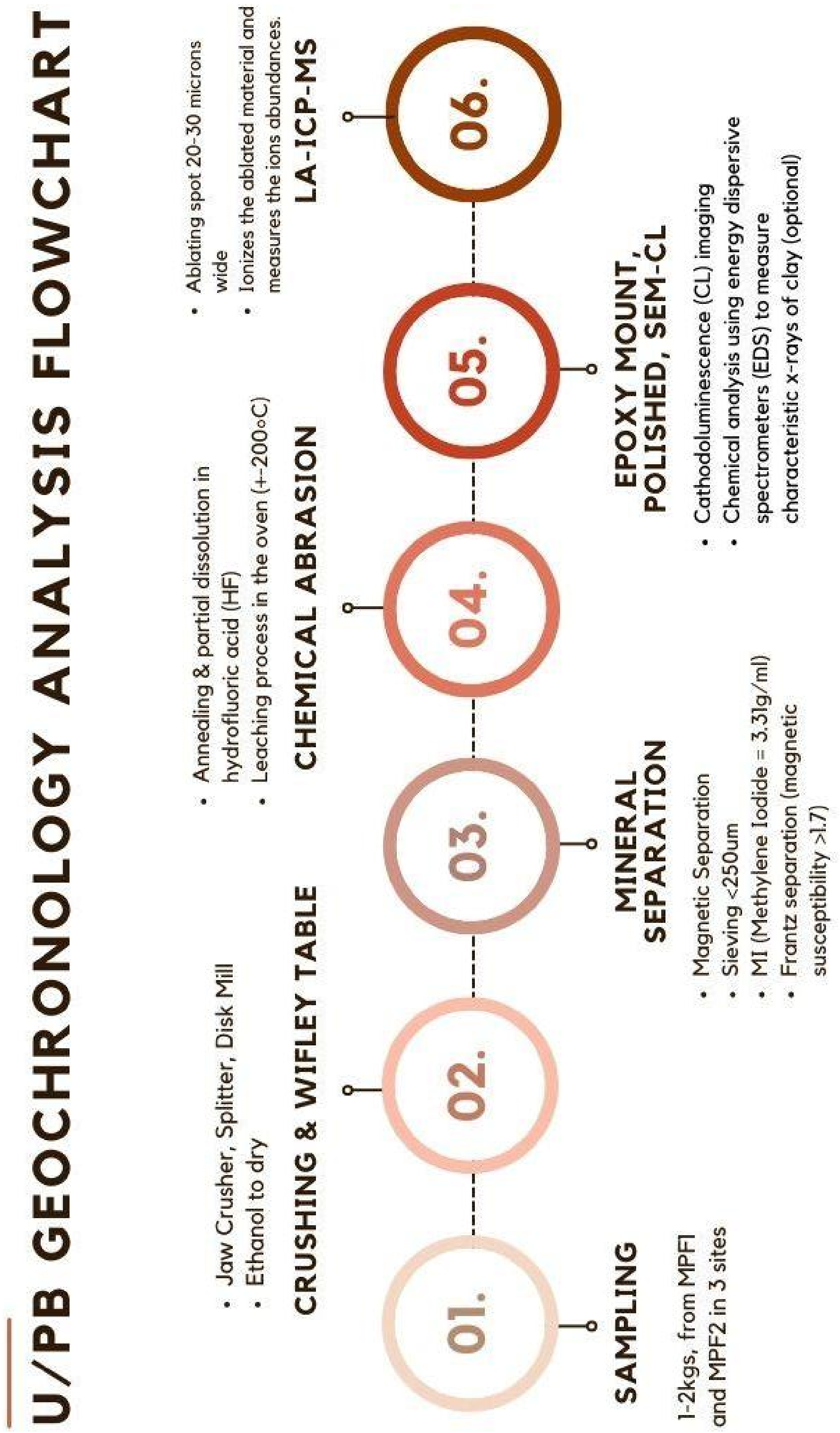

Appendix G: Zircon U-Pb Geochronology data tables

Sample MC-Spaniards Bay (resembling MPF 1) *47.612345, -53.271531*

				Isotopic Ratio							Isotopic Ages								
Sample ID	Zircon ID	U (ppm)	Th (ppm)	207Pb/ 235U	±2SE	206Pb/ 238U	±2SE	Rho	207Pb/ 206U	±2SE	207Pb/ 235U	±2SE	206Pb/ 238U (Age)	±2SE	206Pb/ 207U (Age)	±2SE	Best age	±2SE	Conc %
utput_1_88	2_3-4_1D	319.4	198.2	0.809	0.049	0.0967	0.002	0.29947	0.0603	0.0033	599	25	595	12	571	100	595	12	104
put_1_150	2_28-29_1B	60.4	26.4	0.998	0.045	0.1144	0.0025	0.23051	0.0632	0.0027	699	22	697.8	15	671	87	698	15	104
put_1_167	2_25-26_1B	84.1	160.6	0.802	0.025	0.0969	0.0017	0.21986	0.0598	0.0016	596	14	596.4	10	575	58	596	10	104
put_1_155	2_29_3B	136.9	78	0.843	0.022	0.1007	0.0019	0.25619	0.0603	0.0014	619.3	12	618.4	11	601	49	618	11	103
utput_1_34	2_14-15_3D	45.6	39	0.818	0.038	0.0966	0.0018	0.12597	0.0611	0.0026	604	21	594.5	11	580	91	595	11	103
put_1_185	2_22-23_1A	69.6	53.3	0.834	0.029	0.1001	0.0021	0.28306	0.0609	0.0017	614	16	615	12	603	58	615	12	102
put_1_140	2_32-33_3B	113.2	75.4	0.813	0.037	0.0965	0.0018	0.27469	0.0607	0.0026	600	21	593.6	11	591	89	594	11	100
put_1_192	2_20-21_1D	190.9	113.3	0.799	0.02	0.0971	0.0017	0.35275	0.0599	0.0011	595.4	11	597.6	9.9	596	40	598	10	100
put_1_163	2_27_2A	38.5	24.5	0.9	0.046	0.1039	0.0021	0.19929	0.0623	0.0028	645	24	636.9	13	640	94	637	13	100
utput_1_31	2_14-15_3A	138	98.2	0.781	0.021	0.09419	0.0015	0.22843	0.0599	0.0014	586.2	12	580.2	9	585	50	580	9	99
put_1_181	2_23-24_1D	136.8	101.5	0.792	0.029	0.0947	0.0018	0.44553	0.0604	0.002	590	17	583	11	590	71	583	11	99
put_1_130	2_34-35_3B	205.1	89.8	3.298	0.066	0.2551	0.0045	0.65558	0.093	0.00098	1479	16	1464	23	1483	20	1483	20	99
put_1_159	2_28_4C	240.6	228.4	6.45	0.14	0.3675	0.0062	0.4801	0.1267	0.0018	2036	19	2017	29	2048	24	2048	24	98
put_1_156	2_29_3C	113.6	85.8	0.87	0.025	0.1022	0.0018	0.28522	0.0617	0.0016	634	14	627	11	637	55	627	11	98
utput_1_97	2_1-2_1D	148.5	79.8	0.862	0.021	0.102	0.0016	0.31015	0.0613	0.0012	630.3	11	626.1	9.6	637	42	626	10	98
put_1_122	2_34-35_1A	434	55.1	6.368	0.12	0.3651	0.0062	0.66372	0.1266	0.0011	2026	16	2005	29	2048	16	2048	16	98
put_1_102	2_38-39_1D	169.5	121.8	0.819	0.021	0.0972	0.0018	0.61027	0.0605	0.0012	606	12	598	10	612	42	598	10	98
put_1_138	2_32-33_2C	584	322	1.171	0.025	0.1279	0.0023	0.39504	0.066	0.00095	786	12	776	13	796	30	776	13	97
put_1_151	2_28-29_1C	294	224	0.829	0.023	0.0988	0.0018	0.33665	0.0609	0.0013	612.1	12	607.2	11	623	47	607	11	97
Output_1_8	2_5-6_2C	132.9	36.4	1.096	0.028	0.1228	0.0022	0.4216	0.0648	0.0013	750	13	746.3	12	767	41	746	12	97
put_1_101	2_38-39_1C	96.1	71.8	0.834	0.023	0.0985	0.0019	0.51624	0.0612	0.0013	614	12	605.4	11	624	44	605	11	97
utput_1_74	2_5-6_1A	460	355	5.303	0.095	0.3296	0.0054	0.64585	0.1163	0.0011	1868.2	15	1836	26	1898	17	1898	17	97
put_1_132	2_34-35_3D	246.6	236.9	0.8	0.019	0.0956	0.0016	0.47119	0.0605	0.0011	595.8	11	588.5	9.6	609	43	589	10	97
utput_1_22	2_16_2A	405	160	2.72	0.058	0.2256	0.0037	0.60211	0.0869	0.0011	1332	16	1311	19	1357	24	1357	24	97
put_1_143	2_30-31_1C	285.8	215.1	5.24	0.098	0.3274	0.0056	0.546	0.116	0.0014	1857	16	1825	27	1891	22	1891	22	97
put_1_177	2_24_1B	472	143.2	6.62	0.12	0.3678	0.0065	0.54577	0.1298	0.0014	2060	16	2018	31	2091	19	2091	19	97
put_1_109	2_36-37_1A	174.8	81.1	6.58	0.13	0.3669	0.0062	0.24964	0.1296	0.0013	2056	17	2014	29	2088	17	2088	17	96
utput_1_58	2_9-10_2D	286	214	0.835	0.022	0.0985	0.0019	0.62391	0.0611	0.0012	615	12	606	11	630	41	606	11	96
put_1_127	2_34-35_2B	357	118	2.355	0.044	0.2061	0.0033	0.52931	0.08274	0.00088	1228	13	1208	18	1258	21	1258	21	96
utput_1_92	2_3-4_3B	-2269	-260.3	3.371	0.078	0.2556	0.0042	0.66378	0.0953	0.0015	1496	19	1467	22	1529	27	1529	27	96
utput_1_99	2_1-2_2B	89.8	52.7	0.908	0.027	0.1047	0.0018	0.45238	0.0625	0.0016	654	14	641.8	10	670	49	642	10	96
put_1_120	2_36-37_4C	203.6	130.4	6.531	0.13	0.3641	0.0066	0.71722	0.1296	0.0016	2048	18	2001	29	2091	22	2091	22	96
put_1_197	2_20-21_3A	371	247.4	0.82	0.025	0.0964	0.0021	0.5048	0.0609	0.0013	606	14	593	12	621	45	593	12	95
put_1_104	2_38-39_2C	230.8	168.6	0.834	0.024	0.0983	0.002	0.31222	0.0612	0.0013	614.6	13	604.3	12	633	43	604	12	95
put_1_144	2_30-31_1D	503	430	0.827	0.021	0.09812	0.002	0.50391	0.06108	0.0012	611.2	12	603.3	12	633	45	603	12	95
put_1_176	2_24_1A	422	277	0.83	0.055	0.098	0.0019	0.39082	0.0614	0.003	612	23	602.6	11	633	79	603	11	95
put_1_129	2_34-35_2D	95.3	71.7	0.863	0.026	0.1003	0.002	0.16795	0.062	0.0015	630	14	616	11	649	52	616	11	95
put_1_148	2_30-31_2D	198.1	151.9	0.814	0.023	0.0966	0.0017	0.3816	0.061	0.0014	604	13	594.1	9.8	626	48	594	10	95
put_1_175	2_25-26_3B	249	146	0.812	0.024	0.096	0.0017	0.39222	0.0616	0.0016	601	14	591	9.9	623	57	591	10	95
put_1_142	2_30-31_1A	124.4	98.1	0.834	0.029	0.0972	0.0018	-0.01471	0.0621	0.0021	613	16	598.1	10	631	75	598	10	95
utput_1_63	2_7-8_1D	184.8	80	2.227	0.049	0.1976	0.0034	0.50674	0.0816	0.0013	1188	15	1162	18	1226	31	1226	31	95
put_1_110	2_36-37_1C	285.7	232.9	0.828	0.019	0.09816	0.0016	0.45544	0.0613	0.001	612.7	11	603.5	9.6	637	37	604	10	95
put_1_212	2_18_4B	448	231.3	0.81	0.023	0.096	0.0019	0.3213	0.0611	0.0015	601	13	590.9	11	624	56	591	11	95
utput_1_69	2_7-8_3A	174.2	139.8	0.815	0.022	0.0964	0.0016	0.29543	0.0612	0.0014	604	12	594.2	9.5	628	48	594	10	95
utput_1_71	2_7-8_3D	258	72.4	6.55	0.12	0.3625	0.0062	0.80642	0.1309	0.00092	2051	16	1993	29	2108	12	2108	12	95
put_1_184	2_23-24_2C	361.9	446.3	1.131	0.027	0.123	0.0022	0.46679	0.0659	0.0012	768.2	13	748.9	13	793	36	749	13	94
utput_1_54	2_9-10_1D	80.5	44.6	2.685	0.074	0.2212	0.0044	0.61628	0.0878	0.0017	1321	21	1288	23	1368	38	1368	38	94
utput_1_10	2_40_1B	190.7	128.9	0.828	0.02	0.09755	0.0016	0.39377	0.0614	0.0011	611.2	11	599.9	9.3	640	38	600	9	94
put_1_183	2_23-24_2B	83.9	127.5	0.82	0.048	0.097	0.0023	0.34406	0.0615	0.0027	608	24	596.9	13	637	92	597	13	94
put_1_153	2_29_2B	187.6	120.3	0.804	0.022	0.0957	0.0017	0.38753	0.0612	0.0014	599.2	12	589	10	629	49	589	10	94
put_1_201	2_20-21_4B	126.9	84.2	0.883	0.036	0.1014	0.0027	0.29894	0.0629	0.0026	639	19	622	16	666	81	622	16	93
put_1_172	2_25-26_2D	417	248.9	0.813	0.024	0.0958	0.0016	0.24455	0.0615	0.0014	602	13	589.7	9.7	632	51	590	10	93
put_1_114	2_36-37_2C	178.1	76.5	6.59	0.13	0.3603	0.0061	0.51939	0.1325	0.0016	2056	18	1983	29	2127	21	2127	21	93
utput_1_18	2_23-24_1B	164.6	192.2	0.836	0.027	0.0977	0.0018	0.10178	0.062	0.0018	614	15	600.9	11	645	63	601	11	93
utput_1_30	2_14-15_2D	135.8	103.4	0.81	0.023	0.0955	0.0016	0.21392	0.0614	0.0016	601	13	587.8	9.4	631	53	588	9	93
utput_1_96	2_1-2_1C	2960	-1200	0.846	0.033	0.09869	0.0016	0.22457	0.062	0.0021	621	18	606.7	9.3	652	65	607	9	93
utput_1_72	2_7-8_4A	419.9	229.5	0.804	0.018	0.09529	0.0016	0.62221	0.06087	0.00078	598.1	9.9	586.7	9.4	631	29	587	9	93
utput_1_90	2_3-4_2C	2.70E+04	-915	0.84	0.044	0.0985	0.002	0.40904	0.0617	0.0033	617	23	605.3	12	652	85	605	12	93
put_1_116	2_36-37_3A	55.5	73.5	0.828	0.027	0.0973	0.0018	0.28906	0.0619	0.0018	610	15	598.2	10	645	66	598	10	93
put_1_206	2_18-19_2B	343	213.8	0.843	0.03	0.0983	0.0034	0.66995	0.062	0.0014	622	16	604	20	652	46	604	20	93
put_1_195	2_20-21_2C	233.6	113.4	1.01	0.045	0.113	0.0024	0.52515	0.0647	0.0023	705	21	690	14	745	69	690	14	93
utput_1_35	2_14-15_3B	86.6	40.2	0.83	0.035	0.0962	0.0017	0.20245	0.0619	0.0022	611	18	591.9	10	640	68	592	10	92
put_1_135	2_32-33_1B	716	431.1	0.85	0.02	0.0995	0.0016	0.39347	0.0621	0.0013	623	11	611.5	9.6	662	45	612	10	92
utput_1_16	2_28_4D	357.7	372	9.72	0.21	0.4287	0.0087	0.84951	0.1642	0.0014	2407	19	2299	39	2497	14	2497	14	92
utput_1_59	2_9-10_3A	170.5	142	0.874	0.04	0.1015	0.002	0.33922	0.0623	0.0029	638	19	622.9	12	677	81	623	12	92
put_1_111	2_36-37_1D	133.3	172.1	0.874	0.033	0.1011	0.0019	0.37149	0.0627	0.0019	636	17	620.9	11	675	62	621	11	92
put_1_191	2_20-21_1C	156.1	138.6	0.837	0.023	0.0984	0.0019	0.42311	0.062	0.0013	616.6	13	604.9	11	658	44	605	11	92
put_1_137	2_32-33_2A	447	215.9	8.53	0.18	0.4035	0.0072	0.54739	0.1531	0.002	2288	18	2184	33	2376	22	2376	22	92
put_1_118	2_36-37_3D	220.5	334.8	0.848	0.036	0.0995	0.0018	0.39624	0.0619	0.0023	622	18	611.2	11	665	66	611	11	92
utput_1_55	2_9-10_2A	118.8	54.2	1.129	0.029	0.1231	0.0022	0.48628	0.0663	0.0013	765	14	748.2	13	815	40	748	13	92
put_1_203	2_18-19_1B	169.9	132.6	0.86	0.035	0.0997	0.0022	0.40869	0.0624	0.0023	630	19	612	13	668	71	612	13	92
utput_1_93	2_3-4_3C	-1455	-425	0.836	0.026	0.0979	0.0017	0.11681	0.0625	0.0018	615	14	602.3	10	659	63	602	10	91
utput_1_95	2_1-2_1B	-10350	-808	0.863	0.022	0.1006	0.0017	0.23713	0.0623	0.0014	631	12	617.6	9.7	676	46	618	10	91
utput_1_38	2_12-13_1C	598.3	409.9	0.844	0.023	0.0984	0.0017	0.4903	0.062	0.0012	620.3	13	605	9.8	663	41	605	10	91
put_1_202	2_18-19_1A	534	244	0.856	0.026	0.0996	0.0027	0.65721	0.0624	0.0012	628	14	611	16	670	42	611	16	91
utput_1_32	2_14-15_3B	81.7	50.1	0.811	0.027	0.0952	0.002	0.45703	0.0621	0.0018	600	16	586	13	643	61	586	13	91
put_1_147	2_30-31_2C	128.7	202.9	0.847	0.026	0.0985	0.0018	0.38415	0.0621	0.0017	621	15	605.5	10	665	57	606	10	91
put_1_179	2_23-24_1A	189.3	199.7	0.801	0.03	0.0946	0.0017	0.27264	0.062	0.0019	595	17	582.6	10	640	71	583	10	91
put_1_165	2_27_2C	248	254.5	0.786	0.018	0.09316	0.0016	0.48252	0.06101	0.00089	588.9	10	574.1	10	631	31	574	10	91
put_1_108	2_38-39_4B	241.4	147.3	0.93	0.024	0.1064	0.0018	0.41455	0.0634	0.0013	666	13	651.9	11	719	47	652	11	91
utput_1_76	2_5-6_1C	347.7	166.9	3.781	0.17	0.266	0.0047	0.38233	0.1032	0.0037	1588	32	1520	24	1677	54	1677	54	91
utput_1_64	2_7-8_1E	411	580	0.859	0.061	0.0998	0.002	0.174	0.0625	0.0037	629	28	613	12	677	90	613	12	91
put_1_117	2_36-37_3B	117.6	88.9	0.969	0.039	0.1088	0.0019	0.23684	0.0645	0.0025	686	20	666.9	11	738	69	667	11	90
put_1_188	2_22-23_1B	258.7	248.1	0.811	0.03	0.0954	0.0031	0.674	0.0615	0.0012	601	17	587	18	650	44	587	18	90
utput_1_28	2_14-15_2A	58.4	23.01	0.858	0.093	0.0988	0.002	0.085876	0.0631	0.0061	627	40	607.3	12	673	140	607	12	90
utput_1_25	2_14-15_1A	179.2	139.3	1.107	0.027	0.1206	0.0022	0.56719	0.0664	0.0013	755	13	734	13	815	44	734	13	90

Sample HC-Spaniards Bay (resembling MPF 2) *47.624821, -53.275082*

				Isotopic Ratio							Isotopic Ages							
Sample ID	Zircon ID	U (ppm)	Th (ppm)	207Pb/ 235U	±2SE	206Pb/ 238U	±2SE	Rho	207Pb/ 206U	±2SE	207Pb / 235U	±2SE	206Pb / 238U (Age)	±2SE	206Pb/ 207U (Age)	±2SE	Best age	±2SE	Conc %
out_1_143	4B_33-34_2A	277	225	0.879	0.03	0.1026	0.002	0.3572	0.0622	0.001	639	16	629.5	14	666	44	630	14	95
out_1_149	4B_33-34_4A	1312	1297	0.812	0.023	0.0967	0.002	0.3893	0.0609	1E-03	603.3	13	594.8	11	629	33	595	11	95
out_1_187	4B_29-30_2D	237.6	271.3	0.869	0.029	0.1013	0.002	0.2732	0.0621	0.001	634	16	622.2	12	657	48	622	12	95
out_1_174	4B_31-32_5A	348.6	487.1	0.877	0.029	0.1026	0.002	0.3294	0.0619	0.001	639.4	15	629.8	12	665	48	630	12	95
out_1_223	4B_25-26_2D	109.4	106.3	0.897	0.035	0.1033	0.003	0.4123	0.0627	0.002	648	18	633	15	668	60	633	15	95
out_1_125	4B_35-36_2B	317	119.7	2.327	0.069	0.204	0.004	0.6135	0.0827	0.001	1219	21	1197	22	1263	28	1263	28	95
out_1_152	4B_33-34_5A	276	127.6	0.854	0.032	0.0999	0.002	0.4787	0.0616	0.002	625	18	613.6	13	647	55	614	13	95
out_1_112	4B_37-38_4B	286.1	221.1	0.88	0.03	0.1025	0.002	0.2628	0.0622	0.001	640	16	629	13	663	50	629	13	95
out_1_150	4B_33-34_4C	558	253.1	0.838	0.027	0.0985	0.002	0.5528	0.0614	0.001	617	15	605.5	12	638	42	606	12	95
out_1_113	4B_37-38_4C	202.9	176.3	0.867	0.031	0.1011	0.002	0.3564	0.062	0.002	632	17	620.8	13	654	53	621	13	95
out_1_218	4B_25-26_1B	299.1	167.7	0.838	0.027	0.0991	0.002	0.279	0.0613	0.001	617	15	608.8	11	641	46	609	11	95
tput_1_77	4B_20_1A	50.9	20.2	2.062	0.083	0.1884	0.005	0.5728	0.0796	0.002	1141	28	1112	28	1169	53	1169	53	95
out_1_131	4B_35-36_4B	139.2	114	1.09	0.04	0.1201	0.003	0.3259	0.0656	0.002	746	20	731	15	768	56	731	15	95
tput_1_20	4B_27-28_1C	193.5	187.3	2.512	0.077	0.2137	0.005	0.4178	0.085	0.001	1274	21	1248	25	1309	32	1309	32	95
out_1_169	4B_31-32_3C	296.6	305.9	0.846	0.028	0.0997	0.002	0.4273	0.0613	0.001	621.2	15	612.4	12	642	43	612	12	95
out_1_204	4B_27-28_2C	24	14.94	0.857	0.058	0.0978	0.003	0.2497	0.0639	0.004	623	31	601.3	15	630	130	601	15	95
tput_1_95	4B_18-19_2E	114.7	129.6	0.899	0.035	0.1037	0.002	0.2613	0.0623	0.002	649	18	635.9	13	666	63	636	13	95
out_1_132	4B_35-36_4C	121.2	71.5	0.892	0.038	0.1028	0.002	0.2012	0.063	0.002	644	21	630.9	13	660	74	631	13	96
tput_1_27	4B_25-26_4D	199	146.3	0.857	0.031	0.1004	0.002	0.1478	0.0615	0.002	628	17	617	12	644	55	617	12	96
tput_1_42	4B_23-24_3C	296.6	82.5	0.788	0.025	0.0945	0.002	0.6474	0.0603	0.001	589	14	581.8	12	607	42	582	12	96
out_1_105	4B_37-38_2D	221.8	155.2	0.84	0.027	0.0991	0.002	0.3444	0.0615	0.001	617	15	608.8	12	635	48	609	12	96
out_1_175	4B_31-32_5B	235.9	255	0.847	0.031	0.0994	0.002	0.2165	0.0617	0.002	621	17	610.8	12	637	57	611	12	96
tput_1_40	4B_23-24_3A	136.4	34.48	2.245	0.075	0.2002	0.004	0.4598	0.0815	0.002	1194	23	1176	22	1226	41	1226	41	96
out_1_136	4B_35-36_5C	249	120.7	0.846	0.029	0.1003	0.002	0.605	0.061	0.001	621	16	616	13	642	45	616	13	96
tput_1_31	4B_25-26_5C	384.7	100.8	2.308	0.067	0.2036	0.004	0.7303	0.0821	0.001	1213	21	1195	23	1244	24	1244	24	96
tput_1_19	4B_29-30_3C	391	114.6	2.346	0.07	0.2054	0.004	0.4786	0.0826	0.001	1225	21	1204	22	1253	31	1253	31	96
out_1_199	4B_27-28_1A	163.7	48.95	3.008	0.092	0.2397	0.005	0.5533	0.091	0.002	1409	24	1384	26	1439	31	1439	31	96
out_1_161	4B_31-32_2A	188.1	83.4	4.336	0.13	0.2957	0.006	0.6754	0.1064	0.002	1698	25	1670	30	1734	25	1734	25	96
out_1_221	4B_25-26_2B	208.6	90.3	5.418	0.15	0.3331	0.007	0.563	0.1181	0.002	1886	24	1853	36	1923	23	1923	23	96
out_1_107	4B_37-38_3B	288.2	200.6	0.812	0.025	0.0966	0.002	0.3217	0.0607	0.001	602.8	14	594.6	12	617	44	595	12	96
out_1_194	4B_29-30_4A	75.6	60.1	15.71	0.47	0.5436	0.012	0.6788	0.2092	0.003	2856	28	2797	49	2896	22	2896	22	97
out_1_176	4B_31-32_5C	828	113.2	2.308	0.066	0.204	0.004	0.7147	0.0819	1E-03	1213.7	20	1196.7	21	1239	24	1239	24	97
tput_1_22	4B_25-26_1D	174.3	72	1.715	0.052	0.1679	0.003	0.4253	0.0739	0.001	1013	20	1000	19	1035	34	1035	34	97
out_1_196	4B_29-30_4C	366.3	218.7	4.891	0.14	0.3162	0.006	0.673	0.112	0.001	1799.4	24	1770	31	1829	22	1829	22	97
tput_1_44	4B_23-24_4A	369.7	224.4	0.835	0.025	0.0988	0.002	0.495	0.0609	0.001	615.9	14	607.2	12	627	35	607	12	97
tput_1_15	4B_33-34_4B	100.9	62.6	2.831	0.095	0.2311	0.005	0.4823	0.0879	0.002	1361	25	1340	25	1383	40	1383	40	97
out_1_108	4B_37-38_3C	120.3	82.8	0.84	0.034	0.0987	0.002	0.3898	0.0611	0.002	617	19	606.7	12	626	66	607	12	97
out_1_117	4B_37-38_5C	152.4	34.61	2.314	0.074	0.2042	0.004	0.3665	0.0821	0.002	1217	23	1197	23	1235	39	1235	39	97
out_1_124	4B_35-36_2A	62.2	80.7	4.64	0.15	0.3072	0.007	0.341	0.1093	0.002	1753	27	1726	33	1778	39	1778	39	97
out_1_192	4B_29-30_3F	246	133.9	1.112	0.036	0.1233	0.003	0.5053	0.0653	0.001	758	17	749.6	15	772	39	750	15	97
out_1_200	4B_27-28_1D	171	102.5	0.803	0.029	0.0955	0.002	0.2475	0.0608	0.002	597	17	587.9	12	605	63	588	12	97
tput_1_83	4B_20_4B	313.1	287	0.82	0.031	0.0974	0.002	0.217	0.0608	0.002	607	17	598.9	12	616	63	599	12	97
out_1_145	4B_33-34_2C	127.5	111.9	`	0.029	0.0915	0.002	0.3188	0.06	0.002	568	17	564.1	11	580	62	564	11	97
tput_1_52	4B_23-24_6B	152.9	81.6	0.821	0.032	0.0971	0.002	0.2298	0.0611	0.002	606	18	597.5	12	614	63	598	12	97
out_1_227	4B_25-26_3D	120	103.2	0.868	0.03	0.1022	0.002	0.6056	0.0614	0.001	633	16	627.3	13	644	48	627	13	97
out_1_160	4B_31-32_1D	531	211.6	3.604	0.1	0.2684	0.005	0.6772	0.0974	0.001	1549.3	22	1532	27	1572	21	1572	21	97
out_1_133	4B_35-36_4D	92.1	65.7	0.822	0.043	0.0972	0.002	0.1332	0.0614	0.003	606	23	598	13	612	86	598	13	98
tput_1_89	4B_18-19_1B	68.1	62	0.882	0.048	0.1027	0.002	0.1864	0.0624	0.003	640	25	630	14	644	89	630	14	98
out_1_134	4B_35-36_5A	137.4	122.2	0.849	0.03	0.1002	0.002	0.4387	0.0613	0.001	622	17	615.4	13	629	52	615	13	98
tput_1_80	4B_20_3A	264	181.8	3.67	0.1	0.2712	0.005	0.6938	0.098	0.001	1564	23	1547	27	1581	23	1581	23	98
tput_1_17	4B_31-32_3D	460.9	312.2	4.526	0.13	0.3062	0.006	0.7124	0.1075	0.001	1738	23	1721	30	1755	22	1755	22	98
out_1_191	4B_29-30_3E	224.4	196.8	0.824	0.026	0.0981	0.002	0.1067	0.0608	0.001	609.1	14	603.2	11	615	46	603	11	98
tput_1_24	4B_25-26_4A	243.1	67.2	4.899	0.14	0.3187	0.006	0.5046	0.1112	0.001	1801	24	1783	32	1815	22	1815	22	98
tput_1_32	4B_25-26_5D	143.4	99.3	0.789	0.14	0.0941	0.003	0.044	0.0605	0.018	589	47	580	15	590	160	580	15	98
utput_1_9	4B_18-19_1C	184.5	76.4	5.277	0.15	0.3321	0.007	0.5495	0.1151	0.002	1864	24	1848	33	1877	24	1877	24	98

Appendix G: Zircon U-Pb Geochronology data tables (*continued*)

Sample ID	Zircon ID	U (ppm)	Th (ppm)	207Pb/ 235U	±2SE	206Pb/ 238U	±2SE	Rho	207Pb/ 206U	±2SE	207Pb / 235U	±2SE	206Pb/ 238U (Age)	±2SE	206Pb/ 207U (Age)	±2SE	Best age	±2SE	Conc %
				Isotopic Ratio							Isotopic Ages								
tput_1_206	4B_27-28_2E	313.6	186.9	0.833	0.029	0.0978	0.0021	0.3593	0.062	0.0015	614.4	16	601.4	13	666	50	601	13	90
tput_1_141	4B_33-34_1C	175.1	203	0.859	0.032	0.0989	0.0021	0.3598	0.0626	0.0016	628	18	607.8	12	672	56	608	12	90
tput_1_100	4B_37-38_1C	150	94.9	0.767	0.029	0.0909	0.0019	0.3005	0.0612	0.0017	576	17	560.9	11	620	61	561	11	90
tput_1_165	4B_31-32_2E	577	615	0.771	0.026	0.0917	0.0021	0.5038	0.061	0.0012	579.2	15	565.8	12	625	39	566	12	91
tput_1_122	4B_35-36_1C	389.7	325.4	0.854	0.044	0.0991	0.0022	0.3818	0.0624	0.0025	625	22	609.3	13	673	67	609	13	91
tput_1_139	4B_35-36_6B	114.1	69.5	0.772	0.034	0.0909	0.0019	0.1471	0.0614	0.0022	578	19	560.6	11	618	71	561	11	91
tput_1_159	4B_31-32_1B	232.2	218.9	0.861	0.03	0.1	0.0022	0.153	0.0625	0.0015	630	17	614	13	675	51	614	13	91
utput_1_58	4B_21-22_1B	133.1	118	0.84	0.045	0.0969	0.0021	0.1304	0.0628	0.0027	616	23	596	12	655	82	596	12	91
utput_1_98	4B_18-19_3D	229.2	185	0.817	0.03	0.0956	0.002	0.2949	0.0619	0.0016	605	16	588.4	12	646	55	588	12	91
Output_1_4	4B_23-24_2D	173.6	83.3	0.747	0.027	0.089	0.0018	0.3639	0.0607	0.0016	565	16	549.6	11	602	57	550	11	91
utput_1_50	4B_23-24_5D	287.1	126.9	0.833	0.032	0.0974	0.0021	0.2724	0.062	0.0017	614	17	599.1	12	656	55	599	12	91
tput_1_126	4B_35-36_2C	202.5	164.8	0.783	0.027	0.0928	0.0021	0.2387	0.0606	0.0016	586	15	572	12	626	57	572	12	91
tput_1_138	4B_35-36_6A	263.7	117.1	0.819	0.031	0.0961	0.0021	0.0815	0.0611	0.0019	607	16	591.3	12	647	66	591	12	91
tput_1_144	4B_33-34_2B	142.7	131	0.861	0.03	0.0996	0.002	0.3526	0.0626	0.0015	629	16	612	12	669	49	612	12	91
tput_1_172	4B_31-32_4C	579	616	0.845	0.028	0.0989	0.0021	0.4022	0.0618	0.0012	621	15	607.7	12	664	45	608	12	92
tput_1_219	4B_25-26_1C	111.4	115	0.804	0.034	0.0944	0.0021	0.265	0.0618	0.0022	597	19	581.3	12	635	79	581	12	92
tput_1_181	4B_29-30_1E	125.3	80.7	0.796	0.037	0.093	0.0019	0.3643	0.062	0.0023	591	20	573.4	11	626	76	573	11	92
tput_1_109	4B_37-38_3D	214.6	224.4	0.841	0.031	0.0981	0.0021	0.1838	0.0619	0.0016	618	17	603.2	12	658	57	603	12	92
tput_1_193	4B_29-30_3G	271	174	1.097	0.04	0.1203	0.0036	0.6517	0.0662	0.0017	750	20	732	21	798	52	732	21	92
utput_1_10	4B_37-38_1B	215.9	161.8	0.902	0.031	0.1037	0.0022	0.2731	0.0631	0.0017	651	17	636	13	693	55	636	13	92
utput_1_11	4B_37-38_3E	158.1	129.6	1.106	0.034	0.1216	0.0026	0.4395	0.0661	0.0013	755	17	740	15	806	42	740	15	92
tput_1_156	4B_33-34_6A	520	405	0.814	0.027	0.0961	0.0022	0.3894	0.0616	0.0012	603	15	591.3	13	644	42	591	13	92
utput_1_36	4B_23-24_1C	249.7	149.6	0.831	0.03	0.0978	0.0022	0.4593	0.0614	0.0014	613	16	601	13	654	51	601	13	92
tput_1_151	4B_33-34_4D	636	622	0.826	0.028	0.0973	0.0019	0.384	0.0617	0.0013	612	15	598.4	11	651	45	598	11	92
tput_1_180	4B_29-30_1D	387.7	254.6	0.831	0.034	0.0978	0.0022	0.4027	0.0616	0.0017	612.9	18	601.2	13	653	58	601	13	92
tput_1_209	4B_27-28_3C	365	221.9	0.834	0.027	0.0987	0.002	0.5704	0.0617	0.0011	616.2	15	606.8	12	659	36	607	12	92
tput_1_148	4B_33-34_3B	378	258.8	0.817	0.028	0.0965	0.002	0.2785	0.0614	0.0015	605.3	16	594	12	644	49	594	12	92
tput_1_127	4B_35-36_2D	326.7	162.6	0.772	0.025	0.0924	0.0019	0.4097	0.0604	0.0013	580	14	569.4	11	617	46	569	11	92
utput_1_64	4B_21-22_3C	163.3	106.2	0.772	0.028	0.0915	0.0019	0.5682	0.061	0.0015	578	17	564.1	12	611	54	564	12	92
tput_1_167	4B_31-32_3A	166.5	76.7	0.887	0.031	0.1027	0.002	0.1796	0.0625	0.0016	643	17	630.2	12	682	54	630	12	92
utput_1_60	4B_21-22_2C	368	342	0.806	0.026	0.095	0.0021	0.2835	0.0613	0.0012	599	15	585	12	633	43	585	12	92
utput_1_51	4B_23-24_6A	352.7	219.1	0.886	0.041	0.1023	0.0024	0.4599	0.0626	0.0021	643	21	627.7	14	679	68	628	14	92
tput_1_103	4B_37-38_2B	157.6	79.1	0.867	0.035	0.0997	0.0023	0.2689	0.0628	0.002	631	19	613	13	663	69	613	13	92
utput_1_46	4B_23-24_4C	165.8	102.6	0.744	0.029	0.0885	0.0019	0.3199	0.0605	0.0018	563	17	546.7	11	591	63	547	11	93
utput_1_41	4B_23-24_3B	43.3	35.9	3.81	0.14	0.2691	0.0066	0.4964	0.1024	0.0026	1588	30	1535	33	1659	48	1659	48	93
tput_1_203	4B_27-28_2B	488	215	0.82	0.025	0.0972	0.002	0.5232	0.0614	0.001	606.9	14	598.1	11	645	34	598	11	93
utput_1_99	4B_18-19_4A	392	319.7	0.807	0.026	0.0954	0.0019	0.3859	0.0613	0.0012	600	15	587.3	11	633	42	587	11	93
tput_1_228	4B_25-26_3E	74.7	22.19	0.842	0.034	0.0978	0.0024	0.3048	0.0621	0.0019	618	18	601.3	14	648	62	601	14	93
tput_1_198	4B_29-30_4E	77.8	29.5	0.869	0.047	0.0994	0.0023	0.3226	0.0632	0.0031	630	25	610.8	13	658	96	611	13	93
tput_1_182	4B_29-30_1F	207.1	214	0.772	0.033	0.0915	0.0019	0.3698	0.061	0.002	578	18	565.6	11	609	66	566	11	93
tput_1_179	4B_29-30_1B	55.2	46.3	0.885	0.079	0.0998	0.0024	0.0108	0.0645	0.0059	635	37	613	14	660	140	613	14	93
utput_1_26	4B_25-26_4C	351.2	164.8	0.818	0.026	0.0967	0.002	0.4005	0.0613	0.0011	606	14	594.7	11	640	41	595	11	93
tput_1_128	4B_35-36_3A	375.4	145.6	0.781	0.023	0.0933	0.0019	0.5392	0.0606	0.0009	585.3	14	575	11	618	33	575	11	93
utput_1_43	4B_23-24_3D	58	32.38	0.846	0.049	0.0981	0.0023	0.4218	0.0625	0.0026	619	25	603	14	648	96	603	14	93
Output_1_8	4B_20_2B	94.8	130.5	3.248	0.1	0.2468	0.0058	0.6011	0.0955	0.0018	1466	25	1421	30	1527	35	1527	35	93
tput_1_146	4B_33-34_2D	740	589	0.835	0.028	0.0981	0.002	0.4061	0.0616	0.0013	615	16	603.4	12	648	44	603	12	93
utput_1_57	4B_21-22_1A	186.7	248	0.791	0.03	0.0933	0.0021	0.2481	0.0612	0.0018	590	17	576.8	13	619	65	577	13	93
tput_1_101	4B_37-38_1D	438.3	262	0.807	0.025	0.0957	0.002	0.4036	0.0611	0.0011	600	14	589	12	631	41	589	12	93
utput_1_76	4B_21-22_7B	368.7	803	1.12	0.033	0.1229	0.0027	0.2302	0.0661	0.0012	762.2	16	747	15	800	39	747	15	93
tput_1_205	4B_27-28_2D	92.1	27.14	2.183	0.078	0.1937	0.0041	0.4102	0.0815	0.0019	1172	24	1141	22	1221	46	1221	46	93
tput_1_140	4B_33-34_1B	162.6	228.2	0.796	0.027	0.0937	0.0019	0.2309	0.0609	0.0014	593	16	577.6	11	618	48	578	11	93
tput_1_130	4B_35-36_4A	135.4	66.3	0.851	0.031	0.0992	0.0021	0.2285	0.0622	0.0017	623	17	609.6	12	652	60	610	12	93
tput_1_168	4B_31-32_3B	431	350	0.827	0.025	0.0976	0.002	0.2917	0.0614	0.0011	611.4	14	600.3	12	642	38	600	12	94
tput_1_225	4B_25-26_3B	333.2	245.9	0.844	0.027	0.0994	0.0023	0.6719	0.0615	0.001	622.1	14	610.8	13	653	33	611	13	94
tput_1_114	4B_37-38_4D	195.9	192.5	0.827	0.038	0.0969	0.002	0.3547	0.0618	0.0022	610	20	596	12	637	77	596	12	94
tput_1_195	4B_29-30_4B	167.3	75.9	0.8	0.03	0.0945	0.002	-0.032	0.0616	0.002	595	17	581.8	12	621	69	582	12	94
utput_1_45	4B_23-24_4B	451.3	340	0.805	0.025	0.0958	0.0019	0.5085	0.0607	0.001	599.1	14	589.8	11	629	34	590	11	94
utput_1_82	4B_20_4A	637	357.8	1.771	0.051	0.1695	0.0036	0.6728	0.0754	0.0009	1034	18	1009	20	1076	25	1076	25	94
utput_1_90	4B_18-19_1D	157.8	66.27	0.843	0.033	0.0984	0.0021	0.3312	0.062	0.0018	618	18	604.9	12	645	61	605	12	94
utput_1_97	4B_18-19_3C	758	633	0.816	0.024	0.0971	0.002	0.5387	0.061	0.0008	605.1	13	597.5	12	637	30	598	12	94
utput_1_79	4B_20_2A	120.5	158.1	0.792	0.031	0.094	0.002	0.3914	0.0611	0.0018	591	18	578.8	12	617	63	579	12	94
tput_1_154	4B_33-34_5C	182.1	363	0.84	0.034	0.098	0.0021	0.2081	0.0622	0.0019	616	19	602.4	12	642	69	602	12	94
tput_1_106	4B_37-38_3A	571	325	0.817	0.025	0.0969	0.002	0.3667	0.0609	0.001	605.9	14	595.9	11	635	37	596	11	94
tput_1_147	4B_33-34_3A	799	625	0.789	0.023	0.0941	0.0019	0.3783	0.0607	0.001	590	14	580	11	618	37	580	11	94
utput_1_86	4B_20_5B	300.1	202.4	0.821	0.028	0.0972	0.002	0.4074	0.0612	0.0013	607.4	15	598	12	637	46	598	12	94
utput_1_87	4B_20_5C	495	537	0.751	0.027	0.0902	0.0019	0.5699	0.0601	0.0012	568	15	556.8	11	593	44	557	11	94
utput_1_28	4B_25-26_4E	146	87.4	0.749	0.027	0.0902	0.0019	0.549	0.0601	0.0015	566	16	557	11	593	58	557	11	94
utput_1_71	4B_21-22_5D	350.2	105.4	1.762	0.053	0.1693	0.0034	0.3798	0.0754	0.0011	1031	19	1008	19	1073	30	1073	30	94
tput_1_210	4B_27-28_4A	181.2	307.2	0.857	0.031	0.1004	0.0021	0.2261	0.0614	0.0015	629	17	616.7	12	656	53	617	12	94
tput_1_118	4B_37-38_5D	246.8	217.5	0.863	0.029	0.1007	0.0021	0.3478	0.0617	0.0013	630	16	618.6	12	658	47	619	12	94
tput_1_153	4B_33-34_5B	147.8	63.9	0.84	0.037	0.0979	0.0023	0.2475	0.0623	0.0022	616	20	601.8	13	640	76	602	13	94
tput_1_202	4B_27-28_2A	282.7	278.2	0.866	0.027	0.1015	0.002	0.4366	0.062	0.0012	632.7	15	623.1	12	662	41	623	12	94
utput_1_34	4B_23-24_1A	177	89.2	0.821	0.034	0.0968	0.0021	0.2823	0.0613	0.0018	608	18	596	13	633	63	596	13	94
utput_1_68	4B_21-22_4D	268.6	118	0.85	0.027	0.0995	0.002	0.3612	0.0614	0.0012	623	15	611.2	12	648	42	611	12	94
utput_1_66	4B_21-22_4B	313.6	186.2	0.768	0.025	0.092	0.0018	0.5928	0.0602	0.0012	578	14	567.2	11	601	41	567	11	94

Appendix G: Zircon U-Pb Geochronology data tables (*continued*)

Sample ID	Zircon ID	U (ppm)	Th (ppm)	Isotopic Ratio 207Pb/ 235U	±2SE	206Pb/ 238U	±2SE	Rho	207Pb/ 206U	±2SE	Isotopic Ages 207Pb/ 235U	±2SE	206Pb/ 238U (Age)	±2SE	206Pb/ 207U (Age)	±2SE	Best age	±2SE	Conc %
put_1_163	4B_31-32_2C	226	179.7	5.424	0.15	0.3368	0.007	0.627	0.1164	0.0015	1887	24	1871	32	1898	22	1898	22	99
utput_1_59	4B_21-22_1C	304.3	167.7	0.798	0.03	0.0951	0.002	0.304	0.0606	0.0016	593	17	585.5	11	593	59	586	11	99
utput_1_30	4B_25-26_5B	66.6	31	2.981	0.1	0.2402	0.005	0.423	0.0893	0.0019	1403	25	1387	26	1404	41	1404	41	99
put_1_135	4B_35-36_5B	236.8	230.9	0.837	0.03	0.0997	0.002	0.466	0.0609	0.0012	618	16	612.7	12	620	44	613	12	99
utput_1_67	4B_21-22_4C	145.6	93.7	0.814	0.03	0.0972	0.002	0.242	0.0607	0.0016	603	17	598.1	12	605	60	598	12	99
put_1_189	4B_29-30_3B	172.1	117.1	5.42	0.15	0.3376	0.007	0.544	0.116	0.0015	1887	24	1875	33	1892	24	1892	24	99
put_1_142	4B_33-34_1D	217.9	101.7	0.749	0.03	0.0912	0.002	0.394	0.0595	0.0014	567	15	562.3	12	566	51	562	12	99
put_1_186	4B_29-30_2C	614	323	3.616	0.1	0.2713	0.006	0.82	0.0966	0.0011	1551	23	1547	29	1555	22	1555	22	99
utput_1_73	4B_21-22_6C	175	159.1	0.873	0.03	0.1031	0.002	0.412	0.0614	0.0014	636	16	633	13	635	50	633	13	100
put_1_170	4B_31-32_4A	236.4	205.6	0.791	0.03	0.0945	0.002	0.39	0.0602	0.0018	589	18	582	12	582	68	582	12	100
utput_1_85	4B_20_5A	167.4	98.2	0.821	0.03	0.0982	0.002	0.267	0.0605	0.0016	609	18	603.5	12	602	65	604	12	100
utput_1_56	4B_23-24_7C	130.6	99.7	0.815	0.03	0.097	0.002	0.242	0.0605	0.0019	606	17	596.4	13	589	69	596	13	101
put_1_115	4B_37-38_5A	282.6	146.6	0.867	0.03	0.1033	0.002	0.302	0.061	0.0012	633	15	633.5	12	624	42	634	12	102
put_1_104	4B_37-38_2C	80.2	62.3	0.814	0.04	0.0974	0.002	0.128	0.0611	0.0022	601	20	599	13	590	86	599	13	102
utput_1_61	4B_21-22_2D	358.9	188.9	0.89	0.03	0.1054	0.002	0.403	0.0613	0.0011	646	14	645.9	13	636	37	646	13	102
put_1_216	4B_27-28_5D	262.1	188.4	0.831	0.03	0.0996	0.002	0.272	0.0605	0.0013	614.1	15	612	12	602	49	612	12	102
put_1_110	4B_37-38_3F	243.9	124.4	1.975	0.06	0.1873	0.004	0.417	0.0761	0.0012	1106	21	1109	22	1090	31	1090	31	102
put_1_188	4B_29-30_3A	22.04	12.04	0.866	0.06	0.0994	0.003	-0.029	0.0635	0.0042	625	34	610.7	15	600	140	611	15	102
utput_1_96	4B_18-19_3B	93.8	44.7	0.8	0.04	0.0965	0.002	0.168	0.0602	0.0021	594	20	593.7	12	582	71	594	12	102
utput_1_91	4B_18-19_2A	77.4	55.6	0.832	0.06	0.1	0.002	0.396	0.0605	0.0042	610	31	614	12	600	110	614	12	102
put_1_164	4B_31-32_2D	123.9	140.6	0.877	0.03	0.1041	0.002	0.294	0.0611	0.0017	637	18	638.1	13	620	65	638	13	103
put_1_220	4B_25-26_2A	354.7	454.8	1.053	0.04	0.1204	0.003	0.44	0.0633	0.0014	729	17	733	16	708	45	733	16	104

Sample HC-Ecological Reserves (resembling MPF 2) *46.667321, -53.075113*

Sample ID	Zircon ID	U (ppm)	Th (ppm)	Isotopic Ratio 207Pb/ 235U	±2SE	206Pb/ 238U	±2SE	Rho	207Pb/ 206U	±2SE	Isotopic Ages 207Pb/ 235U	±2SE	206Pb/ 238U (Age)	±2SE	206Pb/ 207U (Age)	±2SE	Best age	±2SE	Conc %
Output_1_	3_24-25_1A	671	14.22	1.696	0.035	0.1653	0.0037	0.62509	0.07414	0.0007	1006.5	13	986	20	1045	20	1045	15	94
Output_1_	3_24-25_1B	180	132.5	0.843	0.026	0.098	0.0025	0.49155	0.0617	0.0016	619	15	602.5	15	647	55	603	14	93
Output_1_	3_24-25_1C	31.57	23.75	0.84	0.049	0.0983	0.0025	0.10108	0.0621	0.0035	618	29	604	15	620	130	604	31	97
Output_1_	3_24-25_1D	166.5	106.8	0.836	0.029	0.0978	0.0024	0.49699	0.0615	0.0015	616	16	601.5	14	644	55	602	26	93
Output_1_	3_24-25_1E	193.8	119.1	0.831	0.025	0.0973	0.0025	0.2167	0.0617	0.0017	613	14	598	15	650	61	598	13	92
Output_1_	3_25_2A	52.9	111.8	0.866	0.035	0.1005	0.0024	0.41743	0.0621	0.0021	628	19	617.2	14	646	72	617	12	96
Output_1_	3_25_2C	136.6	39.4	2.458	0.06	0.2123	0.0048	0.58077	0.0839	0.0013	1259	18	1241	26	1286	31	1286	14	97
Output_1_	3_25_3A	194.2	61.4	5.32	0.14	0.327	0.0085	0.7158	0.1179	0.0017	1871	23	1823	42	1921	26	1921	13	95
Output_1_	3_25_3C	172.7	165.3	0.825	0.023	0.0971	0.0021	0.30032	0.0618	0.0014	611	13	597.2	13	649	48	597	12	92
Output_1_	3_24_2A	174.6	92.9	0.805	0.024	0.09642	0.0021	0.42162	0.0605	0.0013	599	13	593.3	12	610	48	593	13	97
Output_1_	3_24_2B	277.8	125.2	0.839	0.022	0.0986	0.0024	0.55361	0.0617	0.0011	617.8	12	605.9	14	651	38	606	13	93
Output_1_	3_24_2C	263	208	0.859	0.027	0.1013	0.0022	0.28778	0.0613	0.0015	628	15	622	13	631	55	622	13	99
Output_1_	3_24_3A	277	159.8	0.824	0.021	0.0968	0.0021	0.41632	0.0616	0.0011	609.4	12	595.4	12	649	37	595	18	92
Output_1_	3_24_3B	333.1	151.4	0.843	0.023	0.0993	0.0022	0.54576	0.0614	0.0011	619.5	13	610.4	13	645	38	610	13	95
Output_1_	3_24_4A	139.4	69.3	0.851	0.027	0.0993	0.0022	0.43856	0.0619	0.0015	623	15	610.4	13	650	52	610	15	94
Output_1_	3_24_4B	186	211.9	0.872	0.027	0.1014	0.0023	0.37699	0.0621	0.0015	635	15	622.8	13	668	53	623	14	93
Output_1_	3_23_1A	130.4	115.4	1.15	0.035	0.1262	0.0031	0.46262	0.0658	0.0015	775	16	766	18	786	47	766	13	97
Output_1_	3_23_1B	157	146.9	0.82	0.025	0.0964	0.0022	0.3612	0.0616	0.0015	607	14	593.3	13	642	51	593	12	92
Output_1_	3_23_1C	971	292.8	2.353	0.047	0.207	0.0044	0.65695	0.08223	0.00064	1228	14	1213	23	1248	15	1248	13	97
Output_1_	3_23_1D	223	238	0.951	0.027	0.1076	0.0024	0.44958	0.0638	0.0013	677	14	658.4	14	723	43	658	16	91
Output_1_	3_23_1E	142.4	69.6	0.824	0.025	0.0974	0.0022	0.2861	0.0613	0.0015	609	14	598.8	13	623	54	599	12	96
Output_1_	3_22_1A	489	254.7	0.81	0.019	0.0975	0.0021	0.54403	0.06012	0.00082	601.8	11	599.8	12	603	31	600	13	99
Output_1_	3_22_1B	464	298	0.837	0.022	0.099	0.0022	0.36339	0.0609	0.0011	616.3	12	608.6	13	633	40	609	20	96
Output_1_	3_22_1C	387.2	326.5	1.136	0.029	0.127	0.0028	0.4031	0.0644	0.0011	769	14	770.6	16	755	36	771	13	102
Output_1_	3_22_1D	415	604	0.821	0.023	0.097	0.0021	0.4306	0.0613	0.0012	607	13	596.5	12	633	44	597	13	94
Output_1_	3_22_2A	683.1	523	0.853	0.021	0.10064	0.0021	0.36577	0.0612	0.001	625.3	11	618.1	13	635	36	618	14	97
Output_1_	3_22_2B	590	327.6	2.213	0.046	0.1993	0.0042	0.48457	0.08027	0.00083	1184	14	1172.6	22	1198	20	1198	12	98
Output_1_	3_22_3A	148.2	100.9	0.817	0.035	0.0959	0.0021	0.19016	0.0616	0.0023	605	20	590.2	13	622	85	590	11	95
Output_1_	3_22_3C	1003	611	0.86	0.021	0.10186	0.0022	0.50878	0.06089	0.00089	629.3	11	625.2	13	630	33	625	13	99
Output_1_	3_20-21_1A	692	724	0.892	0.022	0.1028	0.0024	0.36438	0.0629	0.0012	646.8	12	630.6	14	697	41	631	15	90
Output_1_	3_20-21_1B	634	218.2	0.746	0.022	0.09092	0.002	0.38972	0.0594	0.0013	565	13	560.9	12	577	47	561	13	97
Output_1_	3_20-21_1C	873	404.9	0.764	0.018	0.09312	0.0019	0.53313	0.05948	0.00089	575.4	11	573.9	11	574	33	574	15	100
Output_1_	3_20-21_1D	228	222	0.868	0.029	0.10061	0.0021	0.052101	0.0625	0.0018	631	16	618.7	13	648	62	619	14	95
Output_1_	3_21_2C	142.7	351	1.044	0.027	0.1162	0.0027	0.58188	0.0649	0.001	725	13	708.7	15	761	34	709	23	93
Output_1_	3_20_2A	66.6	98.4	0.8	0.025	0.0949	0.0022	0.23351	0.0612	0.0016	595	14	584.1	13	623	60	584	39	94
Output_1_	3_20_2B	84.4	93.7	0.876	0.033	0.1019	0.0025	0.5602	0.0621	0.0017	636	18	625.5	15	665	58	626	13	94
Output_1_	3_20_2C	68.1	58.4	0.779	0.036	0.0928	0.0025	0.6349	0.0603	0.0021	581	19	574	14	606	81	574	14	95
Output_1_	3_20-21_3A	135.3	39.79	1.701	0.045	0.1691	0.0041	0.48494	0.0725	0.0013	1007	17	1007	23	992	35	1007	15	102
Output_1_	3_20-21_3B	36.46	49.5	6.34	0.18	0.3655	0.0096	0.41154	0.1254	0.0027	2022	24	2007	45	2026	39	2026	14	99
Output_1_	3_20-21_3E	142.7	100.3	0.807	0.025	0.0978	0.0024	0.55847	0.0597	0.0012	600	14	603	13	589	46	603	12	102
Output_1_	3_20-21_3F	227.8	124.2	0.829	0.024	0.0984	0.0024	0.4145	0.0608	0.0012	612	13	604.8	14	620	41	605	12	98
Output_1_	3_21_4A	186.8	240.6	0.882	0.031	0.1028	0.0025	0.27474	0.0623	0.0019	641	17	630.5	15	665	69	631	13	95
Output_1_	3_21_4B	234.4	204.2	0.922	0.024	0.1077	0.0024	0.3435	0.0622	0.0012	662.1	13	659.1	14	665	41	659	13	99
Output_1_	3_18-19_1A	333.6	276.3	0.83	0.022	0.09786	0.0021	0.47084	0.0613	0.001	612.3	12	601.8	12	643	37	602	14	94
Output_1_	3_18-19_1B	141.4	167.5	0.72	0.023	0.0878	0.0022	0.41718	0.059	0.0014	549	13	545.3	12	554	53	545	37	98
Output_1_	3_18-19_1C	168.3	137	0.828	0.023	0.0973	0.0022	0.42409	0.0615	0.0012	611.1	12	598.6	13	649	40	599	15	92
Output_1_	3_18-19_1D	170.9	56.8	0.841	0.023	0.1002	0.0023	0.40689	0.0607	0.0012	618	13	615.4	13	614	43	615	0	100
Output_1_	3_18-19_2A	152.5	111.6	0.889	0.027	0.1035	0.0023	0.58756	0.0619	0.0013	644	15	634.8	14	661	43	635	0	96
Output_1_	3_18-19_2B	70.7	23.09	4.023	0.11	0.2851	0.0067	0.47849	0.1023	0.002	1637	23	1616	34	1660	37	1660	0	97
Output_1_	3_18-19_2C	68.7	78.4	0.955	0.036	0.1081	0.0025	0.19595	0.0641	0.0022	678	19	661.5	15	700	72	662	0	95

Appendix G: Zircon U-Pb Geochronology data tables (*continued*)

Sample ID	Zircon ID	U (ppm)	Th (ppm)	Isotopic Ratio 207Pb/235U	±2SE	206Pb/238U	±2SE	Rho	207Pb/206U	±2SE	Isotopic Ages 207Pb/235U	±2SE	206Pb/238U (Age)	±2SE	206Pb/207U (Age)	±2SE	Best age	±2SE	Conc %
Output_1_	3_18-19_2D	43.4	36.5	0.844	0.034	0.1001	0.0024	0.41372	0.0611	0.0021	617	19	614.6	14	596	77	615	13	103
Output_1_	3_18-19_2E	123.6	103	0.844	0.026	0.1004	0.0023	0.30764	0.0608	0.0015	619	14	616.7	13	607	55	617	13	102
Output_1_	3_18-19_2F	114.1	90.2	0.806	0.023	0.0964	0.0021	0.30657	0.0607	0.0013	601	13	592.9	12	610	49	593	28	97
Output_1_	3_18-19_3A	119.9	80	0.83	0.03	0.0984	0.0025	0.35856	0.0609	0.0018	611	17	605.1	14	602	66	605	12	101
Output_1_	3_18-19_3C	160.3	60.1	0.844	0.023	0.1002	0.0022	0.41684	0.0607	0.0012	620.1	13	615.7	13	618	42	616	13	100
Output_1_	3_18-19_3F	156.1	73.4	0.833	0.026	0.0986	0.0023	0.51901	0.0614	0.0015	613	14	606	13	635	54	606	18	95
Output_1_	3_16-17_1A	215	359	6.47	0.16	0.3808	0.0093	0.71449	0.1226	0.0019	2045	25	2080	44	1992	28	1992	13	104
Output_1_	3_16-17_1B	229.2	137.1	0.828	0.022	0.0981	0.0021	0.41867	0.0607	0.0011	611.4	12	603.2	12	615	38	603	13	98
Output_1_	3_16-17_1C	102.5	79.8	0.818	0.024	0.0967	0.0022	0.26849	0.0608	0.0014	605	14	595.2	13	615	52	595	13	97
Output_1_	3_16-17_1D	600	574	5.013	0.11	0.322	0.0078	0.83943	0.1128	0.0011	1821	19	1799	38	1842	18	1842	24	98
Output_1_	3_16-17_2A	229.5	201.3	0.811	0.024	0.098	0.0022	0.32833	0.0598	0.0013	602	13	602.4	13	583	49	602	13	103
Output_1_	3_16-17_2B	170.1	190	0.867	0.023	0.1033	0.0023	0.16432	0.0609	0.0013	632.3	13	633.6	13	611	48	634	13	104
Output_1_	3_16-17_2C	373	451	0.838	0.02	0.0995	0.0022	0.6198	0.0612	0.001	617.4	11	611.2	13	635	35	611	14	96
Output_1_	3_16-17_2D	238	111.8	2.777	0.064	0.2283	0.005	0.5759	0.0881	0.0011	1348	17	1325	26	1378	24	1378	24	96
Output_1_	3_16-17_3A	177.1	111.9	0.834	0.025	0.0986	0.0022	0.32326	0.0608	0.0015	615	14	606	13	627	50	606	21	97
Output_1_	3_16-17_3C	279	191.4	0.802	0.02	0.0959	0.0022	0.49442	0.0608	0.0011	598.3	12	590.3	13	619	38	590	13	95
Output_1_	3_16-17_3D	87.8	60.7	0.857	0.032	0.1009	0.0025	0.32857	0.0613	0.0019	625	17	619.6	14	622	67	620	15	100
Output_1_	3_16-17_4A	409.1	58.6	3.613	0.084	0.2707	0.0066	0.67922	0.0967	0.0012	1552	19	1544	33	1558	24	1558	17	99
Output_1_	3_16-17_4B	280.2	93.4	2.377	0.051	0.2085	0.0045	0.65995	0.08243	0.00089	1234.6	15	1221	24	1251	21	1251	14	98
Output_1_	3_16-17_4E	130	131	0.791	0.025	0.0937	0.0021	0.34535	0.0607	0.0015	590	14	577.6	13	609	55	578	12	95
Output_1_	3_16-17_4F	77.8	53.5	0.833	0.031	0.0982	0.0025	0.35831	0.0617	0.002	612	17	603.4	15	622	69	603	13	97
Output_1_	3_14-15_1A	477	285	2.278	0.046	0.2004	0.0043	0.61294	0.08229	0.0007	1204.6	14	1177	23	1251	17	1251	13	94
Output_1_	3_14-15_1B	69.4	81.2	0.915	0.036	0.1065	0.0024	0.29414	0.0618	0.0021	655	19	652.4	14	631	75	652	13	103
Output_1_	3_14-15_1C	199.4	143.7	0.858	0.023	0.1012	0.0022	0.46958	0.0613	0.0012	629	13	622.5	12	633	41	623	12	98
Output_1_	3_14-15_1D	106.1	89.7	0.822	0.028	0.0972	0.0023	0.18584	0.0608	0.0017	608	16	598	13	624	64	598	14	96
Output_1_	3_14-15_2A	198.8	403	0.729	0.022	0.0893	0.0022	0.49246	0.0598	0.0015	555	13	551.3	13	577	54	551	12	96
Output_1_	3_14-15_2B	240.8	714	0.8	0.023	0.0952	0.0022	0.49778	0.061	0.0012	596	13	586.4	13	625	43	586	14	94
Output_1_	3_14-15_2C	200.9	214	0.745	0.024	0.0902	0.0021	0.50486	0.0598	0.0014	564	14	556.4	12	578	51	556	17	96
Output_1_	3_14-15_2D	559	307	0.862	0.021	0.1011	0.0023	0.38301	0.0617	0.0011	630.6	11	620.8	14	653	39	621	14	95
Output_1_	3_14-15_3A	264	538	0.735	0.019	0.0891	0.002	0.39879	0.0596	0.001	558.5	11	550	12	576	39	550	13	95
Output_1_	3_14-15_3B	183.5	208	0.794	0.024	0.0944	0.0023	0.54515	0.0613	0.0014	592	13	581.6	14	632	50	582	12	92
Output_1_	3_14-15_3C	171.8	101.4	1.116	0.031	0.1253	0.0029	0.40297	0.0645	0.0012	761	16	760.9	17	750	42	761	12	101
Output_1_	3_13-31_1A	59.5	15.73	0.824	0.033	0.0982	0.0024	0.25872	0.0605	0.0021	610	19	603.9	14	591	81	604	13	102
Output_1_	3_13-31_1B	315.4	200.3	0.833	0.019	0.0998	0.0022	0.5146	0.06032	0.00091	614.7	11	613	13	608	32	613	13	101
Output_1_	3_13-31_1C	308	223	0.746	0.021	0.0894	0.0021	0.56153	0.0604	0.0011	564.5	12	552	12	603	41	552	13	92
Output_1_	3_13-31_1D	166.7	102.9	0.803	0.026	0.0957	0.0021	0.46091	0.0611	0.0015	597	14	589	12	617	54	589	13	95
Output_1_	3_13-31_2A	132.6	194	0.751	0.027	0.0899	0.0022	0.52388	0.0602	0.0016	566	16	554.7	13	581	58	555	13	95
Output_1_	3_13-31_2B	102.3	61.6	0.852	0.031	0.0983	0.0023	0.27082	0.0624	0.0019	622	17	604	13	669	67	604	14	90
Output_1_	3_13-31_2C	481	194.6	0.87	0.018	0.10248	0.0022	0.41683	0.06142	0.00067	635.2	9.9	628.9	13	648	23	629	14	97
Output_1_	3_13-31_2D	148.5	57.5	0.872	0.025	0.1022	0.0023	0.37484	0.0617	0.0013	635	14	627.4	13	649	44	627	13	97
Output_1_	3_13-31_2E	209.5	146.8	0.845	0.022	0.1003	0.0023	0.32817	0.061	0.0011	620.3	12	616.2	13	625	40	616	14	99
Output_1_	3_13-31_3A	237.2	209.8	0.852	0.026	0.1008	0.0024	0.2659	0.0616	0.0017	627	15	618.8	14	641	57	619	13	97
Output_1_	3_13-31_3B	308.5	186.4	0.815	0.021	0.0967	0.0024	0.3922	0.0605	0.0011	604.2	11	595	14	614	41	595	13	97
Output_1_	3_13-31_3C	152.4	58.2	0.858	0.025	0.1026	0.0023	0.36215	0.0605	0.0013	629	13	629.6	13	605	49	630	22	104
Output_1_	3_31_3A	111.6	84.4	0.862	0.026	0.1011	0.0024	0.34255	0.0617	0.0014	629	14	622.1	14	645	51	622	12	96
Output_1_	3_31_3B	298	224.5	0.734	0.021	0.0889	0.0022	0.56986	0.0595	0.0011	557.5	12	549	13	571	42	549	15	96
Output_1_	3_31_3C	193.1	200.6	0.805	0.022	0.0967	0.0022	0.55007	0.0605	0.0011	598.3	12	594.8	13	613	38	595	14	97
Output_1_	3_32-33_1A	253.6	98.3	2.348	0.054	0.209	0.005	0.67837	0.08137	0.00094	1227	16	1223	27	1225	22	1225	40	100
Output_1_	3_32-33_1B	140.2	238.8	0.746	0.022	0.0894	0.002	0.35695	0.0603	0.0014	565	13	551.8	12	599	51	552	34	92
Output_1_	3_32-33_1D	51.15	42.4	0.852	0.035	0.0988	0.0025	0.38089	0.0617	0.0021	623	19	607	15	640	79	607	14	95
Output_1_	3_32-33_2A	292.2	180.8	0.802	0.021	0.0967	0.0023	0.47979	0.0601	0.0011	597.1	12	594.9	14	595	38	595	14	100
Output_1_	3_32-33_2B	81	23.42	2.202	0.061	0.1969	0.0047	0.3221	0.0812	0.0017	1179	19	1158	25	1212	40	1212	12	96
Output_1_	3_32-33_2D	81.8	67.4	2.467	0.075	0.2141	0.0056	0.65167	0.0823	0.0015	1262	21	1255	27	1251	34	1251	13	100
Output_1_	3_32-33_3B	165.9	186.3	0.734	0.024	0.0901	0.0024	0.31757	0.0591	0.0016	557	14	556	14	546	59	556	14	102
Output_1_	3_32-33_3C	62	48.5	0.813	0.032	0.0974	0.0024	0.31044	0.0607	0.0021	603	18	598.8	14	578	73	599	13	104
Output_1_	3_34-35_1A	223.9	299.1	0.741	0.021	0.0891	0.0021	0.53953	0.0603	0.0012	561.7	12	549.9	12	595	43	550	22	92
Output_1_	3_34-35_1C	101.7	57.9	0.845	0.027	0.0996	0.0022	0.18719	0.0614	0.0016	620	15	611.8	13	625	56	612	15	98
Output_1_	3_34-35_1D	152.3	152	0.833	0.028	0.0983	0.0023	0.29513	0.0614	0.0018	613	15	604.2	14	619	62	604	13	98
Output_1_	3_34-35_2A	256.1	179.9	0.841	0.024	0.0998	0.0022	0.39881	0.0606	0.0012	618	13	613.2	13	613	45	613	12	100
Output_1_	3_34-35_2C	267	215.3	3.14	0.073	0.2428	0.0055	0.74964	0.0932	0.0011	1443	19	1401	29	1487	22	1487	14	94
Output_1_	3_34-35_3A	82.8	97.4	0.838	0.032	0.098	0.0028	0.50801	0.0625	0.002	615	18	604	15	650	71	604	14	93
Output_1_	3_34-35_3B	231	222	0.86	0.024	0.1023	0.0023	0.34473	0.0601	0.0012	628	13	628	13	608	45	628	12	103
Output_1_	3_34_4A	174	105.7	0.759	0.021	0.0923	0.0021	0.3262	0.0593	0.0013	571.8	12	568.8	12	556	49	569	13	102
Output_1_	3_34_4B	148	74.9	0.824	0.025	0.0977	0.0023	0.43969	0.0608	0.0013	609	14	600.6	14	619	49	601	14	97
Output_1_	3_26_1A	225.7	197.3	0.818	0.023	0.0967	0.0023	0.52869	0.0611	0.0013	607	14	595.1	14	629	44	595	16	95
Output_1_	3_26_1D	364.1	187.7	0.757	0.018	0.09126	0.002	0.52328	0.06006	0.00091	571.8	11	562.9	12	595	33	563	0	95
Output_1_	3_26_2B	185.4	87.9	0.823	0.022	0.0978	0.0022	0.34607	0.0608	0.0011	609.4	12	601.6	13	620	42	602	0	97
Output_1_	3_26_2C	235	157.8	0.804	0.021	0.0962	0.0023	0.40749	0.0604	0.0012	598.2	12	591.9	14	604	41	592	0	98
Output_1_	3_26_2D	128.5	57.6	0.801	0.027	0.0971	0.0027	0.13565	0.0598	0.002	596	16	597	16	589	78	597	0	101

Appendix G: Zircon U-Pb Geochronology data tables (*continued*)

						Isotopic Ratio							Isotopic Ages					
Sample ID	Zircon ID	U (ppm)	Th (ppm)	207Pb/ 235U	±2SE	206Pb/ 238U	±2SE	Rho	207Pb/ 206U	±2SE	207Pb/ 235U	±2SE	206Pb/ 238U (Age)	±2SE	206Pb/ 207U (Age)	±2SE	Best age	±2SE	Conc %
Output_1_	3_26_3A	27.9	32.2	0.908	0.05	0.1048	0.0029	0.46376	0.0623	0.0031	649	28	642	17	620	110	642	13	104
Output_1_	3_26_3B	203.2	65.6	2.365	0.057	0.2092	0.0049	0.6748	0.082	0.0011	1232	18	1224	26	1248	27	1248	18	98
Output_1_	3_11-12_1A	191.4	81.2	0.826	0.024	0.0968	0.0025	0.50514	0.0614	0.0011	610	13	595	15	647	40	595	17	92
Output_1_	3_11-12_1B	252	119.9	2.978	0.079	0.2471	0.0068	0.79723	0.0872	0.0012	1399	20	1422	35	1359	26	1359	15	105
Output_1_	3_11-12_1C	265	173.8	0.874	0.022	0.1026	0.0022	0.37579	0.06175	0.00095	637.9	12	629.8	13	664	35	630	16	95
Output_1_	3_11-12_1D	281.5	356	0.839	0.027	0.0984	0.0031	0.56521	0.0624	0.0018	621	14	605	18	670	59	605	12	90
Output_1_	3_11-12_1E	77.2	101.2	0.838	0.035	0.0997	0.0029	0.28239	0.0614	0.0024	617	20	612	17	603	84	612	14	101
Output_1_	3_11-12_2A	159.4	78.6	0.805	0.026	0.0968	0.0026	0.54753	0.0604	0.0014	601	15	595	15	599	51	595	14	99
Output_1_	3_11-12_2B	293	178.1	0.878	0.026	0.1029	0.0027	0.45191	0.0614	0.0014	638	14	631	16	634	49	631	25	100
Output_1_	3_11-12_2C	205.5	231	0.741	0.025	0.0903	0.0021	0.36545	0.0595	0.0016	563	14	557.5	12	559	60	558	13	100
Output_1_	3_11-12_2D	357.5	250.8	0.811	0.023	0.0963	0.0023	0.45087	0.0606	0.0013	602	13	592.6	14	619	46	593	13	96
Output_1_	3_11-12_3A	390	254.6	0.811	0.02	0.097	0.0023	0.52084	0.06072	0.00097	603.6	12	596.6	14	619	34	597	15	96
Output_1_	3_11-12_3B	306.6	147.4	2.293	0.055	0.2035	0.005	0.71621	0.0814	0.0011	1208	17	1193	27	1224	25	1224	14	97
Output_1_	3_11-12_3C	128.7	197.6	0.753	0.029	0.0898	0.0023	0.16871	0.0605	0.0021	567	17	555.4	13	578	72	555	33	96
Output_1_	3_11-12_3D	434	843	0.757	0.022	0.0911	0.0022	0.54059	0.0608	0.0012	571	13	562.1	13	624	46	562	12	90
Output_1_	3_9-10_1B	75.5	42.3	0.792	0.033	0.0945	0.0025	0.24151	0.0611	0.0023	588	19	582	15	580	82	582	13	100
Output_1_	3_9-10_1D	112.8	68.6	0.85	0.028	0.1003	0.0025	0.38312	0.0614	0.0017	622	16	616.2	14	619	61	616	13	100
Output_1_	3_9-10_1E	165.6	54.7	3.546	0.09	0.2686	0.0064	0.50558	0.0957	0.0017	1536	20	1533	33	1536	33	1536	17	100
Output_1_	3_9-10_2A	130.8	97.4	0.788	0.024	0.0949	0.0021	0.1374	0.06	0.0015	588	13	584.5	12	579	56	585	12	101
Output_1_	3_9-10_2B	185.6	153.7	0.832	0.024	0.098	0.0022	0.46394	0.0615	0.0013	613	14	602.7	13	640	47	603	13	94
Output_1_	3_9-10_2C	146.3	100.6	0.861	0.025	0.1004	0.0023	0.25962	0.0617	0.0014	629	13	616.7	13	640	48	617	13	96
Output_1_	3_9-10_2D	127.5	211	0.875	0.035	0.1031	0.0028	0.53133	0.0612	0.0018	636	19	633	17	622	67	633	12	102
Output_1_	3_9-10_2E	238.8	182.6	0.75	0.023	0.0904	0.0021	0.000481	0.06	0.0015	567	13	557.7	12	585	54	558	15	95
Output_1_	3_9-10_2F	340.5	428	0.747	0.021	0.091	0.0022	0.24709	0.0594	0.0013	565.5	12	561.6	13	565	49	562	16	99
Output_1_	3_9-10_3A	242	183.2	0.826	0.02	0.0972	0.0022	0.35665	0.0612	0.0011	610.8	11	597.9	13	645	37	598	15	93
Output_1_	3_9-10_3C	758	1516	0.747	0.02	0.0909	0.0021	0.62255	0.05976	0.00095	566	12	561	12	587	35	561	15	96
Output_1_	3_9-10_3D	222.8	205.9	0.866	0.033	0.1006	0.0025	0.57263	0.0618	0.0017	631	18	617.7	15	649	60	618	13	95
Output_1_	3_9-10_3E	478	469	0.86	0.027	0.1002	0.0028	0.61636	0.062	0.0013	629	15	615	16	662	44	615	14	93
Output_1_	3_9-10_4C	241	262.2	0.843	0.041	0.0989	0.0026	0.47751	0.0617	0.0024	617	22	608	15	648	90	608	19	94
Output_1_	3_7-8_1A	146.4	175.7	0.874	0.041	0.1029	0.0026	0.36725	0.0615	0.0025	635	22	631	15	627	89	631	14	101
Output_1_	3_7-8_1B	161.1	247.5	0.751	0.025	0.0893	0.0022	0.38853	0.0603	0.0016	568	14	551.5	13	599	56	552	15	92
Output_1_	3_7-8_1C	350	192	0.915	0.023	0.1054	0.0024	0.34092	0.0624	0.001	658.9	12	645.9	14	679	35	646	13	95
Output_1_	3_7-8_1E	384.7	83	2.329	0.048	0.2059	0.0045	0.64825	0.08194	0.00078	1220.4	15	1206	24	1240	19	1240	13	97
Output_1_	3_7-8_1F	77.5	62.82	0.858	0.028	0.1026	0.0024	0.32863	0.0608	0.0015	627	16	629.4	14	621	57	629	15	101
Output_1_	3_7-8_1H	69.2	98.7	0.876	0.032	0.1023	0.0025	0.32534	0.0618	0.0018	636	17	627.7	15	634	64	628	14	99
Output_1_	3_7-8_2A	284.3	182.3	0.837	0.023	0.0986	0.0022	0.49389	0.0613	0.0011	616.8	13	606.3	13	638	40	606	27	95
Output_1_	3_7-8_2B	75.1	54.7	0.817	0.026	0.0964	0.0022	0.18076	0.0615	0.0017	604	14	593	13	622	59	593	12	95
Output_1_	3_7-8_2C	100.8	100.6	0.861	0.041	0.0993	0.0025	0.2953	0.0628	0.0026	628	22	610.4	15	676	88	610	12	90
Output_1_	3_7-8_2E	108.8	63.7	0.892	0.027	0.1053	0.0024	0.28793	0.0614	0.0015	646	14	645.3	14	632	52	645	12	102
Output_1_	3_7-8_2F	213.3	178	1.828	0.042	0.1779	0.0038	0.49186	0.0743	0.001	1054.6	15	1055.6	21	1043	27	1043	12	101
Output_1_	3_7-8_3A	222.7	199.5	0.849	0.02	0.10029	0.0021	0.41895	0.06137	0.00098	623.3	11	616.1	12	645	33	616	12	96
Output_1_	3_7-8_3B	328.3	171.3	0.748	0.022	0.09	0.002	0.39347	0.0601	0.0013	566	13	555.5	12	594	46	556	14	94
Output_1_	3_6_1B	231.1	236.9	0.758	0.025	0.0906	0.0021	0.30992	0.0603	0.0016	571	14	559.3	12	593	58	559	12	94
Output_1_	3_6_1C	372	199.3	0.742	0.019	0.09027	0.0019	0.37118	0.0595	0.001	562.7	11	557.1	12	570	38	557	14	98
Output_1_	3_6_2A	338	211	0.801	0.02	0.09564	0.002	0.41539	0.0605	0.001	596.2	11	588.7	12	604	37	589	14	97
Output_1_	3_6_2B	214	122	0.847	0.026	0.1	0.0023	0.11107	0.0613	0.0016	621	14	614.2	14	631	57	614	13	97
Output_1_	3_6_2C	200.8	149.2	0.808	0.024	0.0965	0.0021	0.132	0.0603	0.0015	600	13	593.8	12	600	55	594	28	99
Output_1_	3_6_3	290.3	344.6	0.816	0.024	0.0958	0.0023	0.3562	0.0616	0.0015	604	14	589.6	14	651	48	590	76	91
Output_1_	3_6_4A	200.4	255.6	0.87	0.036	0.1001	0.0024	0.24133	0.0629	0.0024	633	20	615.1	14	678	83	615	13	91
Output_1_	3_6_4B	360	228.4	0.839	0.022	0.0986	0.0022	0.39651	0.0615	0.0011	617.7	12	606.4	13	641	40	606	12	95
Output_1_	3_5_1A	289	122	2.32	0.055	0.2069	0.0046	0.52188	0.081	0.0011	1218	16	1212	24	1212	28	1212	39	100
Output_1_	3_5_1B	313	165	2.05	0.11	0.1918	0.0076	0.082984	0.0784	0.0028	1139	31	1130	41	1142	76	1142	21	99
Output_1_	3_5_2A	228.5	482	0.849	0.023	0.09995	0.0021	0.39633	0.0614	0.0012	623	13	614	13	639	43	614	12	96
Output_1_	3_5_2B	296.1	143.1	0.829	0.02	0.09847	0.0021	0.39385	0.06106	0.00097	611.9	11	605.3	12	628	35	605	14	96
Output_1_	3_3-4_1A	61.9	36.31	3.291	0.098	0.2501	0.0058	0.48104	0.0946	0.0019	1475	23	1439	30	1522	39	1522	25	95
Output_1_	3_3-4_1B	588	183.4	2.189	0.051	0.1965	0.0047	0.68804	0.08111	0.00088	1177	16	1156	25	1222	21	1222	12	95
Output_1_	3_3-4_1C	170.4	267	0.745	0.022	0.0899	0.002	0.33041	0.06	0.0013	564	12	554.9	12	580	48	555	14	96
Output_1_	3_3-4_1F	38.6	24.59	0.88	0.041	0.1015	0.0024	-0.00636	0.0629	0.0029	638	23	623.1	14	640	100	623	13	97
Output_1_	3_3-4_2A	174.3	175.2	3.553	0.082	0.2624	0.0056	0.51567	0.0976	0.0013	1537	18	1502	29	1574	25	1574	27	95
Output_1_	3_3-4_2C	356	314	0.801	0.02	0.09549	0.002	0.28777	0.06055	0.00094	596.9	11	587.9	12	614	34	588	15	96
Output_1_	3_3-4_2E	184.2	145.5	0.895	0.025	0.1041	0.0023	0.49743	0.0623	0.0011	647	13	638.2	14	668	39	638	43	96
Output_1_	3_3-4_2D	153.9	150.7	0.816	0.025	0.0957	0.0021	0.16749	0.0616	0.0014	604	14	589.2	13	635	53	589	12	93
Output_1_	3_3-4_2F	152.5	123.3	4.39	0.11	0.2982	0.007	0.6132	0.1063	0.0015	1711	22	1682	35	1736	27	1736	14	97
Output_1_	3_3-4_3A	93.1	81.1	0.955	0.037	0.1085	0.0026	0.26267	0.0636	0.0021	678	19	663.8	15	695	71	664	12	96
Output_1_	3_3-4_3B	222.4	75	2.551	0.079	0.2146	0.0055	0.542	0.0859	0.0019	1285	23	1253	29	1331	43	1331	13	94
Output_1_	3_3-4_3C	102.9	50.26	0.743	0.027	0.0906	0.002	0.40911	0.0589	0.0016	561	15	559.1	12	534	62	559	13	105
Output_1_	3_1-2_1D	45.9	41	0.84	0.037	0.0995	0.0024	0.009804	0.0612	0.0026	614	21	611.2	14	585	95	611	13	104
Output_1_	3_1-2_1F	145	77.1	0.781	0.023	0.0946	0.0021	0.16476	0.0595	0.0015	585	13	582.9	12	561	56	583	13	104
Output_1_	3_1-2_1E	308.3	170.5	0.739	0.024	0.0893	0.0021	0.46165	0.06	0.0015	561	14	551.4	13	601	51	551	14	92
Output_1_	3_1-2_1A	291	194.7	0.846	0.023	0.0997	0.0022	0.4916	0.0616	0.0011	621	13	612.5	13	653	39	613	13	94
Output_1_	3_1-2_1B	205.4	124.2	0.81	0.025	0.0969	0.0022	0.33441	0.06	0.0014	601	14	596.2	13	598	54	596	12	100
Output_1_	3_1-2_2B	328	254.3	0.869	0.022	0.1021	0.0023	0.52048	0.0614	0.001	634.5	12	626.4	13	643	35	626	13	97
Output_1_	3_1-2_2C	64.3	42.3	0.856	0.031	0.0992	0.0023	0.10889	0.0621	0.0021	625	17	609.8	14	652	72	610	14	94
Output_1_	3_1-2_3A	270.9	117.4	0.819	0.026	0.0967	0.0022	0.43551	0.0613	0.0015	607	15	595.2	13	641	52	595	13	93
Output_1_	3_1-2_3B	147	227.5	0.75	0.023	0.09064	0.002	0.32029	0.0599	0.0014	566	13	559.2	12	571	53	559	24	98
Output_1_	3_1-2_3C	94.3	80.2	0.815	0.031	0.0949	0.0022	0.29539	0.0619	0.0021	603	17	584.5	13	638	71	585	13	92
Output_1_	3_1-2_3D	109.2	51.3	0.829	0.028	0.0974	0.0023	0.17227	0.0616	0.0018	611	15	599.3	14	638	63	599	15	94
Output_1_	3_27-28_1A	251.2	139.1	0.831	0.021	0.098	0.0022	0.51047	0.06129	0.00094	613	11	602.8	13	638	33	603	13	94
Output_1_	3_27-28_1C	219.9	69.2	2.366	0.051	0.2072	0.0045	0.43053	0.08278	0.00099	1231.3	15	1214	24	1259	24	1259	13	96
Output_1_	3_29-30_2A	128.7	164.3	0.869	0.028	0.1022	0.0022	0.4163	0.0614	0.0014	632	15	626.9	13	633	51	627	0	99
Output_1_	3_29-30_2B	143.7	139	0.754	0.032	0.0907	0.0025	0.3109	0.0604	0.0023	569	19	560	15	592	87	560	0	95
Output_1_	3_29-30_3A	567	364.4	0.822	0.022	0.0976	0.0022	0.60772	0.06086	0.0009	608.7	12	600.6	13	628	32	601	0	96
Output_1_	3_29-30_4D	133.1	68.7	0.813	0.024	0.0977	0.0022	0.30933	0.06	0.0014	602	13	601.9	13	587	48	602	0	103

Sample HC-St. John's (resembling MPF 2) *47.596720, -52.727518*

							Isotopic ratio						*Isotopic ages*						
Sample ID	**Spot name**	**Approx. U (ppm)**	**Approx. Th (ppm)**	**$^{207}Pb/^{206}Pb$**	**±2SE**	**$^{207}Pb/^{235}U$**	**±2SE**	**$^{206}Pb/^{238}U$**	**±2SE**	**Rho**	**$^{207}Pb/^{235}U$**	**±2SE**	**$^{206}Pb/^{238}U$**	**±2SE**	**$^{207}Pb/^{206}Pb$**	**±2SE**	**Conc. And Disc %**	**Best age**	**±2SE**
Output_1_8		200.3	178.1	0.06	0.002	0.728	0.05	0.088	0.005	0.423	555.1	29	544.2	27	608	51	89.51	544.2	27
Output_1_11		257.6	273.1	0.061	0.001	0.745	0.051	0.09	0.005	0.33	564.7	30	553.5	28	621	53	89.13	553.5	28
Output_1_7		224.2	270.7	0.062	0.001	0.769	0.053	0.091	0.005	0.473	578.2	30	559.5	28	652	50	85.81	559.5	28
Output_1_5		116.5	59.4	0.062	0.002	0.772	0.055	0.091	0.005	0.394	580	31	559.7	28	664	59	84.29	559.7	28
Output_1_2		148	118	0.06	0.001	0.752	0.052	0.092	0.005	0.455	568.2	30	565.8	28	576	53	98.23	565.8	28
Output_1_9		144	111	0.06	0.002	0.76	0.053	0.092	0.005	0.377	572	31	566.9	28	602	62	94.17	566.9	28
Output_1_6		76	51.3	0.06	0.002	0.766	0.055	0.093	0.005	0.417	577	32	572.4	29	590	65	97.02	572.4	29
Output_1_12		130	84.3	0.062	0.002	0.803	0.056	0.095	0.005	0.406	597	32	583.5	29	655	57	89.08	583.5	29
Output_1_1		27.5	16	0.06	0.003	0.786	0.064	0.095	0.005	0.092	583	37	585.1	30	550	110	106.4	585.1	30
Output_1_10		133.6	133.3	0.063	0.002	0.814	0.059	0.095	0.005	0.336	603	33	585.9	29	678	66	86.42	585.9	29
Output_1_3		123.6	93.5	0.061	0.002	0.825	0.057	0.098	0.005	0.432	611.1	31	599.4	30	639	54	93.8	599.4	30
Output_1_4		29.5	12.29	0.074	0.003	1.777	0.13	0.175	0.009	0.26	1037	49	1039	51	1039	66	100	1039	66

Appendix H: SEM-CL images of zircon grains

(HC-ER, MPF 2)

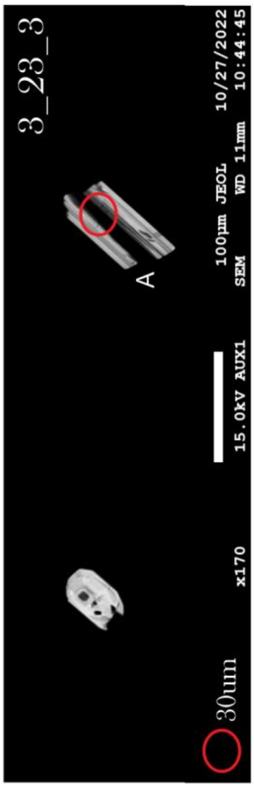

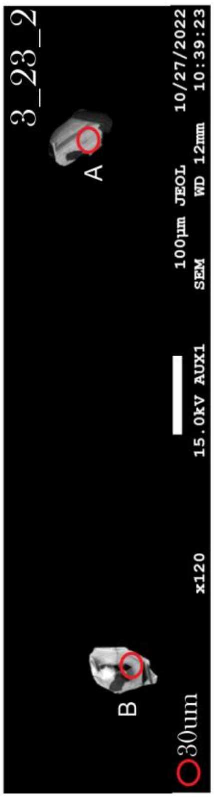

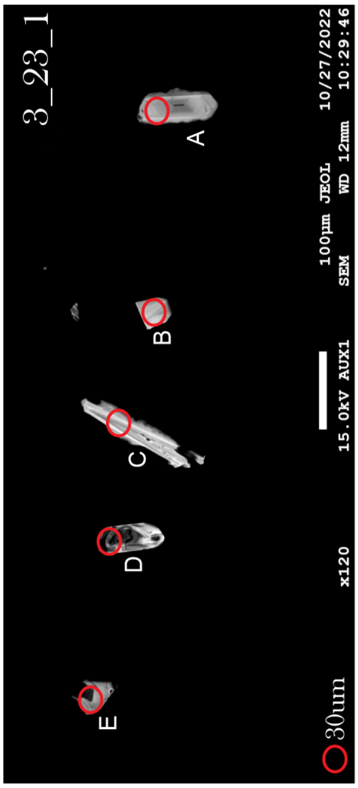

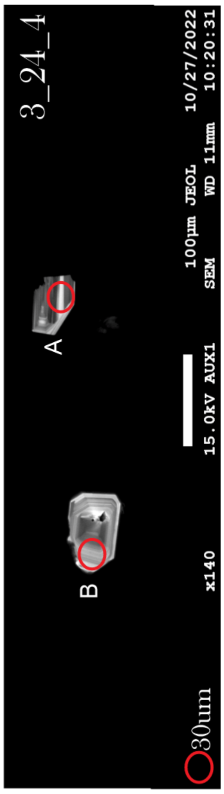

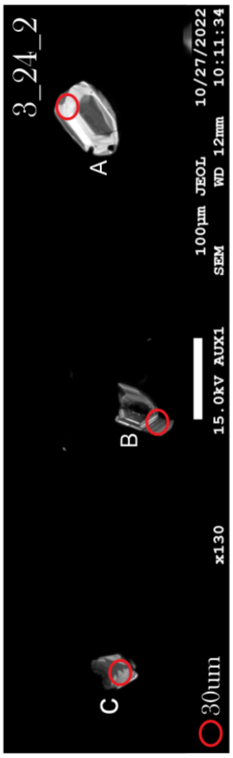

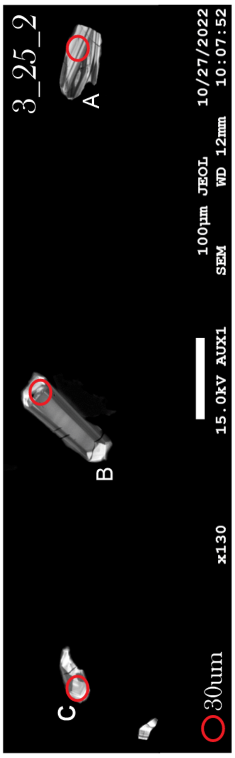

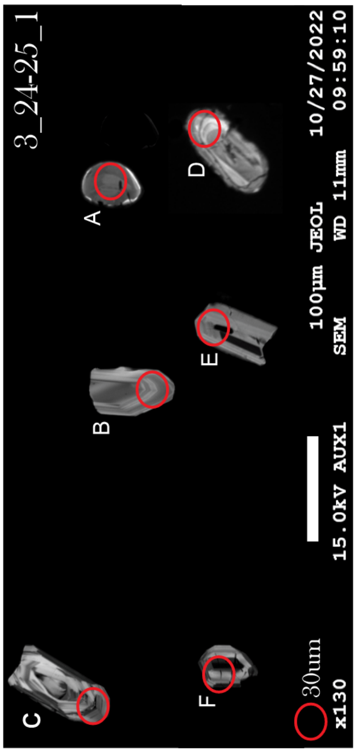

Appendix G: SEM-CL images of zircon grains *(HC-ER, MPF 2)* **(continued)**

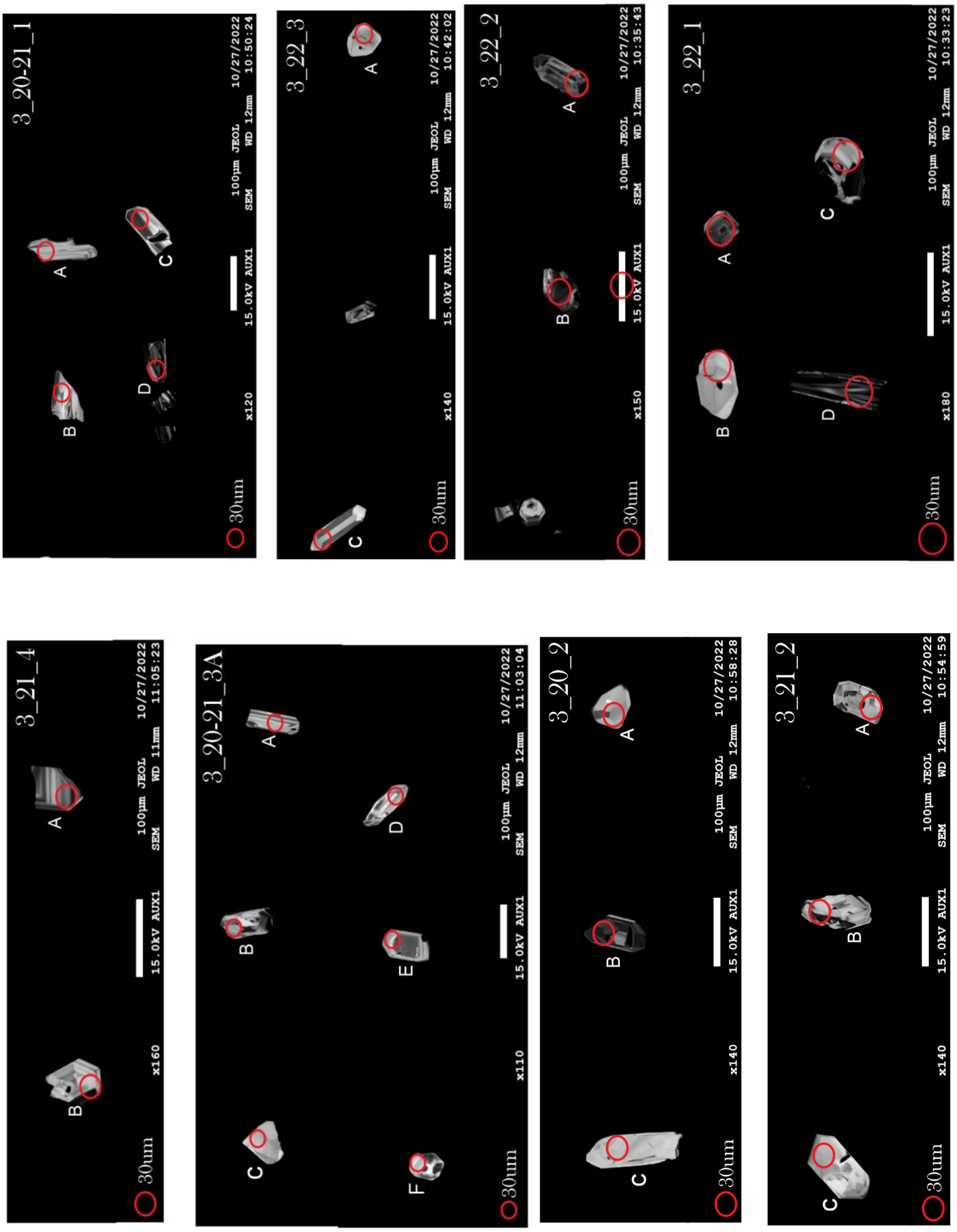

Appendix H: SEM-CL images of zircon grains (*HC-ER, MPF 2)* (continued)

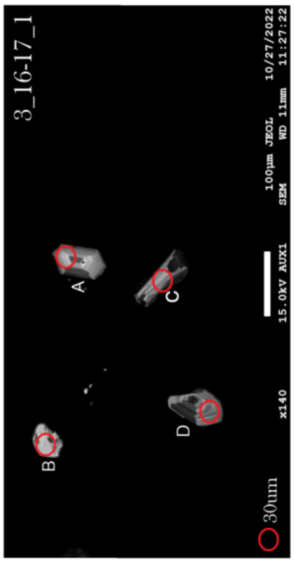

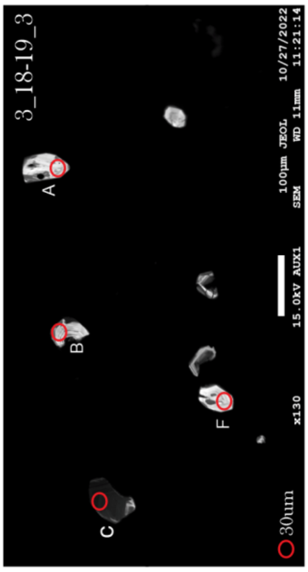

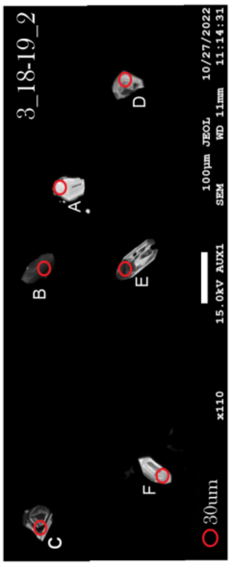

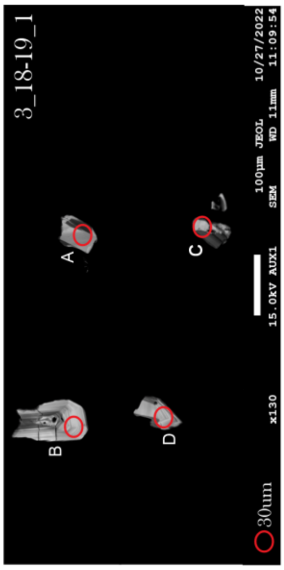

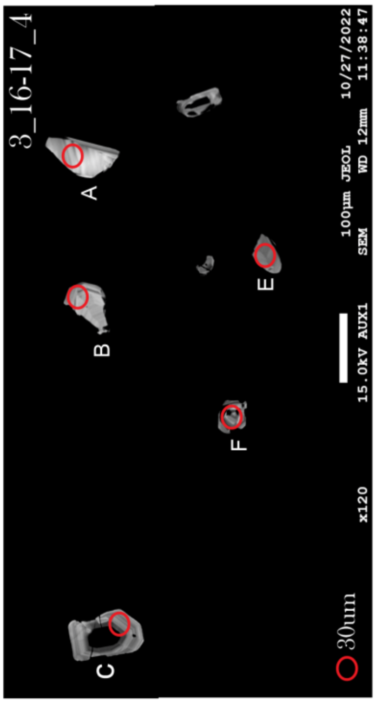

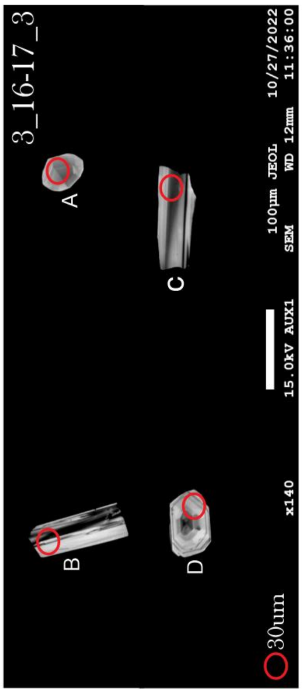

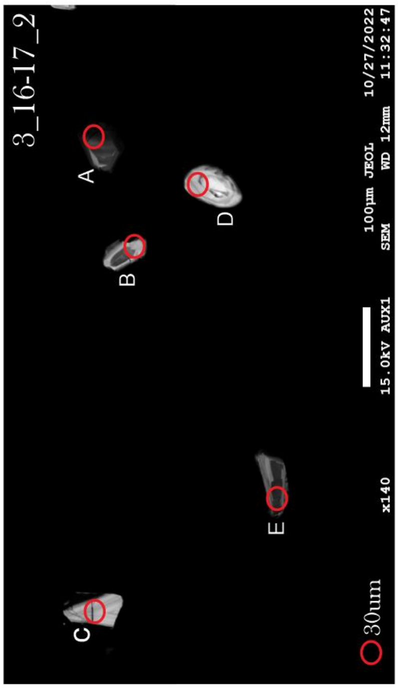

Appendix H: SEM-CL images of zircon grains *(MC-SB, MPF 1)*

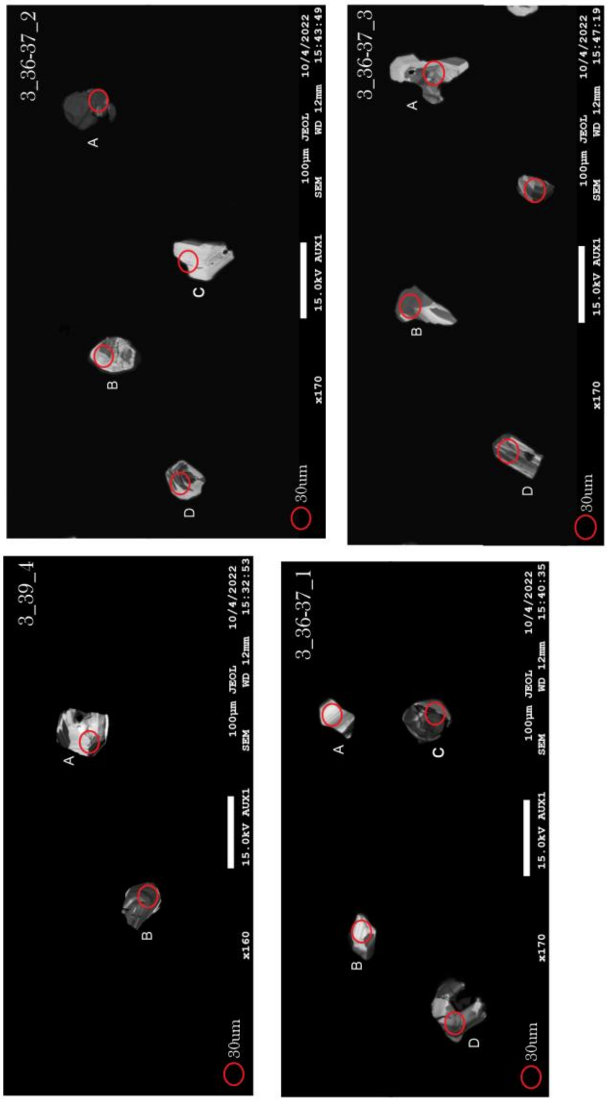

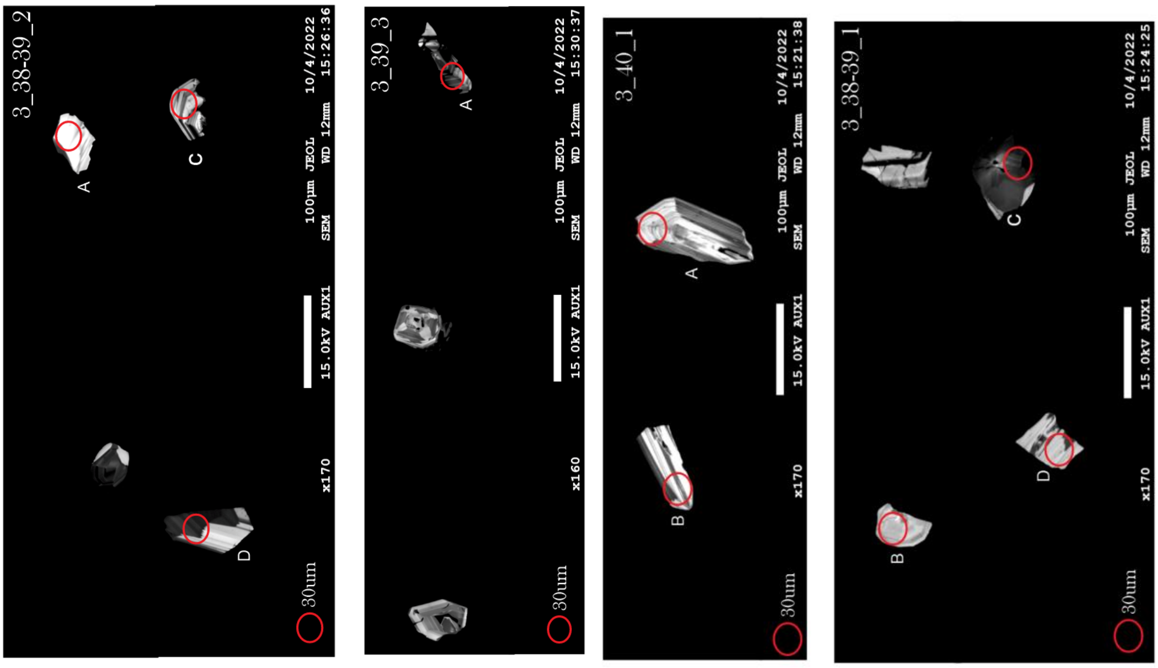
3_38-39_2
A
C
D
30um
x170
15.0kV AUX1
100µm JEOL
SEM WD 12mm
10/4/2022
15:26:36
3_39_3
A
30um
x160
15.0kV AUX1
100µm JEOL
SEM WD 12mm
10/4/2022
15:30:37
3_40_1
A
B
30um
x170
15.0kV AUX1
100µm JEOL
SEM WD 12mm
10/4/2022
15:21:38
3_38-39_1
B
C
D
30um
x170
15.0kV AUX1
100µm JEOL
SEM WD 12mm
10/4/2022
15:24:25

Appendix H: SEM-CL images of zircon grains *(MC-SB, MPF 1)* **(continued)**

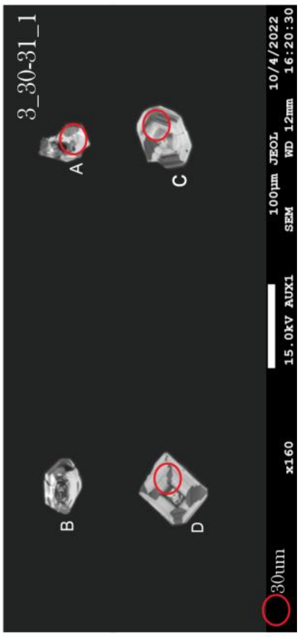

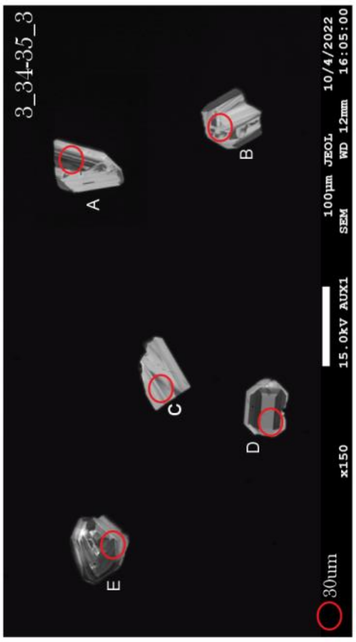

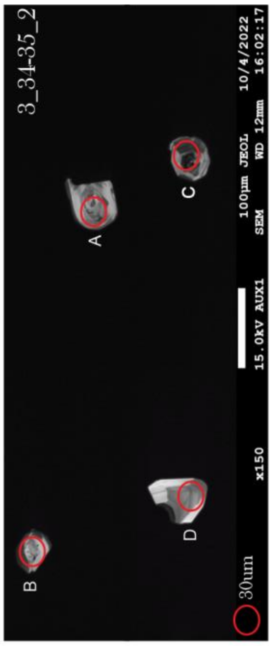

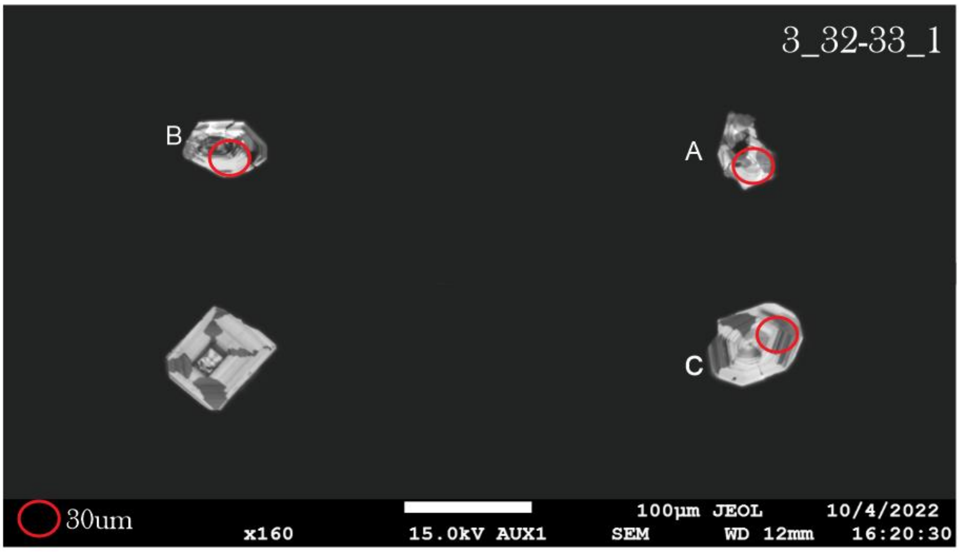

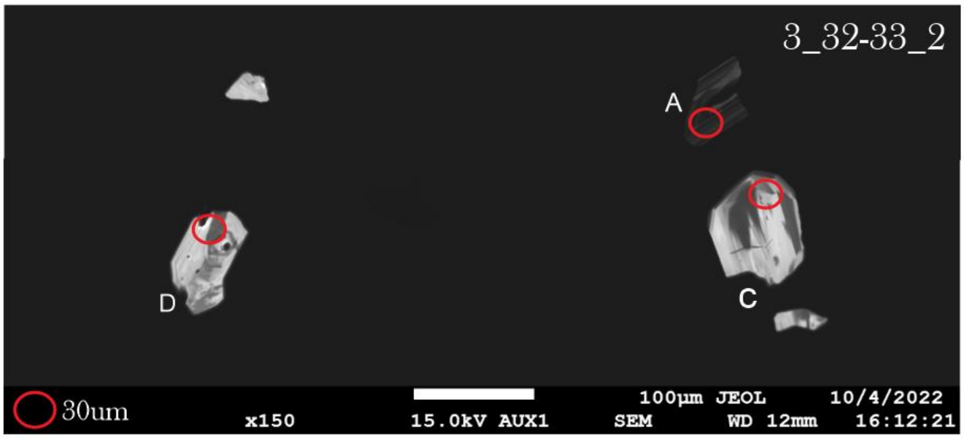

Appendix H: SEM-CL images of zircon grains *(MC-SB, MPF 1)* **(continued)**

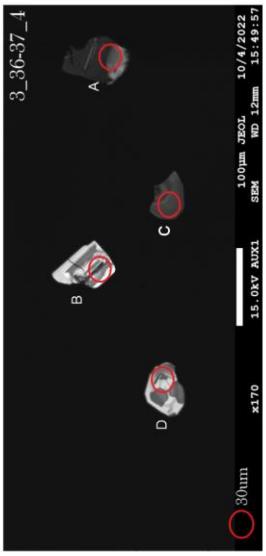

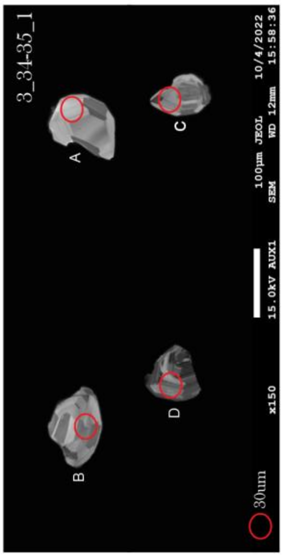

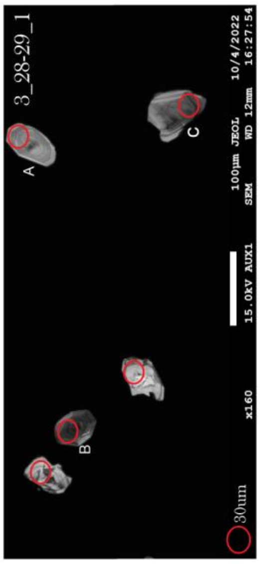

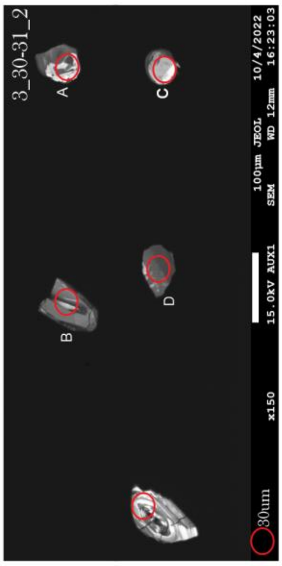

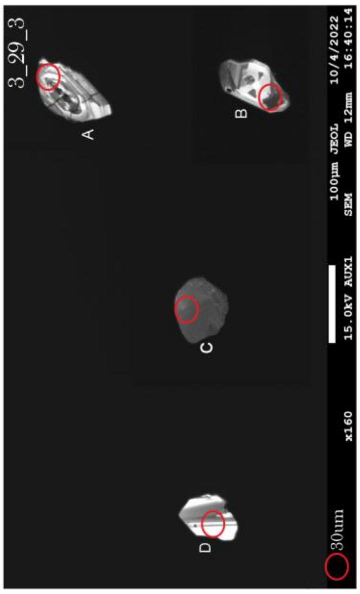

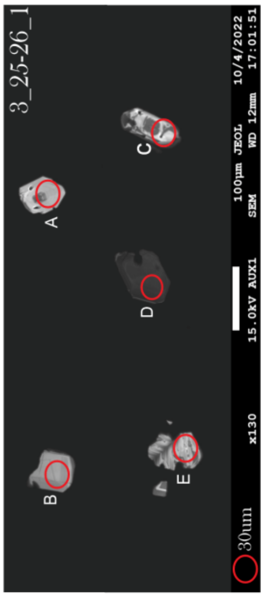

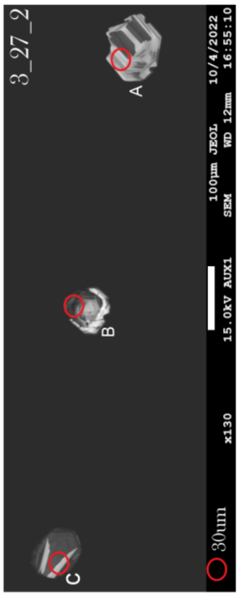

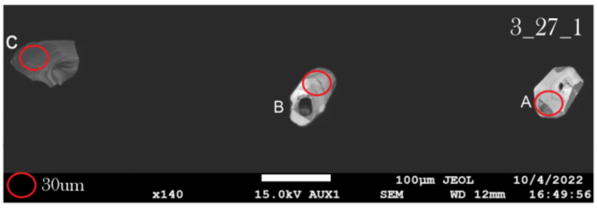

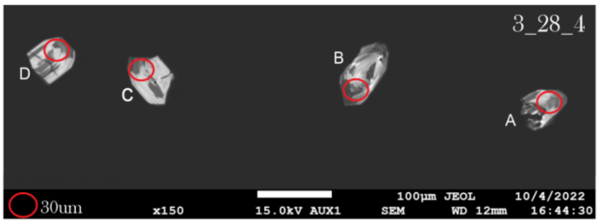

Appendix H: SEM-CL images of zircon grains *(MC-SB, MPF 1)* **(continued)**

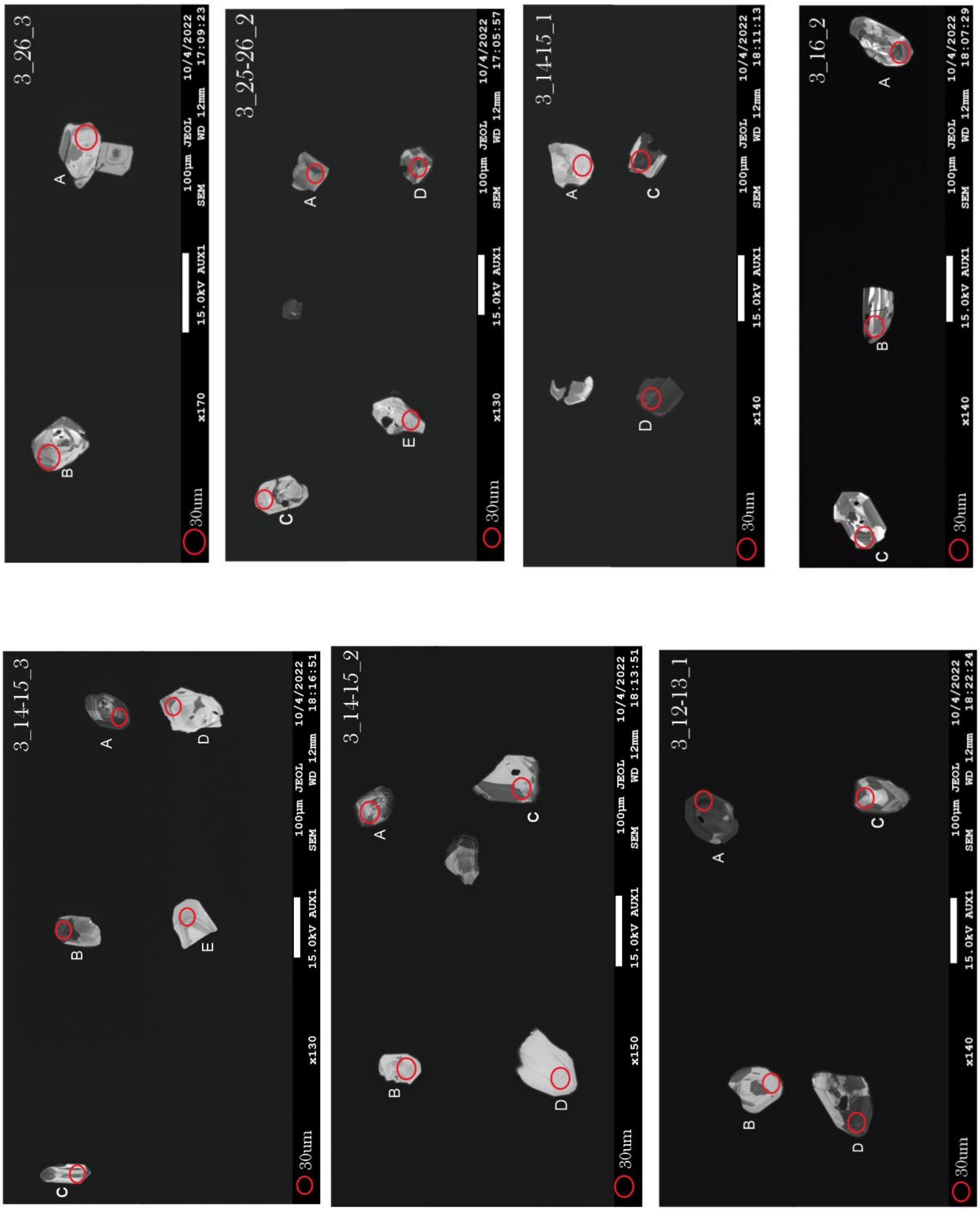

Appendix H: SEM-CL images of zircon grains *(MC-SB, MPF 1)* **(continued)**

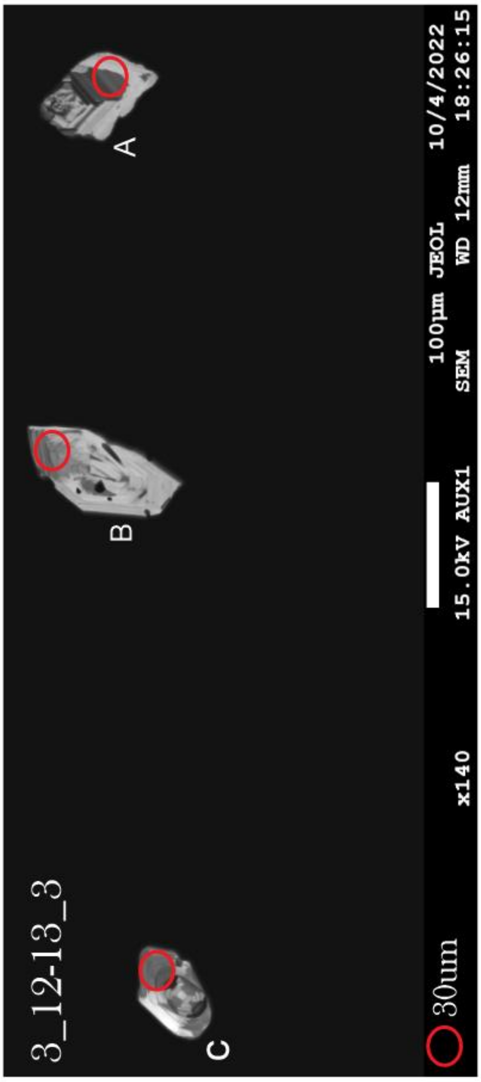

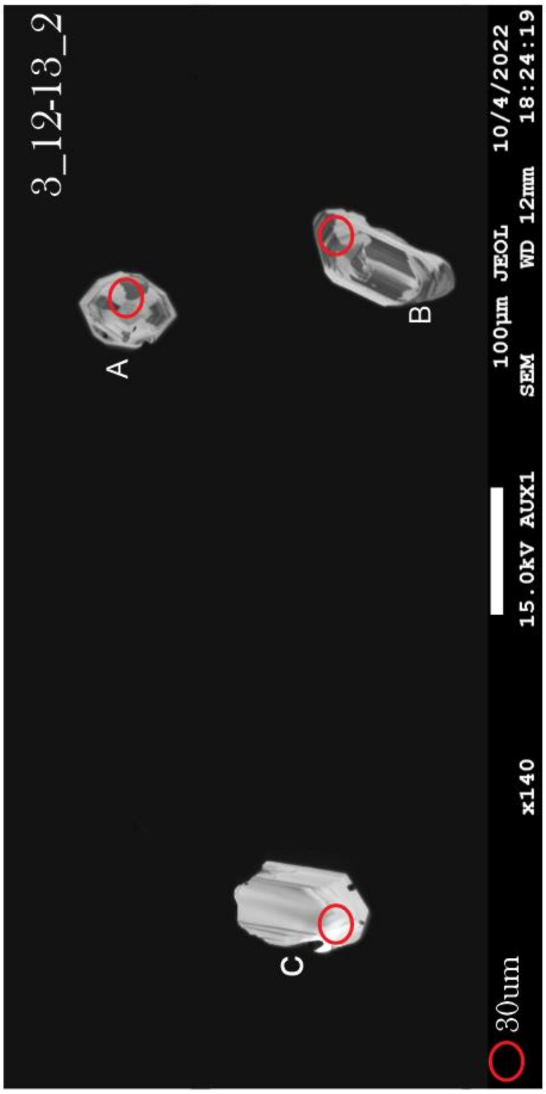

Appendix H: SEM-CL images of zircon grains *(MC-SB, MPF 1)* **(continued)**

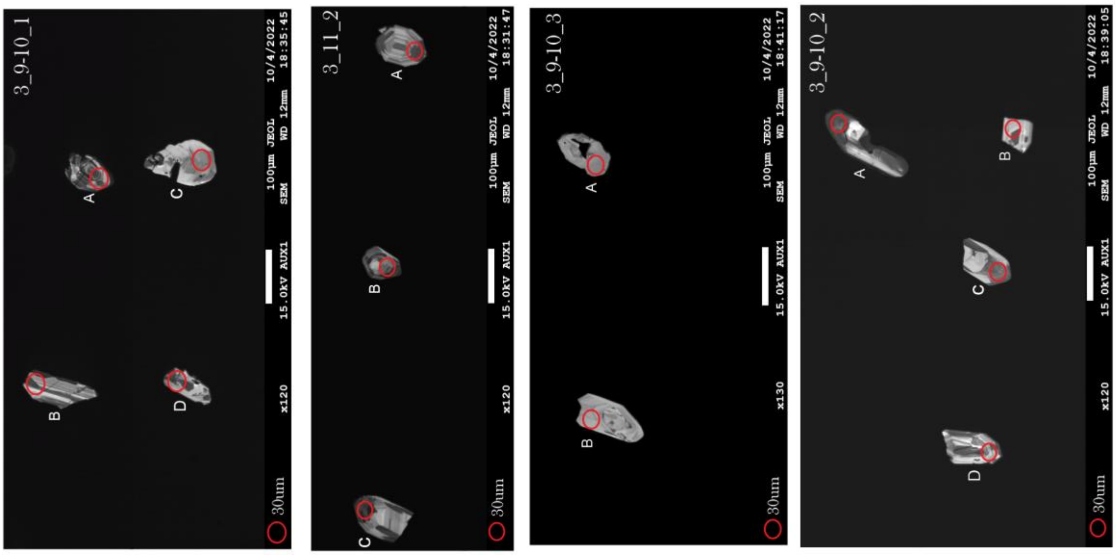
3_9-10_1
3_11_2
3_9-10_3
3_9-10_2

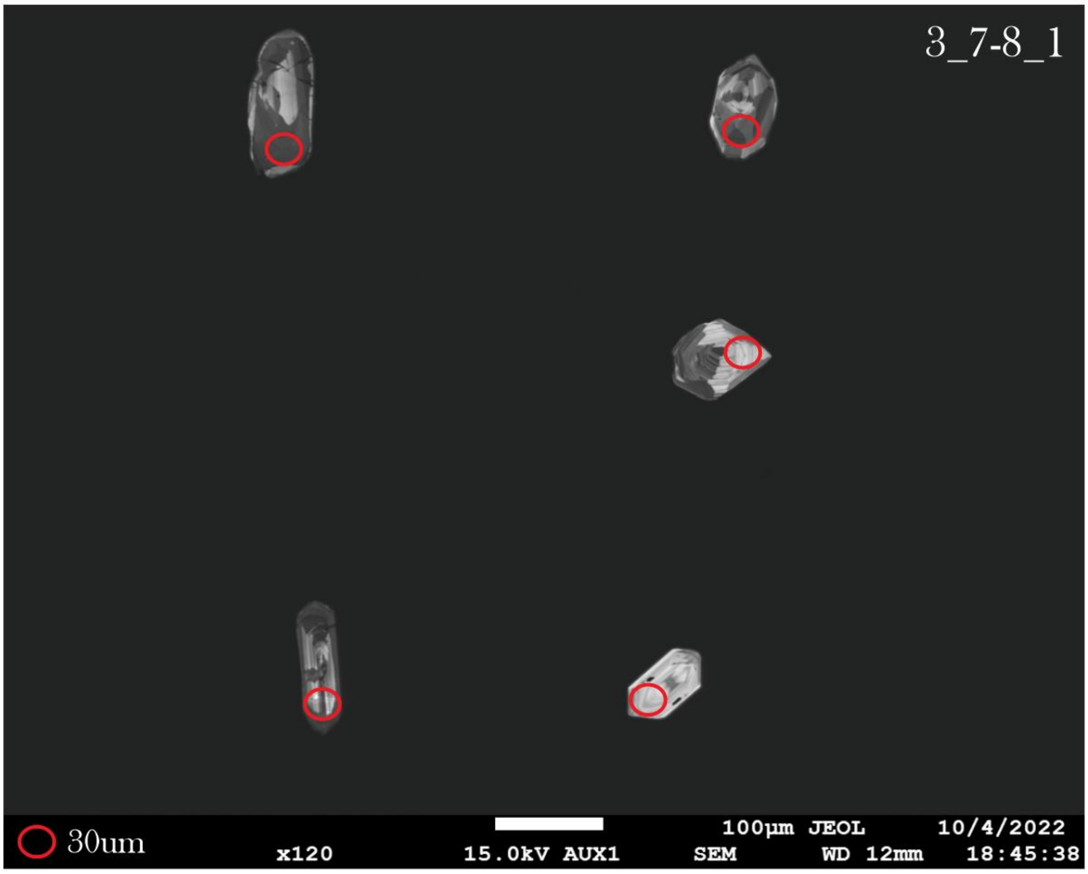
3_7-8_1
30um
x120
15.0kV AUX1
100µm JEOL
SEM
WD 12mm
10/4/2022
18:45:38

Appendix H: SEM-CL images of zircon grains *(HC-SB, MPF 1)* **(continued)**

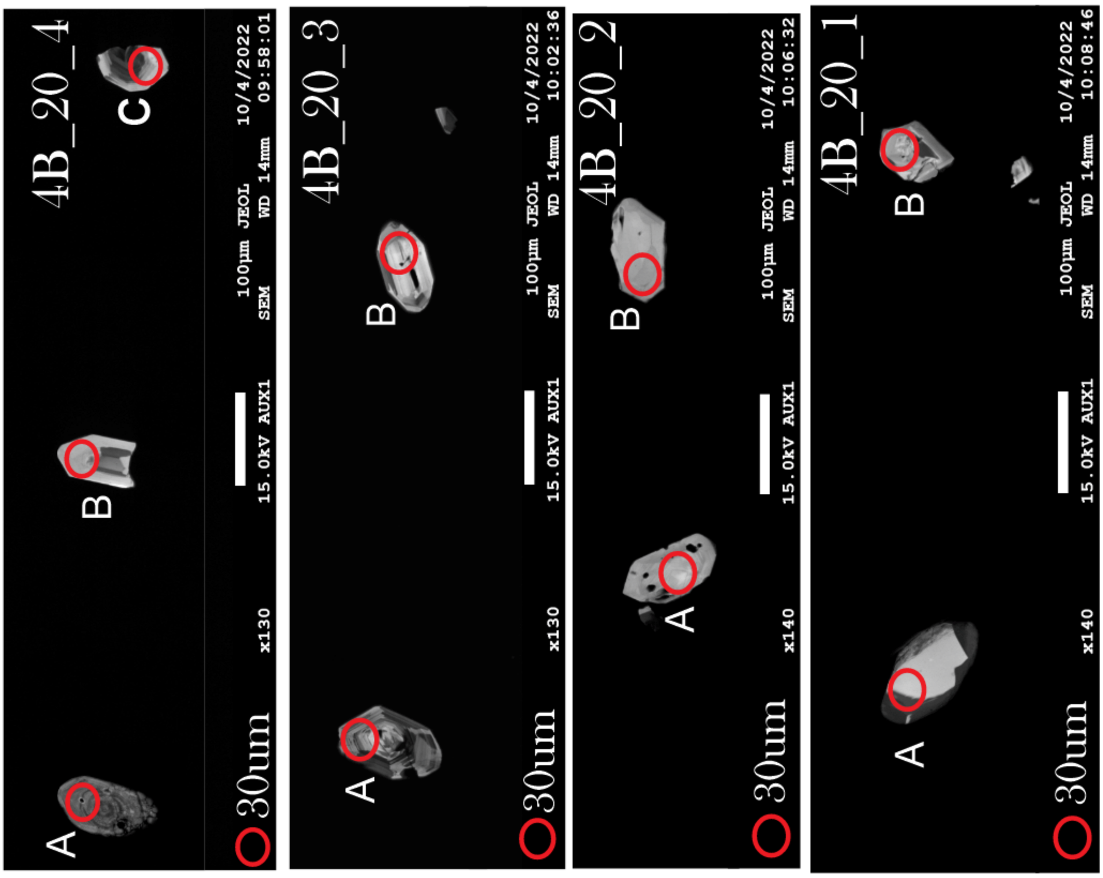

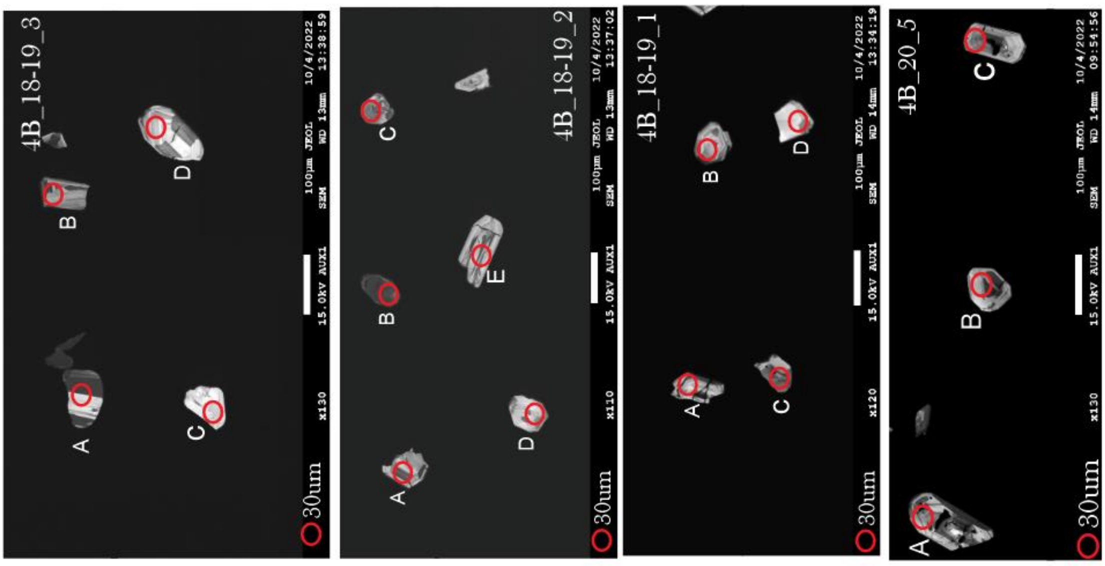

Appendix H: SEM-CL images of zircon grains ***(HC-SB, MPF 1)*** **(continued)**

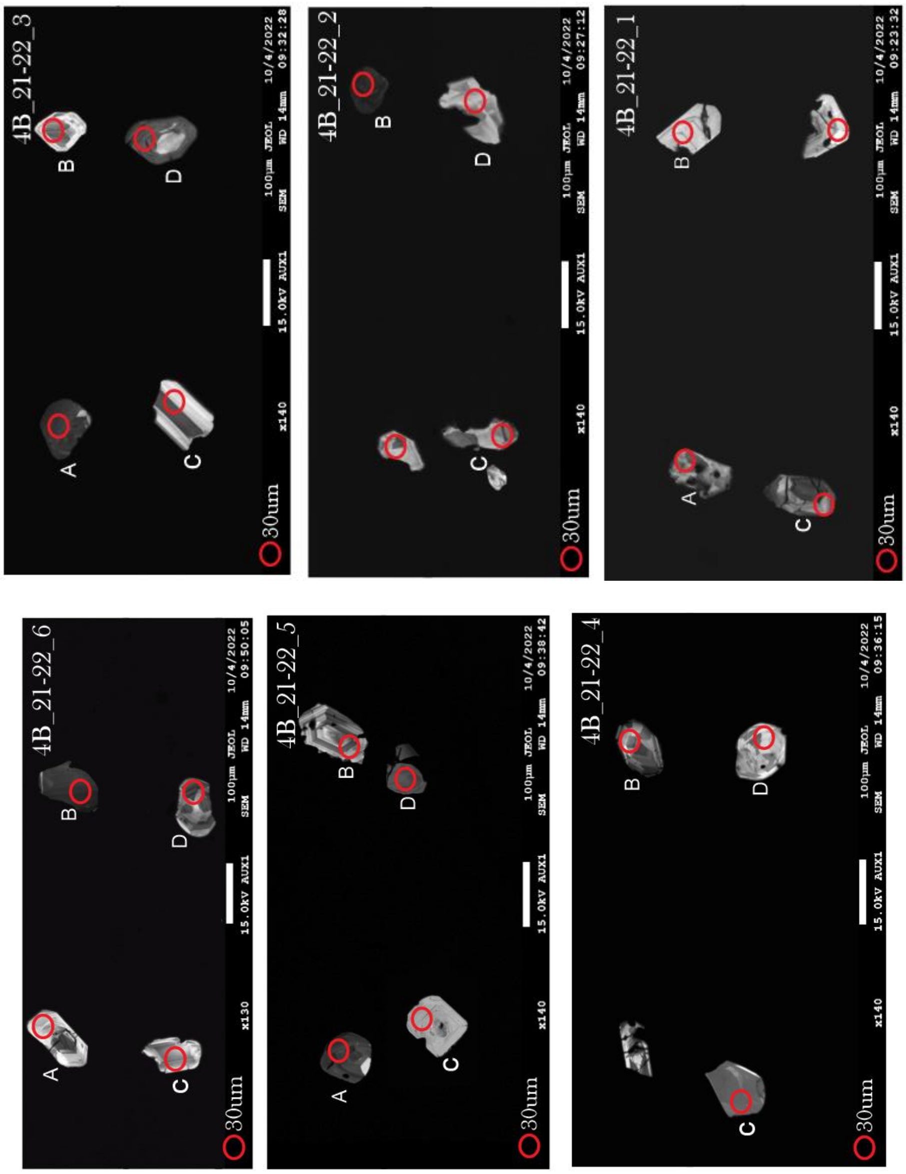

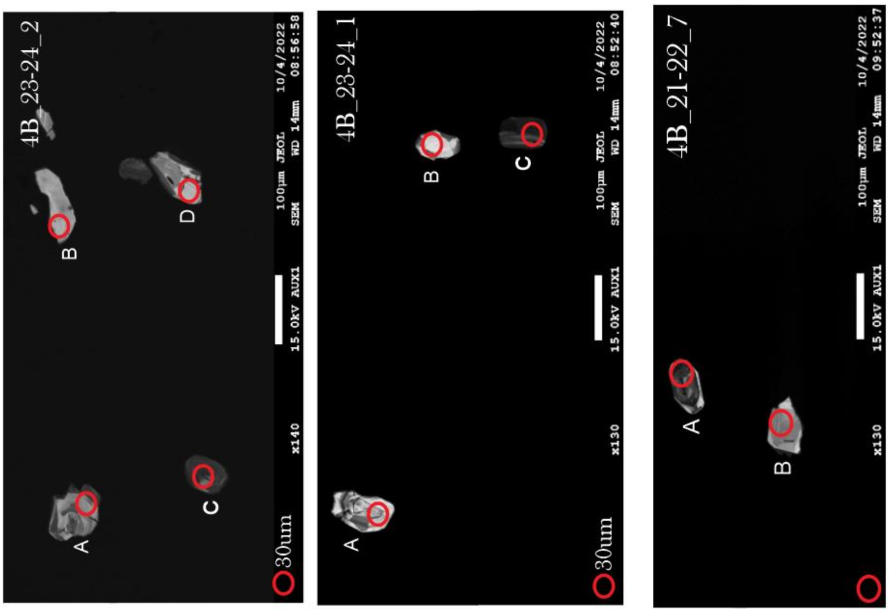

Appendix H: SEM-CL images of zircon grains *(HC-SB, MPF 1)* **(continued)**

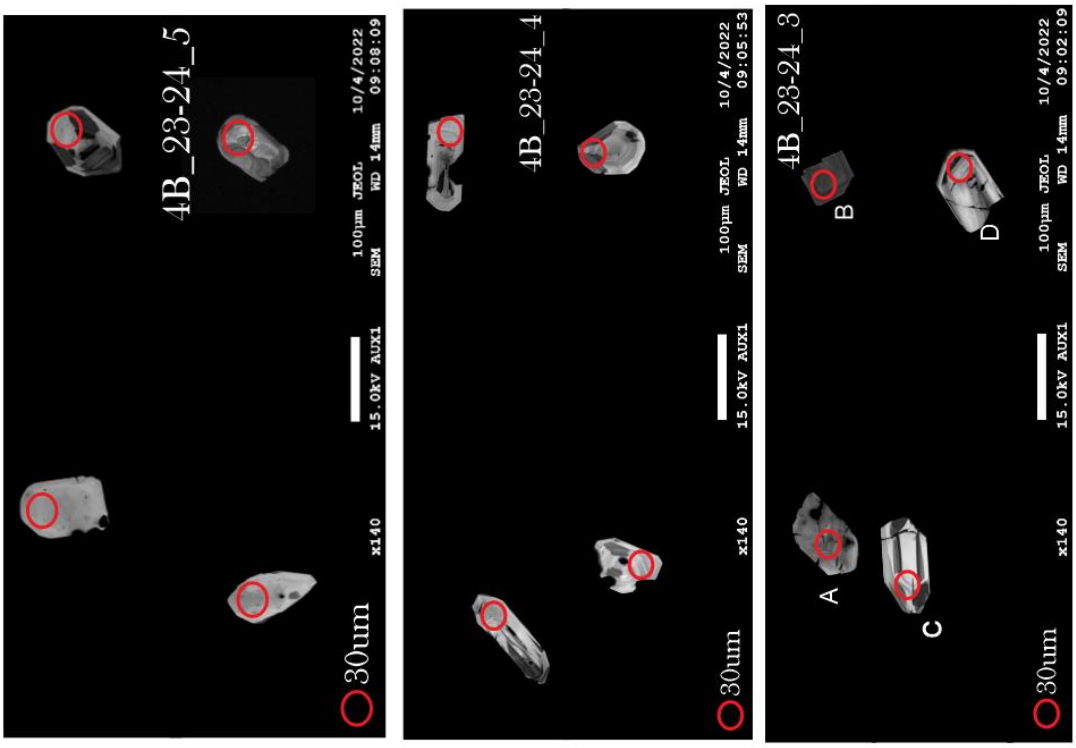

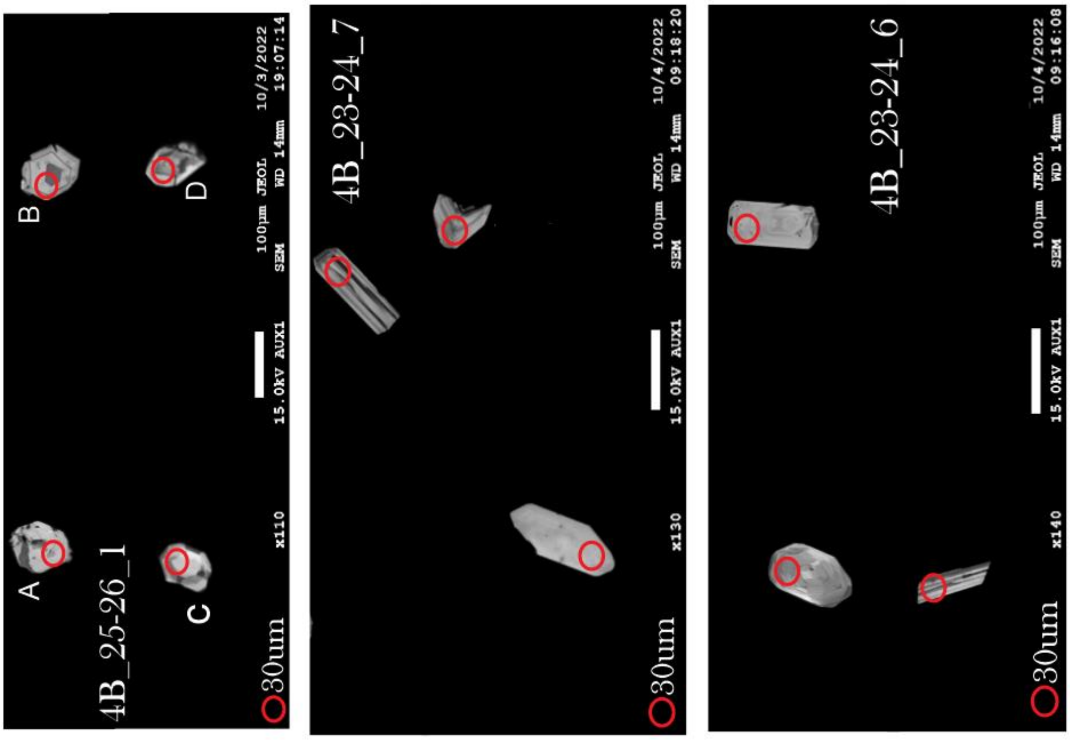

4B_25-26_1
A
B
C
D
30um
x110
15.0kV AUX1
100µm JEOL
SEM WD 14mm
10/3/2022 19:07:14
4B_23-24_7
30um
x130
15.0kV AUX1
100µm JEOL
SEM WD 14mm
10/4/2022 09:18:20
4B_23-24_6
30um
x140
15.0kV AUX1
100µm JEOL
SEM WD 14mm
10/4/2022 09:16:08

Appendix H: SEM-CL images of zircon grains *(HC-SB, MPF 1)* **(continued)**

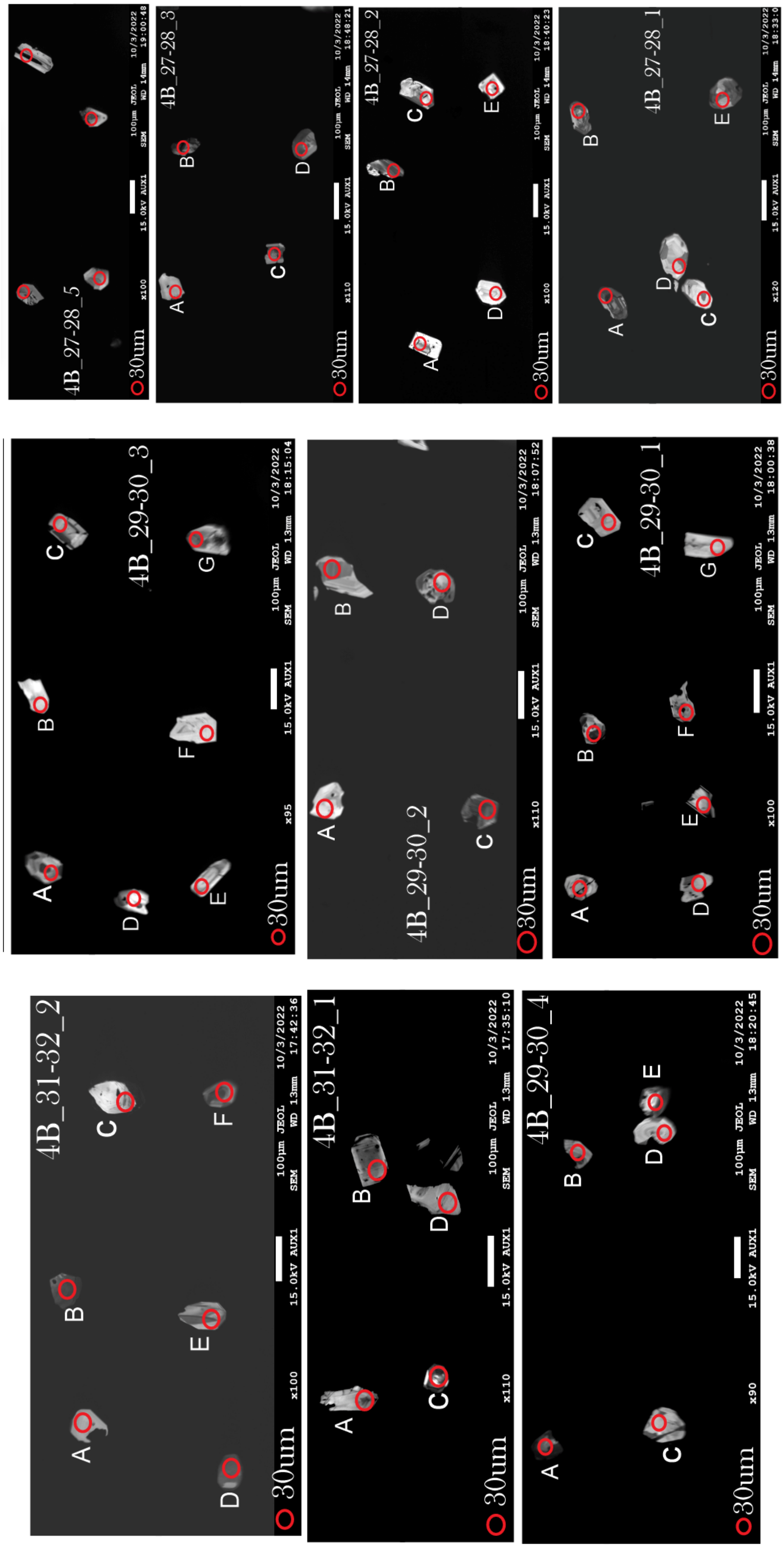

Appendix H: SEM-CL images of zircon grains *(HC-SB, MPF 1)* **(continued)**

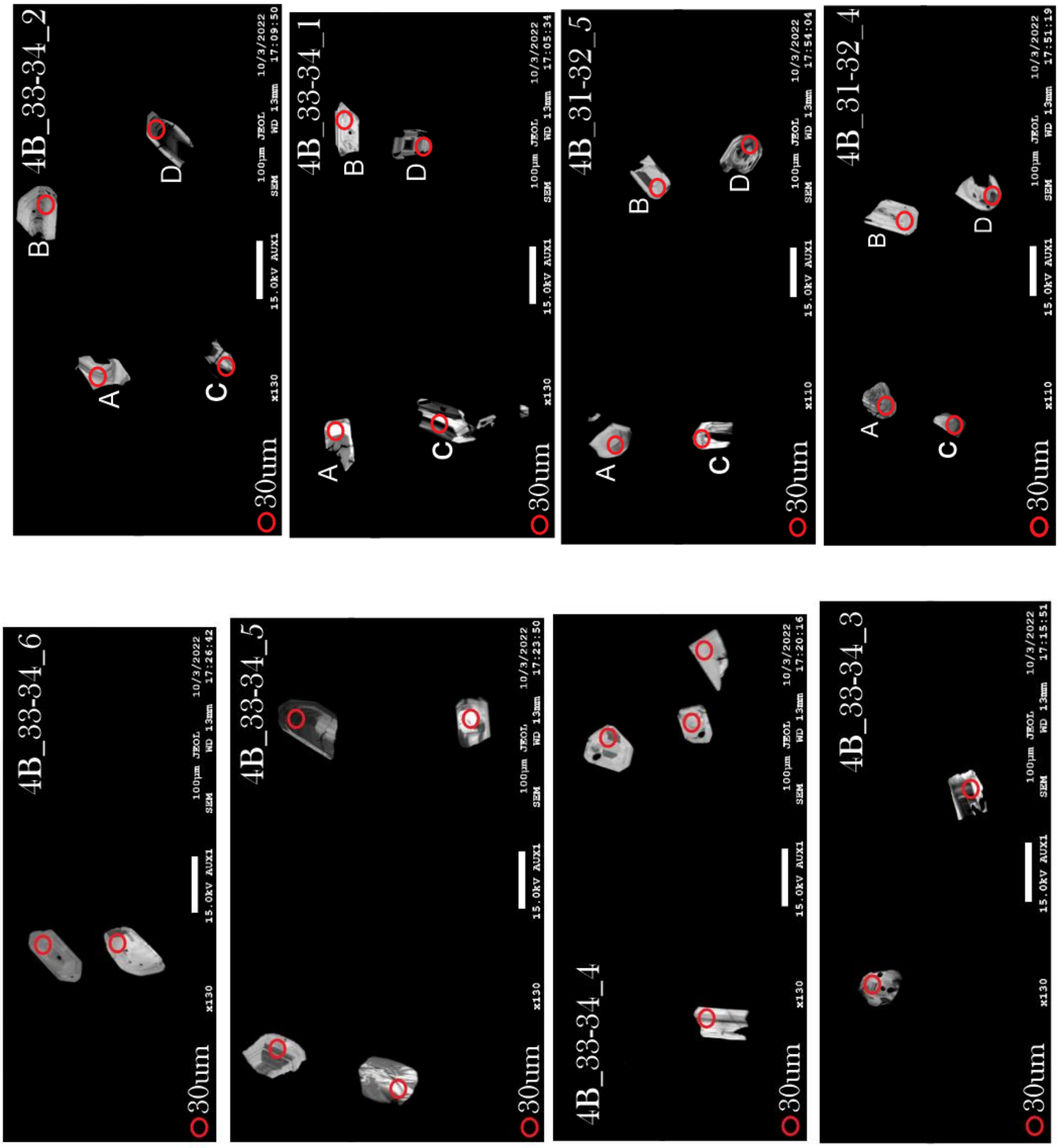

Appendix I: Mapping SEM-CL image zircon address

(HC-ER) Red arrow represents North/ top side.

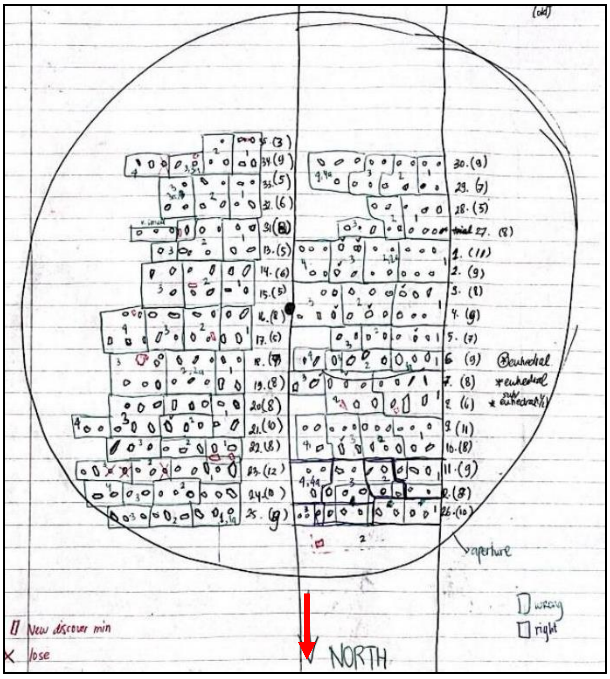

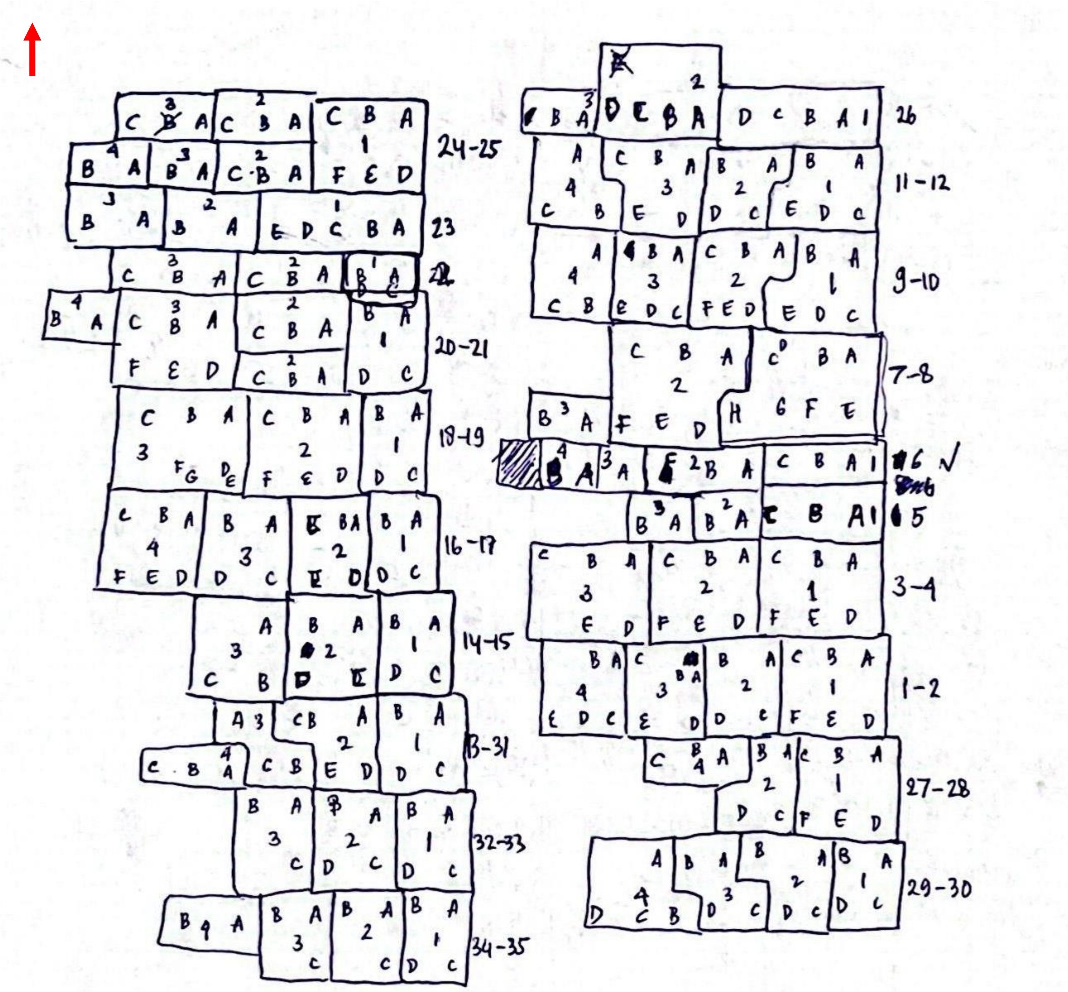

Appendix I: Mapping SEM-CL image zircon address (continued)

(MC-SB) Red arrow represents North/ top side.

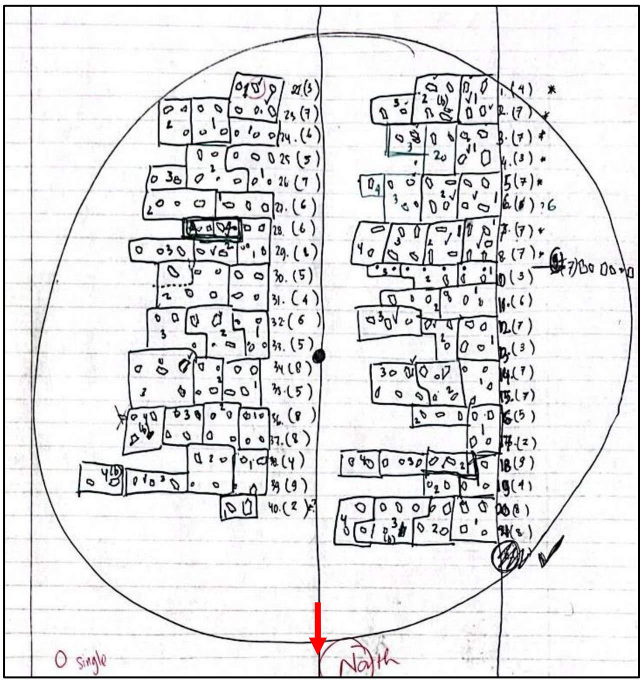

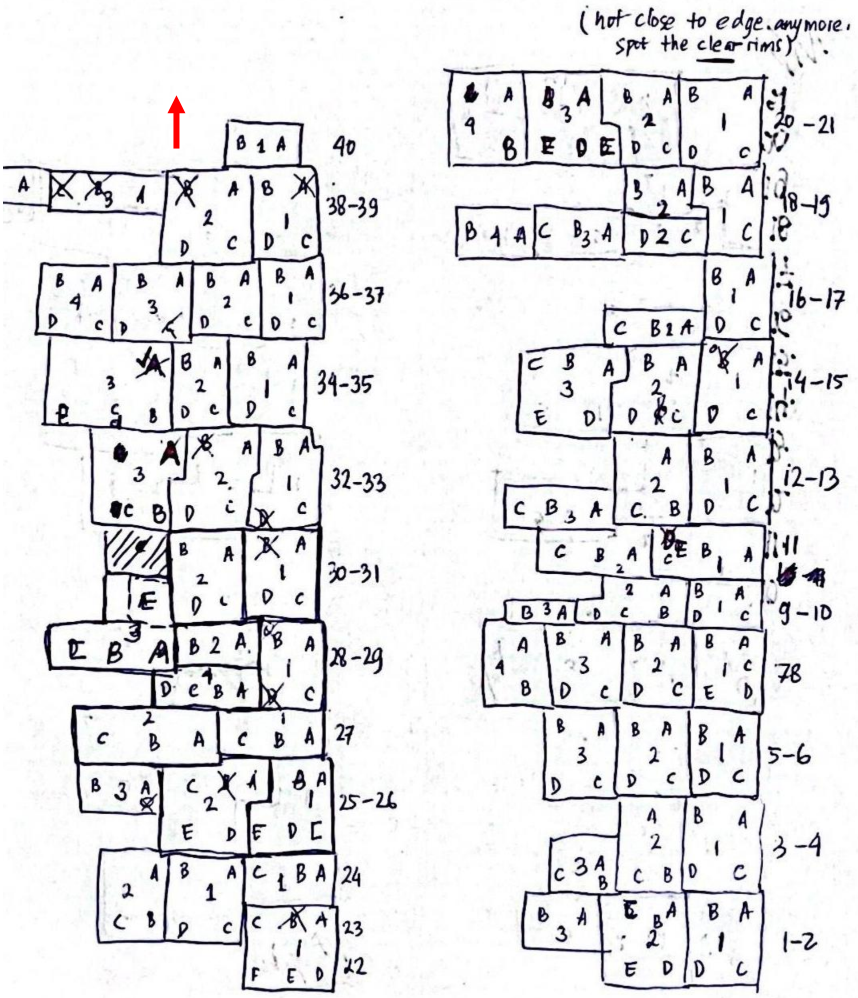

Appendix I: Mapping SEM-CL image zircon address (continued)

(HC-SB) Red arrow represents North/ top side.

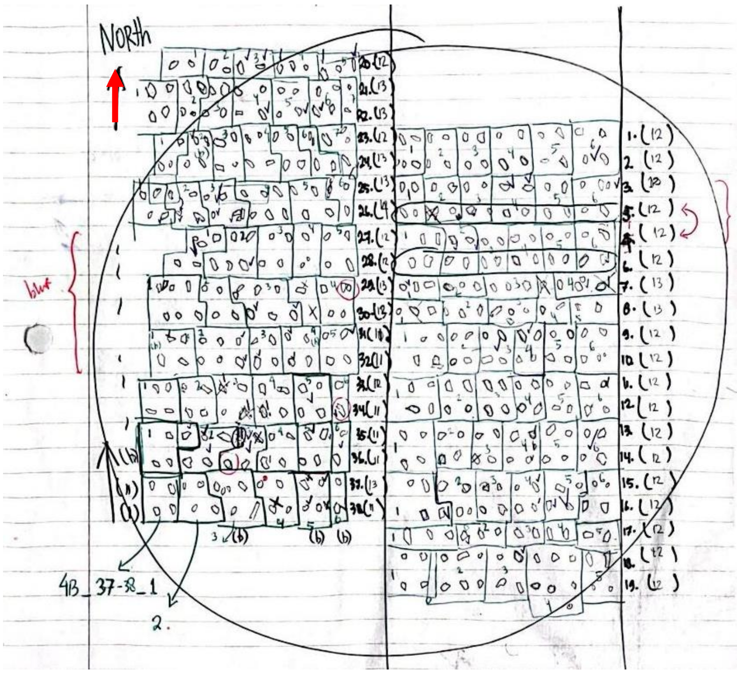

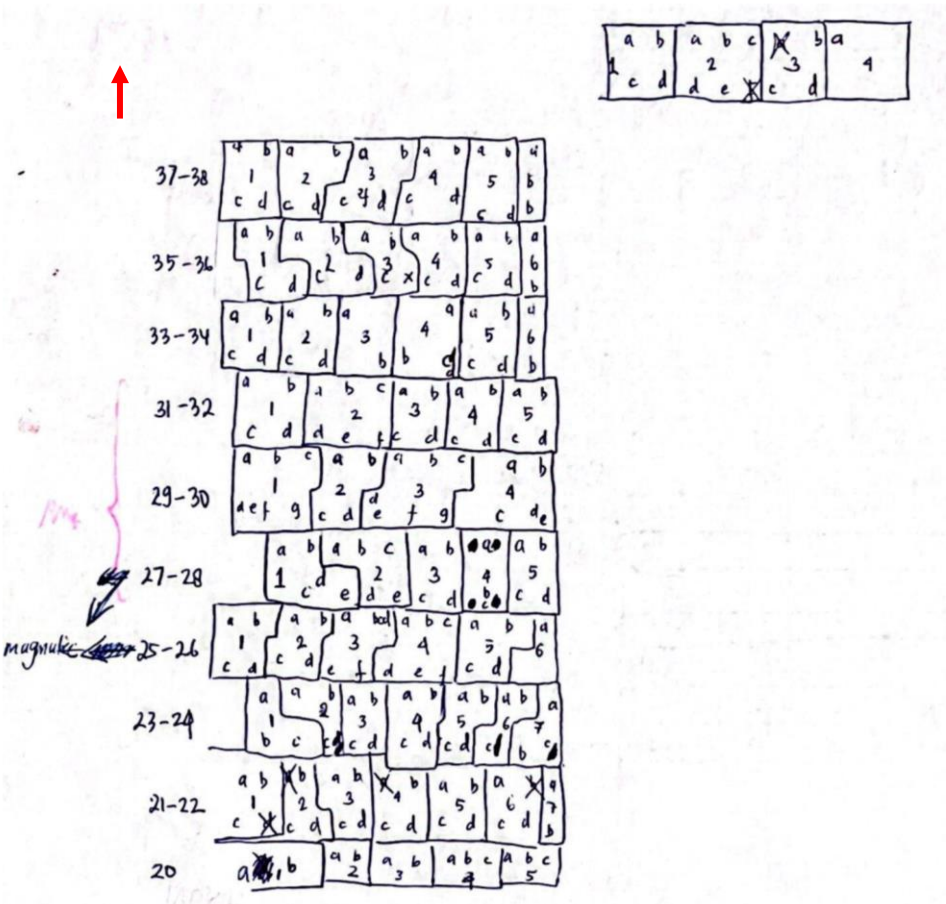

Appendix I: Mapping SEM-CL image zircon address (continued)

(HC-SJ) Red arrow represents North/ top side.

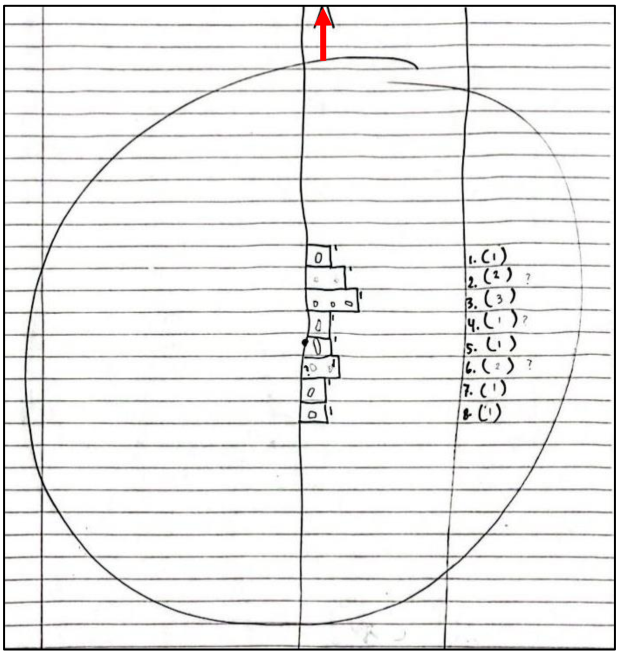

(MC-ER) No zircon found.